



HAL
open science

3D segmentation of pelvic structures in pediatric MRI for surgical planning applications

Alessio Virzì

► **To cite this version:**

Alessio Virzì. 3D segmentation of pelvic structures in pediatric MRI for surgical planning applications. Medical Imaging. Université Paris Saclay (COmUE), 2019. English. NNT: 2019SACLT002 . tel-02107714

HAL Id: tel-02107714

<https://pastel.hal.science/tel-02107714v1>

Submitted on 23 Apr 2019

HAL is a multi-disciplinary open access archive for the deposit and dissemination of scientific research documents, whether they are published or not. The documents may come from teaching and research institutions in France or abroad, or from public or private research centers.

L'archive ouverte pluridisciplinaire **HAL**, est destinée au dépôt et à la diffusion de documents scientifiques de niveau recherche, publiés ou non, émanant des établissements d'enseignement et de recherche français ou étrangers, des laboratoires publics ou privés.

3D segmentation of pelvic structures in pediatric MRI for surgical planning applications

Thèse de doctorat de l'Université Paris-Saclay
préparée à Télécom ParisTech

Ecole doctorale n°580 Sciences et technologies de l'information et de la
communication (STIC)

Spécialité de doctorat : Automatique, Traitement du Signal, Traitement des Images, Robotique

Thèse présentée et soutenue à Paris, le 31/01/2019, par

ALESSIO VIRZÌ

Composition du Jury :

Erwan Kerrien Chercheur, INRIA Nancy-Grand Est & LORIA, Nancy	Rapporteur
Laurence Rouet Chercheur, Philips Research (Medisys), Paris	Rapporteuse
Catherine Adamsbaum Professeur, APHP, CHU Kremlin-Bicêtre, Université Paris Sud, Le Kremlin-Bicêtre	Examinatrice
Thierry Géraud Professeur, EPITA - Research and Development Laboratory (LRDE), Paris	Président
Isabelle Bloch Professeur, Télécom ParisTech (LTCl), Paris	Directrice de thèse
Sabine Sarnacki Professeur, APHP, Hôpital Necker Enfants-Malades, Paris Descartes University, Paris	Co-directrice de thèse

Abstract

Surgical planning relies on the patient’s anatomy, and it is often based on medical images acquired before the surgery. This is in particular the case for pelvic surgery on children, for various indications such as malformations or tumors. In this particular anatomical region, due to its high vascularization and innervation, a good surgical planning is extremely important to avoid potential functional damages to the patient’s organs that could strongly affect their quality of life.

In clinical practice the standard procedure is still to visually analyze, slice by slice, the images of the pelvic region. This task, even if quite easily performed by the expert radiologists, is difficult and tedious for the surgeons due to the complexity and variability of the anatomical structures and hence their images. Moreover, due to specific anatomy depending on the age of the patient, all the difficulties of the surgical planning are emphasized in the case of children, and a clear anatomical understanding is even more important than for the adults. For these reasons it is very important and challenging to provide the surgeons with patient-specific 3D reconstructions, obtained from the segmentation of MRI images.

In this work we propose a set of segmentation tools for pelvic MRI images of pediatric patients. In particular, we focus on three important pelvic structures: the pelvic bones, the pelvic vessels and the urinary bladder.

For pelvic bones, we propose a semi-automatic approach based on template registration and deformable models. The main contribution of the proposed method is the introduction of a set of bones templates for different age ranges, which allows us to take into account the bones variability during growth. For vessels segmentation, we propose a patch-based deep learning approach using transfer learning, thus requiring few training data. The main contribution of this work is the design of a semi-automatic strategy for patches extraction, which allows the user to focus only on the vessels of interest for surgical planning. For bladder segmentation, we propose to use a deformable model approach that is particularly robust to image inhomogeneities and partial volume effects, which are often present in pediatric MRI images.

All the developed segmentation methods are integrated in an open-source plat-

form for medical imaging, delivering powerful tools and user-friendly GUIs to the surgeons. Furthermore, we set up a processing and portability workflow for visualization of the 3D patient specific models, allowing surgeons to generate, visualize and share within the hospital the patient specific 3D models.

Finally, the results obtained with the proposed methods are quantitatively and qualitatively evaluated by pediatric surgeons, which demonstrates their potentials for clinical use in surgical planning procedures.

Publications

This work has led to the following publications (in chronological order):

- **A. Virzi**, C. Muller, J.-B. Marret, E. Mille, L. Berteloot, D. Grévent, N. Boddaert, P. Gori, S. Sarnacki and I. Bloch, *Comprehensive review of 3D segmentation software tools for pediatric MRI usable for pelvic and abdominal surgery planning*, Submitted to Surgical Endoscopy.
- **A. Virzi**, P. Gori, C. Muller, E. Mille, Q. Peyrot, L. Berteloot, N. Boddaert, S. Sarnacki and I. Bloch, *Segmentation of pelvic vessels in pediatric MRI using a deep learning approach*, Journées Francophones de Radiologie Diagnostique et Interventionnelle (JFR), Paris, France, October 2018.
- **A. Virzi**, P. Gori, C. Muller, E. Mille, Q. Peyrot, L. Berteloot, N. Boddaert, S. Sarnacki and I. Bloch, *Segmentation of pelvic vessels in pediatric MRI using a patch-based deep learning approach*. Data Driven Treatment Response Assessment and Preterm, Perinatal, and Paediatric Image Analysis (2018), Springer International Publishing, pp. 97–106
- C. Muller, **A. Virzi**, J.-B. Marret, E. Mille, L. Berteloot, P. Gori, T. Blanc, D. Grevent, F. Barga, N. Boddaert, I. Bloch and S. Sarnacki, *3D patient specific models from MRI segmentation and tractography to enhance surgery planning of pelvic tumors and malformations*, 19th European Congress of Pediatric Surgery, Paris, France, June 2018.
- E. Mille, C. Muller, **A. Virzi**, P. Gori, J.-B. Marret, L. Berteloot, D. Grevent, T. Blanc, N. Boddaert, I. Bloch and S. Sarnacki, *Appraisal of sacral nerve injury by pelvic neurotractography after robotic surgery for a sacral neurofibroma in a 12 years old girl*, 19th European Congress of Pediatric Surgery, Paris, France, June 2018.
- C. Muller, **A. Virzi**, J.-B. Marret, E. Mille, C. Cretolle, P. Gori, L. Berteloot, D. Grevent, T. Blanc, N. Boddaert, I. Bloch and S. Sarnacki, *Analysis of the sacral plexus anatomy using diffusion tensor MRI based neurotractography*,

according to spinal dysraphism, sacral anomaly and type of anorectal malformation, 19th European Congress of Pediatric Surgery, Paris, France, June 2018.

- C. Muller, **A. Virzì**, J.-B. Marret, E. Mille, L. Berteloot, D. Grevent, T. Blanc, N. Garcelon, I. Buffet, E. Hullier-Ammard, P. Gori, N. Boddaert, I. Bloch and S. Sarnacki, *Towards building 3D individual models from MRI segmentation and tractography to enhance surgical planning for pediatric pelvic tumors and malformations*, Surgetica 2017, Strasbourg, France, 2017, pp. 113-115
- **A. Virzì**, J.-B. Marret, C. Muller, L. Berteloot, N. Boddaert, S. Sarnacki and I. Bloch, *A new method based on template registration and deformable models for pelvic bones semi-automatic segmentation in pediatric MRI*, IEEE International Symposium on Biomedical Imaging, Melbourne, Australia, 2017, pp. 323-326.

Contents

1	Context and presentation	1
1.1	Pediatric pelvic surgery	1
1.2	Surgical planning	2
1.2.1	Patient specific 3D models	3
1.2.2	Pediatric MRI	3
1.3	Research problem	4
1.4	Manuscript outline	6
2	Image dataset	7
2.1	Patients population	8
2.2	MRI acquisition	8
2.3	Manual segmentations and evaluation measures	11
3	Literature review: pediatric image segmentation	14
3.1	Introduction	16
3.2	Pelvic bones segmentation	16
3.2.1	Methods using only image information	16
3.2.2	Methods using shape priors	18
3.2.3	Discussion	21
3.3	Vessels segmentation	22
3.3.1	Segmentation methods	22
3.3.2	Discussion	23
3.4	Bladder segmentation	24
3.4.1	Segmentation methods	24
3.4.2	Discussion	25
3.5	What about deep learning?	25
3.6	Discussion	26
4	3D segmentation and visualization platforms analysis	27
4.1	Introduction	29
4.2	Software tools evaluation	29

4.2.1	Software tools selected for evaluation	29
4.2.2	Imaging dataset	32
4.2.3	Evaluation criteria	33
4.3	Results	35
4.4	Discussion	39
4.5	Conclusion	44
5	Pelvic bones segmentation	45
5.1	Introduction	47
5.1.1	Context	47
5.1.2	Outline	47
5.2	Segmentation method: a template-based approach	47
5.2.1	Generation of anatomical templates	48
5.2.2	Pre-segmentation from closest template registration	48
5.2.3	Refined segmentation using deformable models	50
Deformable model	50	
Constraints on the surface evolution	51	
5.3	Results	52
5.3.1	Landmark selection	52
5.3.2	Qualitative evaluation of the segmentation results	53
5.3.3	Quantitative evaluation of the segmentation results	53
5.4	Conclusion and discussion	59
5.4.1	Contributions	59
5.4.2	Perspectives	60
6	Pelvic vessels segmentation	61
6.1	Introduction	63
6.1.1	Context	63
6.1.2	Outline	63
6.2	Segmentation method: a patch-based deep learning approach	63
6.2.1	Patches extraction	64
Vascular tree reconstruction	64	
Pseudo-RGB patches extraction	66	
6.2.2	Deep CNN for patches segmentation	67
6.3	Results	68
6.3.1	Landmark selection	69
6.3.2	Qualitative results	69
6.3.3	Quantitative results	69
6.4	Conclusion and discussion	71
6.4.1	Contributions	71
6.4.2	Perspectives	72

7	Bladder segmentation	75
7.1	Introduction	77
7.1.1	Context	77
7.1.2	Outline	77
7.2	Segmentation method: a deformable model approach	77
7.2.1	Pre-processing	77
7.2.2	Pre-segmentation using level-sets	78
7.2.3	Refined segmentation using parametric deformable models	80
7.3	Results	80
7.3.1	Qualitative results	80
7.3.2	Quantitative results	86
7.4	Conclusion	88
7.4.1	Contributions	88
7.4.2	Limits and perspectives	89
8	3D modeling workflow and clinical applications	90
8.1	Introduction	91
8.2	Graphical user interfaces	91
8.3	3D patient specific modeling workflow	97
8.4	Some clinical applications	99
9	Conclusion and future work	103
9.1	Conclusion	103
9.2	Perspectives	106
A	Pelvic tractography	109
A.1	Introduction	110
A.1.1	Context	110
A.1.2	Diffusion MRI and tractography	110
A.2	Pelvic tractography segmentation	113
A.2.1	Modeling the spatial relations	113
A.2.2	Definition of the main pelvic nerves paths	116
A.3	Preliminary results	118
A.4	Conclusion	120
	Bibliography	122

Acronyms

1D one-dimensional.

2D two-dimensional.

3D three-dimensional.

4D four-dimensional.

ARM anorectal malformations.

ASSD Average Symmetric Surface Distance.

CNN convolutional neural networks.

CT computed tomography.

CTA computed tomography angiography.

DC DICE index.

DWI diffusion weighted images.

FOV field of view.

GUI graphical user interface.

GVF gradient vector flow.

LS level-set.

MIS minimally invasive surgery.

MRA magnetic resonance angiography.

MRI magnetic resonance imaging.

ROI region of interest.

SNR signal-to-noise ratio.

SSM statistical shape models.

TPS thin-plate spline.

Chapter 1

Context and presentation

1.1 Pediatric pelvic surgery

The pelvis is an anatomical region that is highly complex, at the crossroad between digestive, genital and urological tracts and with high vascularization and innervation. Its anatomical analysis is particularly difficult due to the complex 3D shapes of the pelvic structures and to their complex spatial relationships. Moreover, in the pelvis, the involved structures (except the bones) are soft and deformable, leading to a strong anatomical inter-patient variability.

Pelvic anatomy is even more complex for children, where organs vary during growth, both in terms of shapes and of relative spatial position. Moreover, all these difficulties are strongly emphasized in case of rare tumors and malformations [3]. However, in the context of surgical planning, a clear understanding of the patient's pelvic anatomy is essential, considering that any lesion of vascular and/or nervous structure may have a major impact on the quality of life.

Nowadays, in order to reduce as much as possible the surgical trauma while maintaining the security and efficiency of gold standard treatments, minimally invasive surgery (MIS) is widely used for pelvic and abdominal pediatric interventions. In fact, while classical (or "open") surgery requires large skin and muscle incisions to allow for the access to the surgical field, MIS uses rigid, thin and long tubular cameras (3 to 10 mm of diameter) in association with surgical instruments inserted through tubular metallic or plastic ports (3 to 15 mm of diameter) through the skin. Thanks to these small incisions, this surgical technique has several advantages such as reduced post-operative pain, faster post-operative recovery and better aesthetic outcomes for the patient.

One of the latest developments of MIS is robotic surgery (see Figure 1.1). The main advantages of this technique are i) a magnified 3D visualization, which allows the surgeon to keep the depth information while looking at the console screen and

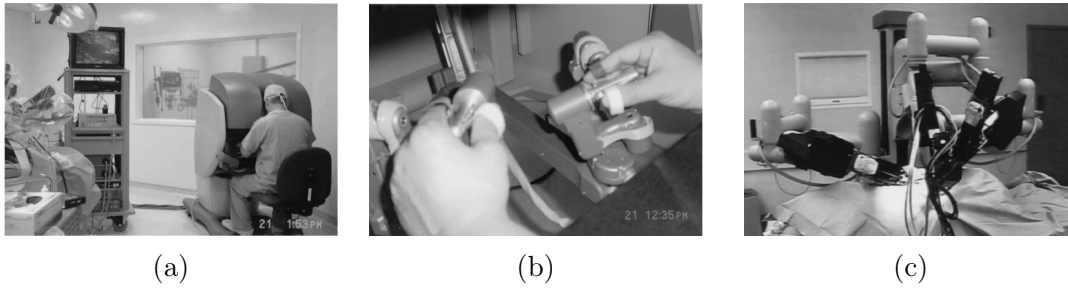


Figure 1.1: Example of MIS using a *da Vinci Surgical System* (Intuitive Surgical, Mountain View, Calif). The surgeon performs the operation looking at a screen (a), manipulating dedicated tools (b) that guide the movement of the robotic arms (c) in contact with the patient. Images drawn from the material in [112].

ii) the presence of 360° articulated instruments, which aims to make robotic surgical experience as “smooth” as the open surgery one. However, this kind of surgery lacks, as classical MIS, of haptic (force) feedback. This produces the loss of the surgeon’s sense of touch, making the robotic interventions clearly more complex than the open ones.

Therefore, due to the extreme complexity of the pelvic anatomy and of the robotic interventions, surgical planning plays a crucial role on ensuring the best possible outcome for the patients.

1.2 Surgical planning

Surgical planning relies on the patient’s anatomy and is based on medical images acquired before the surgery. This is in particular the case for pelvic surgery on children, for various indications such as malformations or tumors. As previously mentioned, in this particular anatomical region, due to its high vascularization and innervation, a good surgical planning is extremely important to avoid potential functional damages to the patient’s organs that could strongly affect their quality of life.

In clinical practice the standard procedure is still to visually analyze, slice by slice, the images of the pelvic region. This task, even if quite easily performed by the expert radiologists, is difficult and tedious for the surgeons due to the complexity and variability of the anatomical structures and hence their images. Moreover, due to specific anatomy depending on the age of the patient, all the difficulties of the surgical planning are emphasized in the case of children, and a clear anatomical understanding is even more important than for the adults. For these reasons it is very important and challenging to provide the surgeons with patient specific three-

dimensional (3D) models, obtained from the processing and analysis of anatomical images.

1.2.1 Patient specific 3D models

3D patient specific modeling has been developed and proved useful in very few specific studies within the general surgical field, to reduce the time required for the surgery giving to the surgeon a major awareness of the patient specific anatomy and of the relationships between the target structures. As demonstrated by the surgeon experience, the more complex the anatomy of the surgical region of interest, the more complete a 3D reconstruction is useful. This gives the surgical staff a powerful planning tool to improve the approach to critical interventions during the pre-operative phase [39, 78, 96]. The advantages of the 3D models in daily practice are especially obvious for surgical planning in oncology, allowing the surgeon to better understand the spatial relationships between the tumor and the surrounding structures. For anorectal malformations (ARM), the 3D models of nerves and muscles may also be useful to better describe the anomalies of the spinal cord and/or muscles frequently associated with such malformations. This should be useful not only to refine the classification of these malformations, but also to evaluate the impact of the different types of surgical approaches and of potential rehabilitation techniques (neuromodulation, physiotherapy). More than just the surgical planning, patients specific 3D models can also be useful during the post operative follow-up (e.g. highlighting complications of the surgery, critical spontaneous evolution, effects of treatments such as chemotherapies or radiotherapies in tumors). Finally, 3D models could also be extremely important to better inform patients and their parents about the pathology and its evolution.

These models can be obtained through processing of medical images. In particular magnetic resonance imaging (MRI), due to its good contrast between the soft tissues and its non-ionizing nature, is the reference imaging modality for the pelvis in pediatric patients [32, 108]. Moreover, with respect to other modalities, MRI also allows obtaining images that represent the water diffusion properties of the tissues. These images, called diffusion weighted images (DWI), are particularly interesting since they allow obtaining 3D representations of the nerve fibers. For a detailed description of the MRI principles, please refer to [49].

1.2.2 Pediatric MRI

MRI acquisitions in pediatrics raises several problems compared to the adults, which have direct impact on the image quality.

During the acquisition, in order to obtain good quality images, the patient has to stay as motionless as possible. This requirement, even if easily accomplished

with adult patients, is more difficult to fulfill with the non-cooperative child. In fact, due to the narrow tube of the MRI machine and to the strong noise that the machine produces during the acquisition, the child tends to move, compromising the whole exam. In order to avoid multiple MRI acquisitions, a mild sedation of the children could be performed (see Chapter 2). However, children's motion can not be totally avoided, which can produce images corrupted by *motion artifacts*, as shown in Figure 1.2.

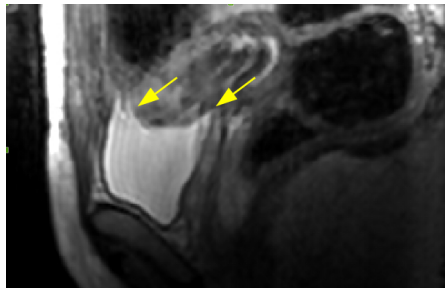


Figure 1.2: Example of motion artifact on a sagittal slice of a T2-w MRI, which produces blurred and repeated structures borders (yellow arrows).

Another strong difference between the adult and the pediatric MR images is given by the different sizes of the target structures. This produces higher *partial volume effects* for children than for adults (using the same MRI acquisition parameters), as shown in Figure 1.3. The partial volume effects are due to the contribution of multiple tissues to the image intensity inside a single voxel. In particular, the bigger the size of the voxel, in relation to the dimensional scale of the structures of interest, the bigger will be the blur close to the structures boundaries. This effect could be partially solved by using higher resolution images for children than for adults. However, due to harder acquisition time constraints in pediatrics than for adults, this is not usually done in clinical practice.

1.3 Research problem

Patients specific 3D modeling is an extremely powerful tool for a better understanding of the patient's anatomy, hence improving the surgical planning procedure, especially for the pelvis in pediatric patients. These 3D models can be obtained by processing the patient's MRI, which is the reference image modality for the pelvis. The reference procedure to obtain the 3D models is manual segmentation. However, this procedure is extremely tedious and time consuming, which clearly limits the routine use of 3D models in clinical practice. For this reason, automated or semi-automated segmentation tools are essential in order to obtain

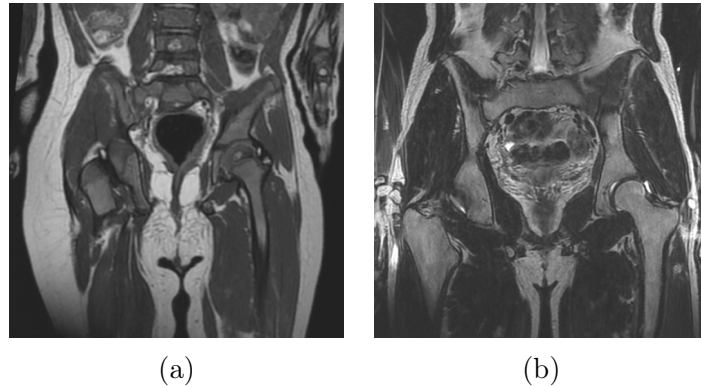


Figure 1.3: Coronal T2-w MRI slices of (a) an adult patient and (b) a pediatric patient, corresponding to the same anatomical pelvic region. The pediatric image has stronger blur on structures boundaries than the adult image.

faster segmentation results. However, in the literature, there is a strong lack of segmentation methods for pelvic structures applicable to pediatric populations. This is mostly due to the strong complexity of the involved structures and to the image acquisition constraints in pediatrics.

For this reason, in order to bridge the gap between adults and children treatments, there is a strong need for novel segmentation tools for pediatric pelvic MRI. Moreover, the developed methods should be user friendly, robust and should respect the time constraints of the daily clinical practice. In this work we will focus on three pelvic structures: i) the pelvic bones, which constitutes a core structure of the pelvis and that serve as spatial reference for surgical planning, ii) the vessels, whose preservation is essential in order to avoid potential functional damages to the patient’s organ, and iii) the bladder, which has a central position in the pelvic region. For each structure of interest, the proposed approach strongly relies on prior knowledge on anatomy, including its variability.



Figure 1.4: Aim of this work: obtaining patient specific 3D models from MRI images.

1.4 Manuscript outline

This manuscript is structured around the design of a set of segmentation tools, specific for pelvic structures in pediatric MRI, integrated in a complete framework for surgical planning.

In Chapter 2, we describe the image dataset (patients population and imaging sequences) used in this work.

In Chapter 3, we review the state of the art on pelvic segmentation, with a particular focus on the complexity of pediatrics.

In Chapter 4, we analyze and evaluate a set of 3D segmentation and visualization platforms, which can be used for pelvic MRI images. This review is a major contribution of this work, and it is, to the best of our knowledge, the first study that takes also into account the segmentation performances on the software tools evaluation.

In Chapter 5, we present a new method for pelvic bones segmentation, which is the first study for their segmentation in pediatric MRI. The proposed method is based on template registration and deformable models, and takes into account the bones variability during growth.

In Chapter 6, we present a novel approach for the segmentation of the pelvic vessels in pediatric MRI. The proposed method consists on a semi-automatic extraction of a set of axial patches containing the vascular structures of interest, followed by an automatic segmentation procedure based on CNN and transfer learning.

In Chapter 7, we present a method for bladder segmentation based on a modified version of the Chan-Vese level set model, aiming to obtain a robust presegmentation, and on a parametric deformable model for segmentation refinement.

In Chapter 8, we present the developed GUIs, the novel workflow for surgical planning based on the developed tools, and some interesting clinical applications of patient specific 3D modeling.

In Chapter 9 we present our conclusions and an overview of potential future works. Lastly, in Appendix A we present our preliminary work on the 3D modeling of the pelvic nervous system, based on tractography.

Chapter 2

Image dataset

Abstract

In this chapter we present the image dataset used in this study, describing the patients population and the MRI acquisition protocol. Finally, we describe the dataset of the manually annotated images and we present the evaluation measures that will be used to validate the proposed segmentation methods.

Contents

2.1	Patients population	8
2.2	MRI acquisition	8
2.3	Manual segmentations and evaluation measures	11

2.1 Patients population

From December 2015 onward, each pediatric patient hosted in *Necker Enfants Malades Hospital* for a pelvic tumor or malformation was considered eligible for a perspective clinical study called “*Anatomie computationnelle dans la chirurgie des tumeurs et malformations de l’enfant*” (Computational anatomy for surgery of tumors and malformations in pediatric patients).

The exclusion criteria for the study were:

- patient being younger than 3 months or older than 18 years;
- contra-indication to MRI exam (e.g. intraocular metallic foreign body, pacemakers, mechanic cardiac valve, vascular clips for brain aneurysm);
- participation to a clinical trial demanding dosing of a new molecule in the 30 days before the MRI exam;
- MRI exam requiring general anesthesia.

All the socio-demographic, clinical and para-clinical data were collected in an interactive anonymous database hosted at the Imagine Institute. All patients or patient’s parents gave their informed consent according to ethical board committee requirements (N°IMIS2015-04).

From December 2015 until October 2018, 88 patients were included in the study:

- 38 patients affected by pelvic tumor;
- 47 patients affected by pelvic malformation;
- 3 control patients.

More details on the patients population are provided in Table 2.1.

2.2 MRI acquisition

The images acquisitions were performed with a 3T MRI scanner (GE Healthcare[®]) hosted in the radiology service of the Necker-Enfants Malades hospital (Pr. Nathalie Boddaert, Dr. Laureline Berteloot). In order to optimize the images signal-to-noise ratio (SNR), a cardiac coil (32 channels) was used for the patients younger than 10 years old. An abdominal coil (16 channels) was used for the other patients, which necessitated to increase the image field of view (FOV) in order to cover the whole pelvic region.

Pathology	Type	Number	Age (median [min, max])
Tumor	Ovarian lesion	11	103.4 [3.0 - 195.8]
	Sacrococcygeal teratoma	5	
	Rhabdomyosarcoma	4	
	Cystic lymphangioma	3	
	Abdominal or pelvic neurofibroma	3	
	Other	2	
	Nephroblastoma	2	
	Ganglioneuroblastoma	1	
	Ganglioneuroma	1	
	Vascular malformation	1	
	Sub-diaphragmatic pulmonary sequestration	1	
	Total	38	
Malformation	Other	13	48.3 [3.0 - 175.4]
	ARM with perianal fistula	9	
	ARM with recto-bulbar fistula	4	
	ARM with vestibular fistula	4	
	Cloacal malformation	3	
	Rectal atresia	2	
	ARM with recto-prostatic fistula	2	
	ARM with recto-vesical fistula	2	
	ARM without fistula	4	
	Rectal duplication	1	
	Bladder exstrophy	1	
	ARM with recto-vaginal fistula	1	
	Urogenital sinus malformation	1	
	Total	47	

Table 2.1: Patients population and corresponding pathologies. Patients' ages are expressed in months.

A respiratory trigger, made possible by measuring the breathing frequency with a dedicated belt, was sometimes used, in order to reduce the breathing movement artifacts. However, this procedure increases the acquisition time, especially in case of high breathing frequencies. For this reason, no respiratory trigger was normally

used for the youngest patients.

A glucagon injection, based on an already established acquisition protocol, was performed in order to reduce the digestive peristalsis. The MRI exam is then followed by an oral sugar administration to the patient. As already mentioned, general anesthesia was never performed. However, a mild sedation with Phenobarbital (5mg/kg dose) was sometimes required. Asthma, pathological amygdale and adenoids hypertrophy constitutes contra-indication to this sedation procedure. The total duration of the exam is 30-45 minutes.

MRI sequences

The full MRI acquisition is composed by: i) a set of MRI sequences needed for the clinical analysis of the patients (a well-established acquisition protocol of the radiology department of the Necker Hospital), and ii) two research sequences, added in the context of the 3D patient modeling. In particular, the two research sequences are:

- *CoroT2cube*: the volumic images resulting from this sequence were chosen as anatomical reference for the developed segmentation methods. This sequence was chosen due to its overall good intensity contrast for the anatomical structures of interest (i.e. bones, bladder, vessels, rectum). Moreover, the spatial resolution being quasi-isotropic, this image is particularly well suited for 3D segmentation methods. Some acquisition examples are shown in Figure 2.1.
- *DWI*: the images resulting from this sequence, containing the tissues diffusion information in several spatial directions, are essential in order to obtain nerve fibers reconstruction through tractography algorithms [55]. More details on DWI, tractography and on how nerves reconstructions were included into the patient 3D models are given in Appendix A.

The acquisition parameters of these two sequences were progressively optimized since December 2015, in order to obtain a good compromise between the image quality and the acquisition time. For this reason, the images of the patient dataset have different acquisition parameters, which produces, for example, images different spatial resolutions. Some details on the most up-to-date sequences parameters are given in Table 2.2.

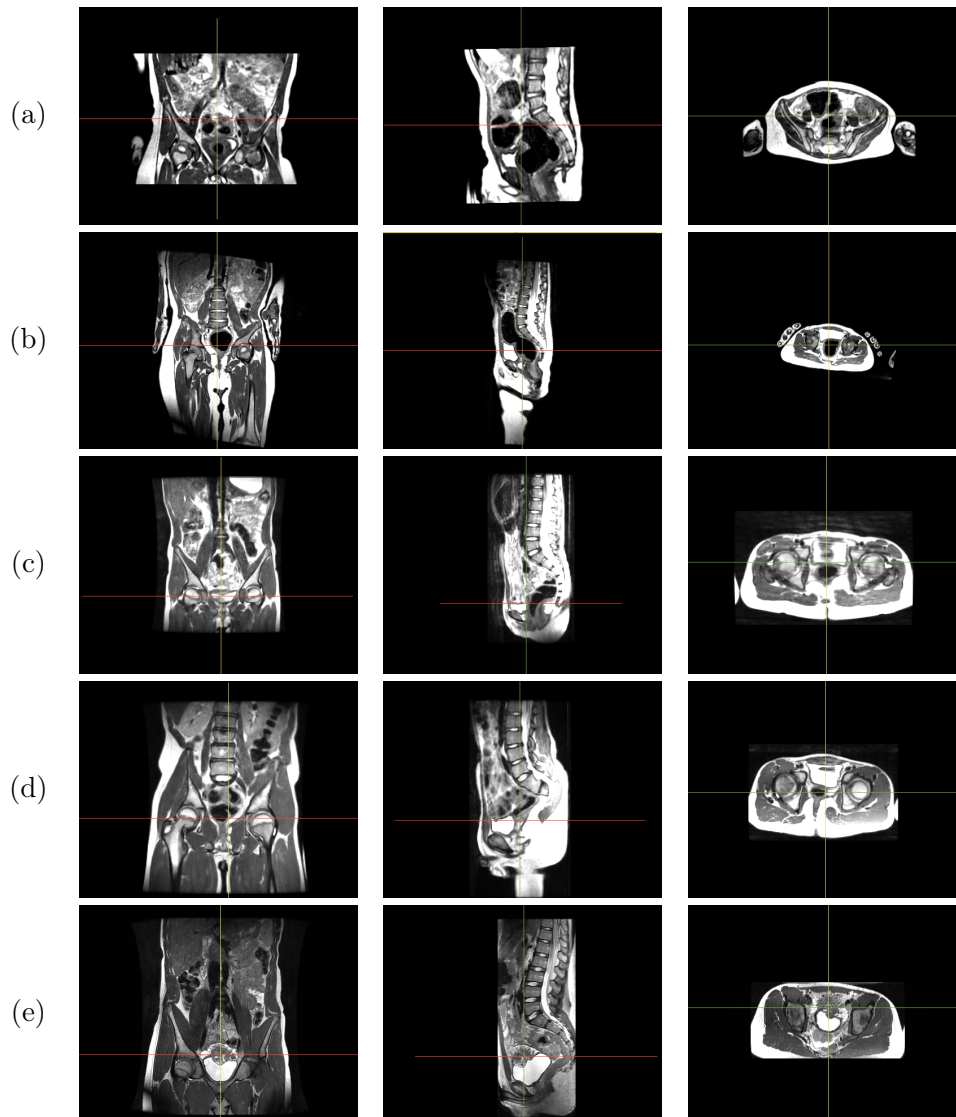


Figure 2.1: Examples of *CoroT2cube* MRI images of patients of (a) 1 year old, (b) 2 years old, (c) 5 years old, (d) 8 years old and (e) 12 years old. Coronal, sagittal and axial slices are depicted from left to right. Red, yellow and green lines represent the slices interseactions.

2.3 Manual segmentations and evaluation measures

In order to validate the performances of the proposed segmentation methods (see Chapters 5, 6 and 7), manual reference segmentations of the T2-w images need

Sequence	Acq. Plan	TR [ms]	TE [ms]	FA [°]	N	b	Voxel Size [mm3]	Acq. time [min]
CoroT2cube	coronal	2000	68.36	90	-	-	1x1x1	5-10
DWI	axial	5893	57.4	90	25	600	1.25x1.25x3.5	5-10

Table 2.2: MRI sequences used in this work and most up-to-date acquisition parameters. TR, FA and TE stand for repetition time, flip angle and time echo, respectively. N and b stand for the number of diffusion directions and the diffusion b-value, respectively.

to be performed. However, this procedure is very time consuming (see Chapter 4). Moreover, in order to evaluate the inter-user variability for each annotated structure, each image was manually segmented by two different users. For these reasons, a subset of the whole patients’ population was manually segmented. In particular, manual segmentations of the bones and the bladder were performed on 25 patients (12 tumors, 13 malformations) and manual segmentations of the pelvis vessels were performed for 35 patients (22 tumors, 13 malformations). More details on the two manually annotated subsets are given in Table 2.3.

Subset	N_tot	N_tum	N_malf	Average voxel size [mm3]	Average Image Size [voxels]
Bones/Bladder	25	12	13	0.94x0.94x0.71	348x348x198
Vessels	35	22	13	0.92x0.92x0.73	346x346x197

Table 2.3: Description of the two T2-w MRI subsets used for the validation of the proposed methods.

In order to quantitatively compare the reference manual segmentations with the results obtained with the proposed methods, we use the DICE index (DC) [31] and the Average Symmetric Surface Distance (ASSD) [52], defined as:

$$DC(A, B) = \frac{2|A \cap B|}{|A| + |B|},$$

$$ASSD(A, B) = \frac{1}{|S(A)| + |S(B)|} \left(\sum_{s_A \in S(A)} \min_{s_B \in S(B)} \|s_A - s_B\|_2 + \sum_{s_B \in S(B)} \min_{s_A \in S(A)} \|s_A - s_B\|_2 \right),$$

where $S(A)$ and $S(B)$ are the sets of surface voxels of A and B , s_A and s_B are points on $S(A)$ and $S(B)$ respectively, $|\cdot|$ denotes the cardinality and $\|\cdot\|_2$ the Euclidean distance.

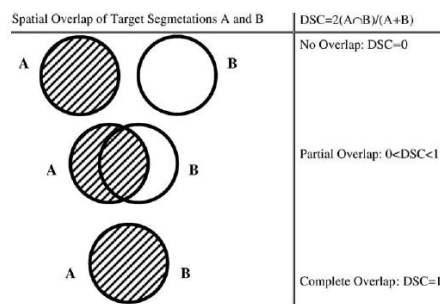


Figure 2.2: Dice score between two sample masks A and B [142].

Chapter 3

Literature review: pediatric image segmentation

Abstract

This chapter reviews the main existing segmentation methods, focusing on the anatomical structures of interest of this work: the pelvic bones, the vessels and the bladder. Due to the lack of studies directly applied to pediatric images, we also discuss methods applied to adults and we analyze the reasons that make them difficult to be applied to the pediatric population.

Contents

3.1	Introduction	16
3.2	Pelvic bones segmentation	16
3.2.1	Methods using only image information	16
3.2.2	Methods using shape priors	18
3.2.3	Discussion	21
3.3	Vessels segmentation	22
3.3.1	Segmentation methods	22
3.3.2	Discussion	23
3.4	Bladder segmentation	24
3.4.1	Segmentation methods	24
3.4.2	Discussion	25
3.5	What about deep learning?	25

3.6 Discussion 26

3.1 Introduction

Image segmentation is one of the most widely explored topics by the medical image processing community. However, there is a huge gap in terms of research effort between the adult and the pediatric field. Almost all the studies on pediatrics are focused on specific anatomical structures, such as the brain in MRI [30, 58, 132] (which is the most studied structure), the heart in ultrasound images [4, 86, 87] and the kidneys in computed tomography (CT) [13] and ultrasound images [17, 82]. Other isolated studies on pediatric image segmentation are, for example, dedicated to adipose tissue segmentation in MRI [41, 64].

As described in Chapter 1, the main structures of interest for pelvic surgical planning are the pelvic bones, the vessels, the bladder and the rectum. To the best of our knowledge, the only studies that address the problem of segmentation of one of these structures, in pediatrics, are focused on the bone structures on CT images [6, 7].

Considering the strong lack of studies on pelvic structure in pediatric images, we will now investigate the methods that were successfully applied to adults (and the few that were applied to pediatrics). Moreover, we will analyze the reasons that make them difficult to be used for our pediatric application.

3.2 Pelvic bones segmentation

The most widely used imaging modality for the analysis of the bone structures is CT. This is mostly due to the high density of the bones compared to the other tissues, which produces images with high contrasted and hyperintense bones structures (see Figure 3.1). For this reason, many successful CT bones segmentation methods were developed, especially for adult patients. However, some studies also addressed the problem of bones segmentation in MRI images of adults patients.

Both for CT and MRI, it is possible to group the existing methods into two macro categories: i) the methods that do not require shape priors on the bones structure and ii) the ones that require shape priors in term of anatomical atlases or statistical shape models (SSM). These methods are discussed in the following sections.

3.2.1 Methods using only image information

Gray-levels thresholding is surely one of the most easy ways to segment an image, when the structures to be segmented can be clearly identified and distinguished from the others based on their intensity values. This condition, which cannot be assumed for bones in MRI, can be somehow respected for bones in CT. However,

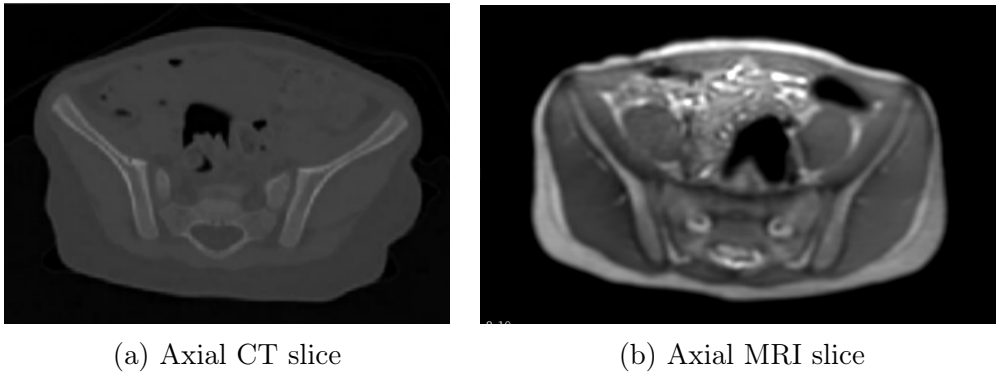


Figure 3.1: Comparison between pelvic CT and MRI images.

even if global thresholding generally leads to a raw but coherent approximation of the bones, this may not be sufficient to obtain accurate segmentations for clinical applications. For this reason several studies on CT, even if still based on a strong assumption on the bones gray-level intensities, proposed more complex methodologies. For instance, some methods have strongly focused on the pre-processing of the CT images, in order to ease the following intensity-based segmentation procedure. In particular, in [127] the authors propose to use a combination of high and low pass filters, specifically designed for non isotropic images, in order to enhance the bones regions while smoothing the other isolated hyperintense components of the image. Global thresholding and morphological operations are then used for final segmentation and separation between the femur and the pelvis. A similar approach was used in [118], in which the author propose to enhance the pelvic bones using wavelets filtering and morphological operations and to use region growing for segmentation.

Some other methods relied also on the image boundaries information. In [43], the authors propose a level-set for the segmentation of the bones in 3D CT data, with a particular focus on the femurs and the vertebral bodies. In particular, they propose to use an energy formulation that incorporates both intensity and boundaries features, and to use a mechanical-based model for automatic detection of small spurious bridges between separated bones. A similar approach, focused on the interface problem between the femurs and the acetabulum, was proposed in [63]. In this case, a bone boundary enhancement filtering is followed by a graph-cuts approach using intensity and boundary based terms. A final post-processing, based on morphological erosion, is then used to identify and separate the femurs and the pelvis.

While the previous studies were applied to adult patients, in [6] and [7] the authors focused on pediatric patients. In particular, in [6] the authors propose to segment the pelvic bones in pediatric CT using opening-by-reconstruction, thresh-

olding and a final refinement using deformable models. The selection of the landmarks needed for the reconstruction procedure requires the prior segmentation of other anatomical structures, such as the peripheral fat, the peripheral muscles and the spinal canal. A similar approach, based on multiple thresholdings and mathematical morphology operations, was proposed by the same authors in [7] for the segmentation of the spinal canal, the ribs and the vertebrae.

If gray-level intensity information is extremely relevant in CT, this is not the case in MRI. For this reason, some studies on MRI rely on texture information. For instance, in [12] the authors propose to segment the knee bones in MRI using an approach based on the extraction of bones features from the phase of the MRI signal. The multiscale texture features are then combined together and classified in a pixel-wise fashion using a support vector machines (SVM) classifier [117], in order to obtain the final segmentation. Another example is given in [74], using a texture-based geodesic active contour, the texture being represented as the local intensity variance of the image, for the knee bones (femur and tibia) segmentation in 2D MRI. For the same application, in [1] the authors propose a method based on graph-cuts. In particular, a graph-cuts approach, opportunely initialized inside the target bones, is used to obtain a pre-segmentation mask of the target structures. This mask is then refined using mathematical morphology and priors on the bone texture, in order to extract the final tibia and femur 2D masks. Graph-cuts were also used in [16] for the segmentation of vertebral bodies on MRI. In this study, the authors propose to pre-process the image using an anisotropic diffusion filtering and an image intensity correction. Then, a graph-cuts approach is proposed to segment the central sagittal 2D slice of the image.

3.2.2 Methods using shape priors

Atlas-based methods

An anatomical atlas is defined as a labeled image representing the standard anatomy of a certain population. Each label can be either represented as binary mask or a vector indicating the positions of each structure boundary. The basic idea of atlas-based segmentation methods is to register the atlas volume to the target volume and, consequently, to transfer the atlas labels on the target volume, obtaining the final segmentation. An example of the atlas-based methodology is depicted in Figure 3.2.

Due to the shape complexity of the pelvic bones, the use of the prior anatomical knowledge, expressed as anatomical atlases, was shown to be very effective. For instance, in [94] the authors propose to segment the pelvic bones in 3D CT images using the multiscale *morphon algorithm* [62] for the registration phase and to obtain the segmentation mask by label propagation. A very similar strategy for

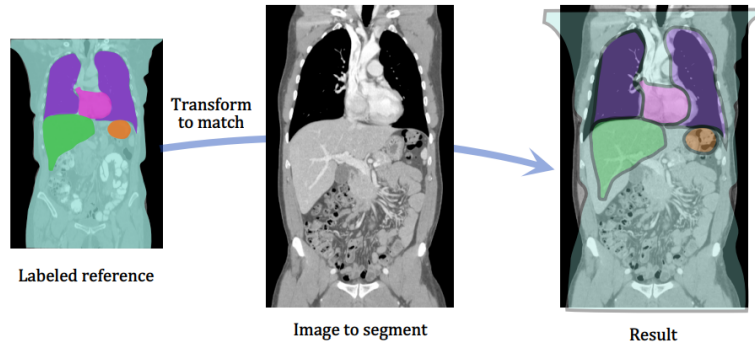


Figure 3.2: Illustration of the atlas-based method principle for an abdominal CT image. Image drawn from [45].

pelvic bones segmentation in 3D CT images was used in [36]. In particular, the authors propose to initialize the registration fitting rigidly the atlas segmentation to a rough segmentation of the target image, obtained by gray-level thresholding. Then, the two images are non-rigidly registered, obtaining the final segmentation by label propagation.

One of the main issues of these methodologies is that the segmentation results are obviously highly dependent on the chosen atlas. Moreover, as the inter-subject variability is not generally taken into account, such methods may give wrong results for structures with high variability or for patients with pathologies [45]. In order to partially solve these problems, some authors propose to use multi-atlas approaches [21, 128]. In [128], the authors propose to use several atlases, obtained by different reference images, for the segmentation of pelvic bones in MRI images. Each atlas of the dataset is first registered to the target image. Then, atlases that generate the most accurate registrations (normalized mutual information is used as similarity measure) are selected and the corresponding labels are propagated to the target image. Finally, the labels are combined together in order to obtain the final segmentation. A very similar approach was proposed in [21] for segmentation of pelvic bones and femurs in CT images. In particular, the authors propose to initialize the registration thanks to a set of automatically extracted landmarks and to refine the final segmentation thanks to a graph-cuts method.

However, image registration, especially in 3D, could be very time consuming. For this reason some authors proposed to substitute this procedure with deformable models approaches. For instance, in [48] the authors propose to segment jointly the pelvic bones, the femurs and the leg muscles in MRI starting from a musculoskeletal template. In particular, the anatomical template is registered to the image thanks to some user-selected landmarks, obtaining a 3D mesh which serves as initialization for a deformable model approach which includes non-intersection

constraints between the different structures. A very similar approach was proposed in [5] for the femur segmentation in MRI images.

SSM-based methods

A statistical representation of an object is formed by identifying a set of landmark points, or eventually a mesh, on an object boundary and by analyzing the variation of each landmark across a set of training images. Constructing a statistical shape model (SSM) basically consists in extracting, through principal component analysis (PCA), the mean shape and a number of modes of variation from a collection of training samples (see Figure 3.3). For further details, an extensive review on statistical shape models can be found in [51].

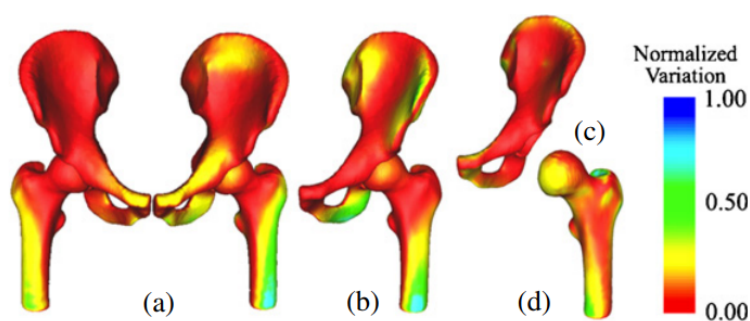


Figure 3.3: Hip bone shape models built from the 3D models of 28 adult patients. The color map illustrates the normalized variation of the primary mode: (a) the bilateral hip SSM; (b) the unilateral hip SSM; (c) pelvic bone SSM; (d) femur SSM. Image drawn from [128].

The ability of the SSMs to incorporate the anatomical shape variations is a strong advantage with respect to the anatomical atlases, which often represent only the mean shape of a given structure, and several applications were developed for pelvic bones segmentation.

The most usual segmentation strategy consists of a first registration of the mean shape of SSM to the target image and on a deformable model, whose evolution is constrained on the image space defined by the SSM. For instance, this kind of approach was used in [65] for pelvic bones segmentation in 3D CT images. The authors propose to manually register the SSM to the target image thanks to a set of user selected landmarks. The final segmentation is obtained through a deformable model, whose evolution is guided by a set of edge points obtained by thresholding the CT image. A similar registration approach was proposed in [102] for pelvic bones and femurs segmentation in 3D MRI images. However, in this study, the authors propose a multi-stage deformable model, in which at each stage the forces

that guide the deformable model evolution are modified by decreasing the SSM contribution and increasing the image-based one. This kind of strategy, aiming to reduce the shape constraints on the final segmentation step in order to have better local results, was also employed in [104] for pelvic segmentation in CT and, by the same authors, in [105] for knee bones segmentation in MRI.

While the previous studies were mostly focused on the final step of the segmentation procedure (the deformable model evolution), some studies focused on more complex ways of building the SSMs. For instance, in [136] the authors propose to use a multi-object hierarchical SSM to jointly segment the pelvis and the femurs in CT images, ensuring non overlapping constraints between the structures while ensuring good local results. In [133], the authors propose to generate a SSM of the pelvic bones that incorporate both shape and gray-level intensity variations in CT images, in order to ease the registration with the target image. Finally, in [19] the authors propose a modified version of a standard SSM which allows focusing on the shape variations of predefined anatomical regions, by manually assigning different weights to the SSM points.

3.2.3 Discussion

CT is the most widely used imaging modality for bones segmentation. Many successful studies were developed for adults and, more rarely, for pediatric patients. Due to the hyperintense nature of the bones in CT, most of the studies use intensity-based approaches and are very difficult to extend to MRI. For this reason, studies on MRI generally rely on the texture information of the bones. However, these approaches were applied to 2D images and to bones with easy shapes, such as the knee and the vertebral bodies. Moreover, since these methods are dedicated to adult patients, they do not take into account the bones texture variability during growth.

Several methods based on anatomical shape priors, in terms of atlases of SSM, were successfully applied to pelvic bones segmentation, both in CT and MRI. In particular SSM-based methods, able to model shape variation within a given population, were shown to be extremely efficient. However, in order to build a proper SSM, a large number of manually annotated data is needed, which is not easy to obtain in pediatrics. Moreover, due to the strong differences in shape and connectivity of pelvic bones during growth, creating a single SSM could not be trivial (a point to point correspondence between the annotated data have to be ensured [65]) and it could not, eventually, well represent the different growing phase of the children.

3.3 Vessels segmentation

3.3.1 Segmentation methods

Most of the studies on vessels segmentation are applied to angiographic images, such as CTA and MRA (an extensive review can be found in [61] and [69]). These image modalities often rely on the injection of a contrast agent and specific acquisition protocols, producing vessels enhanced images (see Figure 3.4a). In case of MRA and CTA, acquisitions are often calibrated such that vessels gray-level intensities correspond to predefined intensity ranges. This property was effectively incorporated in various intensity-based methods. In [11], the author propose to segment vessels in angiographic images through a region-growing technique based on a fixed intensity threshold. Nevertheless, angiographic images often suffer from non-uniformly distributed contrast agent inside the vessels, especially in small vessels. Therefore, in badly conditioned images, the application of a global threshold is not a sufficient approach for the segmentation of the vessels. In this context, in [134] the authors propose a competitive region-growing method, which takes into account both vessels and background intensity information and uses locally adaptive thresholds for segmentation.

Many methods for vessels lumen segmentation also rely on active contour formulations, both parametric [81, 84, 113, 135] and non-parametric [28, 75, 98, 119]. When using parametric active contours, the contour evolution is often constrained by previously detected vascular centerlines, which are normally detected starting from a set of user-selected seeds (e.g. using minimal paths techniques [72]). For instance, in [84] the authors propose a 3D parametric active surface method, where the surface evolution is axially constrained with respect to the vessels centerline curve. A similar method is proposed in [135], introducing a deformable tubular model, where a surface mesh is optimized with respect to the centerline curve. Another example is given in [53], in which the authors propose to segment vessels lumen in 3D images using 2D snakes evolving in perpendicular cross-sections of the vessels centerlines.

A big amount of research work is also dedicated to the design of vessels enhancement filters for angiography images, mainly based on the anisotropic and hyperintense nature of the vessels, which can be used to ease the segmentation procedure. For instance, in [42] and [101], the authors propose to analyze the image Hessian matrix, which incorporate the multi scale second order local structure of the image. A measure of vessel likeliness is then extracted as a function of the Hessian eigenvalues. Other popular vessels enhancement filters are based, for instance, on the spatial covariance of image gradients vectors [66] and on anisotropic diffusion schemes [47]. A comparative analysis of the effects of the vessel enhance-

ment filters images on the segmentation accuracy of an intensity based algorithm can be found in [95].

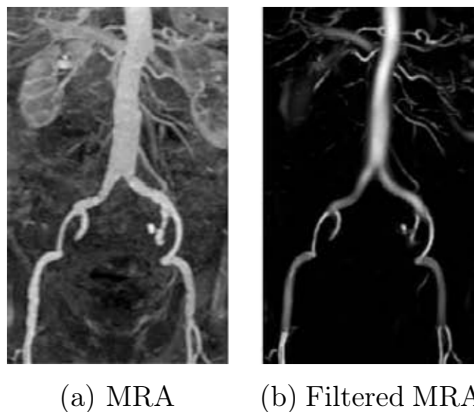


Figure 3.4: Example of vesselness filtering [42] on a MRA volume (maximum intensity projection). Images are based on material from [42].

The tubularity feature of the vessels was also used in many studies to post-process the segmentation results. For instance, in [37], the authors propose to generate, from a collection of 2D cross-sectional vessels segmentations, 3D surfaces as generalized cylinders. It is important to remark that this cylindrical representation of the vessels could not be valid for big vessels, eventually highly collapsed due to their non rigid musculature, such as the vena cava. Other kinds of post-processing approaches rely, for example, on skeletonization techniques and subsequent pruning strategies to remove spurious vessels branches.

3.3.2 Discussion

A large number of studies addresses the problem of vascular segmentation in angiography images. These image modalities often rely on the injection of a contrast agent and on specific acquisition protocols, producing vessels-enhanced images. However, the use of contrast agents is not always recommended in clinical practice, especially for pediatric patients [111]. For this reason, standard MRI acquisitions (see Chapter 2 for further details) are usually chosen for pediatric pelvis exams. The use of standard MRI makes it difficult to apply the methods developed for angiography images, since these images are specifically designed for strong vessels enhanced images. Moreover, for pediatric patients, there are harder clinical constraints on the scan acquisition time than for adults, which do not allow the physicians to considerably increase the images resolution. This, coupled with a smaller size of the vessels walls for pediatric patients, produces images with higher partial volume effects compared to adults. Finally, most of the existing studies

do not address the problem of labeling the vessels into vein and arteries, which is essential for surgical planning applications.

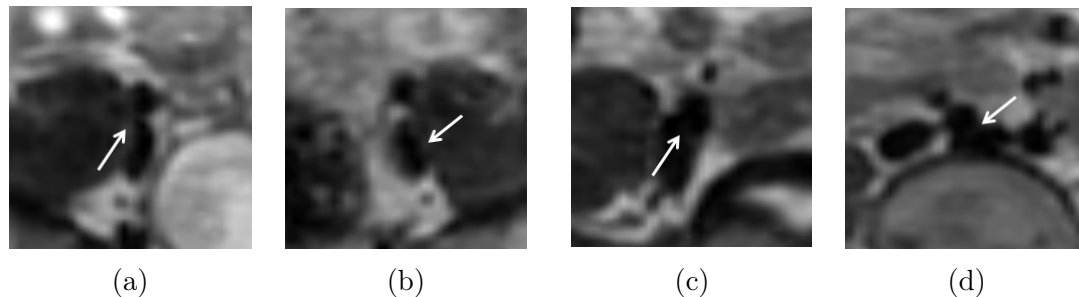


Figure 3.5: Examples of pediatric T2-w MRI slices, focused on the vessels regions. White arrows indicate missing boundaries between the vessels and the surrounding tissues (a, b) and between the veins and the arteries (c, d).

3.4 Bladder segmentation

3.4.1 Segmentation methods

Different successful methods for the segmentation of the bladder on CT images have been reported in the literature. On the other side, only few studies on MRI images were carried out. As an example, in [14] the authors propose an approach based on watersheds with automatic marker extraction for the segmentation of CT images. The watershed markers are based on the image intensity histogram. In [109], the authors propose a method incorporating both shape and appearance information in a 3D graph cuts framework for the simultaneous segmentation of prostate and bladder. Another interesting approach for CT images is proposed in [25]. In this study, the authors propose to identify first a region of interest (ROI) that contains the bladder, starting from a model of the already segmented pelvic bones. Secondly, a pre-segmentation mask is obtained using a modified version of seeded region-growing that also incorporates mathematical morphology operations. Finally a parametric deformable model, using the pre-segmentation as initialization, is used to obtain the final segmentation result. The idea of region growing for bladder segmentation was also proposed in [79] for CT images and in [92] for MRI images. In [44] the authors propose to segment the bladder on T1-w MRI images using deformable models and also relying, in their formulation, on prior knowledge about the bladder intensity. In all the previous methods, the bladder has been segmented considering only the border corresponding to the inner wall of the bladder, assuming that the thickness of the wall is negligible. However,

this assumption is only if the bladder is completely full of urine. Therefore, some methods have been proposed to segment both the inner and outer walls of the bladder, using active contours methods. In [35] a coupled level-sets framework for segmentation of the bladder wall on T1-w MR images is proposed. Starting from the inner bladder segmentation, the authors propose to segment the outer bladder wall using a level-set, whose energy formulation is based on a regional adaptive clustering algorithm. However, even if particularly interesting, this methodology seems computationally expensive [44]. A similar segmentation strategy for 2D T2-w was proposed in [76]. In particular, in this study some prior information on the bladder wall thickness is incorporated, in order to segment the outer bladder border.

3.4.2 Discussion

Several methods for bladder segmentation were developed, especially for CT images. However, even if these techniques led to promising results, they are not easy to extend to MRI images, due to the different intensity representations of the two modalities. For this reason, specific methods were developed for MRI. However, intensity based methods, such as the ones that rely on region-growing techniques, could be very sensitive to intensity inhomogeneities, such as the ones generated by MR bias fields. Active contours, especially level sets methods, appears to be the best solution for bladder segmentation in MRI. However, none of the existing methods was tested on pediatric patients, which present higher intensity inhomogeneities and higher partial volume effects. Finally, segmentation methods for the outer wall of the bladder were reported as computationally expensive or applied to high resolution 2D images.

3.5 What about deep learning?

In the last years, deep learning methods and in particular convolutional neural networks (CNN) have shown excellent performances in various medical imaging tasks [23, 33, 60, 73, 83]. However, deep learning methods usually require a huge number of manually annotated data, which is really difficult to obtain in the medical field, and especially in pediatrics. To partially bypass this constraint, recent studies [8, 77, 106, 131] have relied on transfer learning [90] from pre-trained networks on large datasets of natural images (e.g. ImageNet [27]). However, these studies cannot be directly applied to volumic data, due to the nature of the training dataset (e.g two-dimensional (2D) color images for ImageNet). Moreover, discarding the 3D nature of medical images would result in a loss of useful information for the segmentation task. For this reason, some studies [106, 131] successfully pro-

posed to generate 2D pseudo-color images from volumeic gray-level images, aiming to incorporate 3D information. This is the line adopted in Chapter 6 for vessels segmentation.

3.6 Discussion

As reported in this chapter, very few segmentation methods were developed for pelvic structures in pediatric images. In fact, the segmentation task is more difficult in pediatric images than in adult images because of the nature of the target structures (e.g. shape variability during growth, high partial volume effect) and harder constraints on the imaging acquisitions (e.g. no CT or angiography acquisitions, low image resolution).

However, despite the strong lack in organ-specific segmentation methods for pediatrics, several generic medical image processing platforms are freely distributed as open-source software. These platforms, thanks to different segmentation tools (e.g. region growing, active contours, graph-cuts), aim to speed up the segmentation procedure compared to the fully manual annotation of the images. In order to understand whether these generic segmentation tools could fit to the time constraints required by the clinical practice (less than 2 hours for a full 3D segmentation), a comprehensive review of these open source software is essential. This will be the aim of Chapter 4, which will lead us to the choice of a specific software and its associated programming environment, namely 3D Slicer. The new segmentation methods proposed next, in Chapters 5-7, will be then implemented in this environment.

Chapter 4

3D segmentation and visualization platforms analysis

Abstract

The medical imaging community was very active, in the last decades, on developing and on freely distributing software platforms for image processing and visualization. In particular, generic segmentation tools, aiming the users to speed up the segmentation tasks were implemented in these platforms. For this reason, a comprehensive review of the these software tools, in order to evaluate their performances on pelvic MRI segmentation, is essential. In this chapter, twelve software tools, freely available on the Internet, were evaluated using T2-w volumic MRI and diffusion-weighted MRI images. The software tools were rated accordingly to eight criteria, evaluated by three different users: automatization degree, segmentation time, usability, 3D visualization, presence of image registration tools, tractography tools, supported OS, and potential extension (i.e. plugins). A ranking of software tools for 3D modeling of MRI medical images, according to the set of predefined criteria, is given. This ranking allowed us to elaborate guidelines for the choice of software tools for pelvic surgical planning in pediatric patients. The best-ranked software tools were Myrian Studio, ITK-SNAP and 3D Slicer, the latter being especially appropriate if nerve fibers should be included in the 3D patient model. Finally, 3D Slicer was also chosen as core software platform for developing the organ-specific segmentation methods for pediatric patients (Chapters 5, 6 and 7).

Contents

4.1	Introduction	29
4.2	Software tools evaluation	29

4.2.1	Software tools selected for evaluation	29
4.2.2	Imaging dataset	32
4.2.3	Evaluation criteria	33
4.3	Results	35
4.4	Discussion	39
4.5	Conclusion	44

4.1 Introduction

Our aim in this chapter is to evaluate existing segmentation software tools for pediatric pelvic MRI segmentation. The evaluation is performed according to our requirements in terms of daily surgical use of 3D modeling of children with abdomino-pelvic tumors and malformations, e.g. with a limited number of image processing steps. We present here the selected software tools (Section 4.2.1), we propose a set of criteria (Section 4.2.3) for comparative analysis (Section 4.3), and we provide surgeons and researchers with guidelines for choosing software (Section 4.4).

4.2 Software tools evaluation

4.2.1 Software tools selected for evaluation

This survey focuses on the most generally used software tools in the medical image community, in particular by radiologists. We only include the software tools equipped with segmentation tools, 3D rendering tools and that are usable by a non expert in image processing. All the analyzed software tools are freely available on the Internet, except for two commercial software tools currently used at the Imaging Department of the pediatric Hospital Necker-Enfants Malades of Paris. All free software tools were tested on a Windows OS (CPU at 3.10 GHz, 16 GB RAM, 64 bit OS), except for the OsiriX DICOM Viewer that was tested on a Macintosh OS (CPU at 2.7 GHz, 16 GB RAM, 64 bit OS). The possibility of running the software tools on different operating systems, in particular Linux, was also analyzed. The selected software tools and the corresponding releases are listed in Table 4.1.

3D Slicer 3D Slicer [38] is a free, multi-platform and open source software for image analysis and visualization written in C++, Python and Qt¹. The origin of this software was a project between different laboratories of the Brigham and Women's Hospital and the MIT in 1998. In the following years, several improvements of the software capabilities were achieved through the support of the National Institute of Health (NIH). The main interface of 3D Slicer appears as a typical radiology workstation, allowing for a large number of different visualization configurations to analyze 2D, 3D and four-dimensional (4D) images. The platform also offers a large set of processing tools for different imaging modalities and applications (including segmentation, registration, quantification).

¹<https://www.qt.io/>

Software	Release	Cost	URL
3D Slicer	4.5.0-1	free	http://www.slicer.org/
Anatomist	4.0.0	free	http://brainvisa.info/web/anatomist.html
AW-Server	3.2	\$	http://www3.gehealthcare.com/en/products/categories/advanced_visualization/platforms/aw_server
Freesurfer	5.3.0	free	http://surfer.nmr.mgh.harvard.edu/
FSL	4.0.1	free	http://www.fmrib.ox.ac.uk/fsl
ImageJ	1.50b	free	http://imagej.net/
ITK-SNAP	3.4.0-beta	free	http://www.itksnap.org
Mango	4.0.1	free	http://ric.uthscsa.edu/mango/
MedInria	2.2.3	free	http://med.inria.fr/
MIPAV	7.2.0	free	http://mipav.cit.nih.gov/
Myrian Studio	2.2.1	free	http://studio.myrian.fr/
Olea Sphere	3-0	\$	http://www.olea-medical.com/en/olea-sphere-3-0/
OsiriX	5.8	free	http://www.osirix-viewer.com/
Seg3D	2.2.1	free	http://www.sci.utah.edu/software/seg3d.html

Table 4.1: Selected softwares. Commercial tools are indicated with a \$ in the cost column.

Anatomist Anatomist [97] is the visualization software generally associated with the software platform BrainVISA[46]. BrainVISA is an open-source software written in Python, offering different tools dedicated to the neuroimaging research and mainly developed by the French Alternative Energies and Atomic Energy Commission (CEA). Although BrainVISA is devoted to brain MRI, Anatomist can be used to visualize and segment other types of image volumes.

AW-Server AW-Server is the commercial visualization software developed by GE Healthcare. The workstation, more than just allowing for the visualization and annotation of the images, offers a large number of advanced post-processing applications for different imaging modalities and clinical applications.

Freesurfer Freesurfer [40] is an open source software platform, written in C++, developed by the Martinos Center for Biomedical Imaging of Boston. The software is particularly devoted to the analysis and visualization of structural and functional neuroimaging data, offering several tools for the automated segmentation of anatomical MRI images and the analysis of diffusion MRI data. Despite the strong focus on brain MRI, Freesurfer can be used to visualize and analyze through generic tools various types of multi-dimensional medical images.

FSL FSL (the FMRIB Software Library) [59] is an open source software library, written in C++, mainly developed by the FMRIB Analysis Group of the University of Oxford. The software is strongly devoted to the analysis of functional, structural and diffusion MRI brain imaging data. Similarly to Freesurfer, although FSL is strongly devoted to the brain MRI data, it offers a generic viewer (FSLView) that allows visualizing and manually segmenting 3D images.

ImageJ ImageJ [103] is a Java-based, open source platform for image processing, developed by the NIH and constantly updated since 1997. Thanks to the collaborative efforts of its developer community, ImageJ offers several functionalities for performing a wide variety of image processing tasks. However, even if ImageJ supports multidimensional data, it appears more focused on the processing of 2D images.

ITK-SNAP ITK-SNAP [138] is an open source software application based on ITK² and VTK³ C++ libraries. It was developed by the University of Pennsylvania and the University of Utah, first released in 2004 but under a constant updating process. The platform allows for navigation within the images similarly to a radiology workstation, and it was specifically developed for segmentation tasks, not focusing on other kinds of processing (e.g. filtering, registration).

Mango Mango (Multi-image Analysis GUI) is a free Java-based viewer for medical images developed by the Research Imaging Institute of the University of Texas Health Science Center at San Antonio. The software includes a graphical user interface (GUI) for the visualization of 3D images as well as functionalities for different tasks such as registration, filtering and segmentation. It can be extended through dedicated plugins.

MedInria MedInria [114] is an open source platform for medical image processing developed by Inria, the French National Institute for computer science and applied mathematics. This platform manages the visualization of multidimensional data, and it includes processing and analysis of diffusion MRI images (e.g. to provide tractography). MedInria also offers basic segmentation, registration and filtering tools based on the ITK library.

MIPAV MIPAV [80], acronym for Medical Image Processing Analysis and Visualization, is a Java-based open source software supported by the NIH. It manages

²<https://itk.org/>

³<http://www.vtk.org/>

multimodal and 3D images, even if its main interface appears better suited for the processing and visualization of 2D images. MIPAV offers several functionalities for different tasks such as filtering, registration and segmentation on both 2D and 3D images.

Myrian[®] Myrian[®] is a commercial software for medical image processing and visualization developed by Intrasense. It supports multimodal images and offers different functionalities for tasks such as segmentation, quantification and registration. A non-commercial version, Myrian[®] Studio, is freely available for research purposes and can be extended through dedicated plugins.

Olea Sphere[®] Olea Sphere[®] is a commercial processing platform for CT and MRI, developed by the company Olea Medical. The workstation includes a generic DICOM viewer and offers different packages developed for specific medical applications (e.g. breast, head and neck, prostate).

OsiriX OsiriX [100] is one of the most widely used DICOM viewers in the medical community. The OsiriX project started in 2003 at UCLA, Los Angeles, and in 2010 the first commercial version of the software (OsiriX MD) was released. OsiriX Lite is the free version of the commercial software OsiriX MD, intended for research purposes and offering reduced computational performances, but it still includes the functionalities needed in our application domain. The platform appears as a typical radiology workstation, supporting multimodal images and strongly devoted to the visualization tasks, even if it includes also post-processing tools such as registration and segmentation.

Seg3D Seg3D [22] is an open source software platform for image visualization and segmentation of 3D images developed by the NIH Center for Integrative Biomedical Computing at the University of Utah. The platform focuses on segmentation tasks, even if some other functionalities such as filtering using several methods from the ITK library are present.

4.2.2 Imaging dataset

Softwares were evaluated on imaging data issued from the complete patient's cohort except for the segmentation time criteria, which is highly dependent on the patients' age and pathology. We have thus chosen two adolescent patients with a normal pelvis anatomy, one female and one male of the same age (to take into account gender variation) to evaluate this criterion. Segmentation was performed with all softwares for these two referent patients. Finally, in order not to bias

the segmentation time results, images having both the same acquisition parameters were chosen for these two patients: echo time $TE = 59\text{ ms}$, repetition time $TR = 5716\text{ ms}$, flip angle $FA = 90^\circ$, image size $512 \times 512 \times 208$ voxels, and voxel size $= 0.74 \times 0.74 \times 0.70\text{ mm}^3$.

Diffusion-weighted (DW) MRI scans, acquired immediately after the T2-w acquisitions were used to test the tractography algorithms, in order to minimize the potential patient's displacement between the two scans. The DW MRI was acquired in the axial plan with a sequence of 25 directions, a b-value of 1000 and a voxel size of $1.4 \times 1.4 \times 4\text{ mm}^3$.

4.2.3 Evaluation criteria

In order to evaluate the performances of the software tools on the segmentation of the abdominal and pelvic structures in pediatric MRI, we established a list of eight criteria: automatization degree, usability, 3D visualization, segmentation time, image registration functionalities, tractography functionalities, supported system and potential addition of plugins. They are defined in this section.

Automatization degree This criterion was analyzed according to a score defined by the amount of manual interaction required by the user. Score 1 was assigned to a totally manual segmentation of the regions of interest, performed slice by slice; score 2 to the presence of generic semi-automatic tools for the segmentation of the 2D slices; score 3 to the presence of generic semi-automatic tools for the segmentation of a 3D region; score 4 to the presence of semi-automatic tools optimized for a specific anatomical structure. Note that thresholding-based segmentation tools were present in all the analyzed software tools. In this study, we did not consider them as segmentation tools due to the fact that they do not provide suitable results for any structure of interest in the abdomen and the pelvis, especially in MRI, where no equivalent of the CT Hounsfield units exists.

Segmentation time The time required for the segmentation of the pelvic structures of interest in T2 MRI of two test patients (one male and one female) was evaluated for each analyzed software. The two images had the same features in terms of contrast, size, resolution, and the patients had the same age and the same anatomical complexity (see Section 4.2.2 for further details). Consequently, we can assume that the only factor that could generate a relevant difference on the total segmentation time is given by the different anatomy of the genital system. For this reason the total segmentation time was evaluated for the male patient (bones, bladder, vessels, rectum, prostate, seminal vesicles). For the female patient, only the uterus was segmented and the segmentation time was compared to the one

needed for the segmentation of the genital system of the male patient (prostate and seminal vesicles). The segmentations were carried out using either manual or semi-automatic tools depending on the availability in the software tools. In both cases, the aim was to obtain a satisfying segmentation result. For this reason, in case the segmentation was obtained through semi-automatic tools, the segmentation time also includes the time needed for potential manual corrections of the segmentation. In order to obtain a comparable segmentation among the different software tools, our aim was to obtain results as close as possible to a reference manual segmentation performed by an expert user. The similarity between the different segmentations was evaluated through the DICE index [31] and the value 0.9 was set as lower limit for our application (a DICE index equal to 1 means exact correspondence between the segmentations).

Usability In order to evaluate the usability of the different platforms, we focused on the ease of use of the GUIs (graphical user interfaces). This includes the general functionalities of the GUI, the ease of use of the manual and semi-automatic segmentation tools, the easiness of the management of the input and output patients data, and the header access. This evaluation was qualitatively and independently performed by three different users (two surgeons and a researcher in image processing), by assigning a score from 1 to 4 (the higher the score, the higher the user’s satisfaction). The median value of the scores was retained as the single final score for each software.

3D visualization The quality of the 3D visualization tools was evaluated. The aspects that mostly interest us are the generation of the 3D models starting from the segmented images, the easy navigation within the 3D model and the availability of tools for the improvement of the quality of the visual representation (e.g. smoothing, lighting, colors and transparency management). Evaluation of 3D visualization, similarly to usability, was qualitatively and independently performed by the same users, by assigning a score from 1 to 4 (the higher the score, the higher the user’s satisfaction). The median value of the scores was retained the single final score for each software.

Image registration The availability of automated registration tools, which are needed to align different MRI scans, was evaluated for each software, assigning a binary positive or negative score. The details of registration tools (e.g. rigid, affine, thin-plate) within each software are not listed, being out of the scope of this survey.

Tractography An efficient way to reconstruct the 3D paths of the nerve fibers is to apply tractography algorithms to diffusion MRI acquisitions. Availability of tractography tools was noted for each software by a binary positive or negative score.

Operating systems Considering that different operating systems (OS) are used in the medical imaging community, the corresponding supported OS was reported for each software and the possibility of running the software tools with different OS was considered.

Potential extensions The ability of the software tools to be freely extended by add-ons or plugins was considered as important criteria. For each software, in order to understand the different development strategies to extend their capabilities, we report whether they are open-source or not, the different programming languages to use to eventually develop the extensions, and the availability of documentation (such as wiki pages or tutorials) and forums or mailing lists focused on the development issues.

4.3 Results

The performances of 14 segmentation software tools (12 free software tools and 2 commercial software tools) described in Section 4.2.1 were analyzed. The results given by the analysis of the software performances, according to the criteria described in the previous section, are summarized in Table 4.2 (7 first criteria), Table 4.3 (comparison of the segmentation time for the different structures between male and female patients), and Table 4.4 (last criterion on plugins).

Automatization degree In all the analyzed software tools, except for Anatomist, FSL and Mango, different generic semi-automatic segmentation tools were present. In particular the highest automatization degree score was assigned to 3D Slicer, AW-Server, ITK-SNAP, MedInria, Mipav, Myrian Studio, Olea Sphere and OsiriX. This means that all these software tools include at least one semi-automatic tool for the segmentation of a 3D region, 3D Slicer being the one that offers the largest number of segmentation tools (both 2D and 3D). As shown in Table 4.2, none of the software tools includes organ-specific tools dedicated to the segmentation of the pelvic structures of interest in MRI. However it is important to note that some of the software tools (e.g. 3D Slicer, Myrian Studio, Freesurfer, FSL) have organ-specific segmentation tools for other anatomical structures (e.g. brain, liver, lungs) or for other imaging modalities (e.g. CT, microscopy).

Software	Automatization	Usability	3D Vis.	Segm. time	Registration	Tractography	OS		
							Windows	Linux	Macintosh
3D Slicer	3	3	4	15h	x	x	x	x	x
Anatomist	1	1	1	>25h			x	x	x
AW-Server	3	3	3	>20h	x	x			x
Freesurfer	2	2	1	>20h	x	x		x	x
FSL	1	1	2	>25h	x	x		x	x
ImageJ	2	2	1	>25h	x		x	x	x
ITK-SNAP	3	4	4	10h			x	x	x
Mango	1	3	2	>20h	x		x	x	x
MedInria	3	3	3	>20h	x		x	x	x
MIPAV	3	2	2	>20h	x		x	x	x
Myrian Studio	3	3	4	9h	x		x		
Olea Sphere	3	3	4	>20h	x		x	x	x
OsiriX	3	3	4	>20h	x				x
Seg3D	2	4	3	20h			x	x	x

Table 4.2: Software comparison.

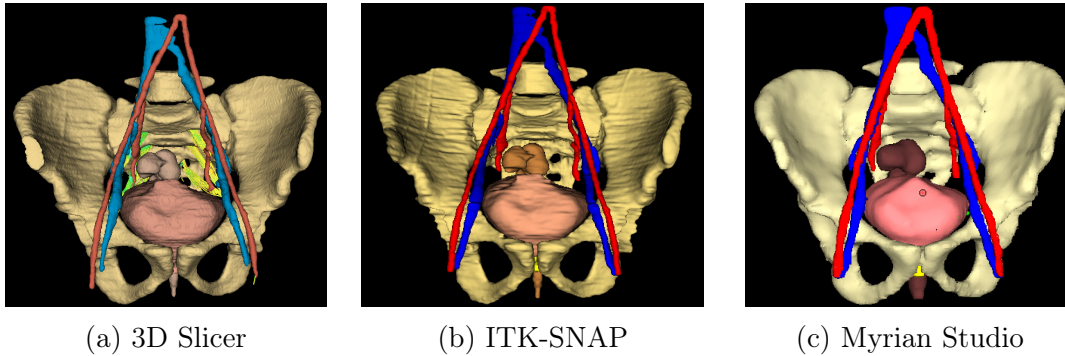


Figure 4.1: Example of 3D pelvic reconstructions obtained through segmentation of the volumetric T2-w MRI.

Usability Our analysis ranks ITK-SNAP and Seg3D as the best tools in terms of usability. These software tools present a clear and intuitive GUI and the number of user interactions (clicks or selection) generally needed to perform a given operation is really limited. In particular they easily allow the user to import the patient data, to access to its information, to perform the segmentation tasks, and to finally save the processing results. The two software tools that obtained the lower score were Anatomist and FSL. The main reason is that they are mostly dedicated to users with a certain image processing background, and they actually do not focus on generic segmentation tasks.

3D Visualization The software tools that obtained the best score were 3D Slicer, ITK-SNAP, Myrian Studio, Olea Sphere and OsiriX. These software tools allow the user to obtain, once the segmentation task is performed, the 3D models of the segmented regions and to easily navigate in the 3D views. Moreover, these software tools offer several tools for the management of the 3D surfaces such as opacity and lighting, that clearly improve the visual quality of the visualization of the 3D models. On the other side, the lowest score was assigned to Anatomist, Freesurfer and ImageJ, mostly due to the not intuitive steps needed to obtain the 3D models from the segmented images.

Segmentation time As shown in Table 4.2, the time required for the segmentation of the structures of interest of our male test patient (bones, colon, bladder, main vessels, prostate) is always at least 9 hours. In particular, Myrian Studio is the software that gave the best segmentation time. The complete reconstructions of all the structures of interest were performed using only four of the analyzed software tools (3D Slicer, ITK-SNAP, Myrian Studio, Seg3D) and, consequently, the exact segmentation time is reported only for them. Using the other software tools,

Software	Segmentation Time [min]	
	Male	Female
3D Slicer	7	19
Anatomist	13	28
AW-Server	8	20
Freesurfer	11	28
FSL	12	26
ImageJ	10	25
ITK-SNAP	6	18
Mango	9	20
MedInria	10	20
MIPAV	11	26
Myrian Studio	4	11
Olea Sphere	9	21
OsiriX	8	18
Seg3D	8	19

Table 4.3: Segmentation time for the genital system.

due to the long time needed for the segmentation, only a few structures have been segmented. In these cases, the time for the complete segmentation is estimated (in Table 4.2 the lower bound is reported) by considering both the time needed to fully segment the first structures and the time needed to partially segment the other structures. As shown in Table 4.3, the segmentation time needed for the segmentation of the female genital system was, for all the software analyzed, higher than for the male one.

Registration tools All the software tools, except Anatomist, Seg3D and ITK-SNAP, include image registration tools. In particular, 3D Slicer is the one that offers the largest number of different image registration tools.

Tractography tools Tractography algorithms that allow to track the nerve fibers from the diffusion MRI are present in 3D Slicer, AW-Server, Freesurfer, FSL, MedInria, MIPAV and Olea Sphere. In Figure 4.1 the full pelvic 3D reconstructions obtained using 3D Slicer, ITK-SNAP, Myrian Studio are shown.

Additionally, the nervous pelvic network was added on the 3D Slicer segmentation view since it could be obtained using this software.

Potential extensions As reported in Table 4.4, all the software tools, except the two commercial software AW-Server and Olea Sphere, can be freely extended by independent developers, in order to improve the performances of the basic versions of the software. The development of extensions is, in most of the cases, supported by specific documentation and forums, and different programming languages can be used.

Software	Extensible	Open-source	Documentation	Forum	Programming language
3D Slicer	x	x	x	x	C++, Python, Matlab
Anatomist	x	x	x	x	C++, Python
AW-Server		-	-	-	-
Freesurfer	x	x	x	x	C++
FSL	x	x	x	x	C++
ImageJ	x	x	x	x	Java, Javascript, Python, Matlab, Ruby, Groovy, Lisp, R
ITK-SNAP	x	x		x	C++
Mango	x		x	x	Java, Python
MedInria	x	x	x	x	C++
MIPAV	x	x	x	x	Java
Myrian Studio	x		x	x	C++, Matlab
Olea Sphere		-	-	-	-
OsiriX	x	x	x	x	Objective C
Seg3D	x	x	x	x	C++, Python, Matlab

Table 4.4: Development features.

4.4 Discussion

The time required for the segmentation is surely the most important factor to consider in our evaluation. Even if the segmentation time is obviously related with the automatization degree of the software, it gives better information about the real performances of the segmentation tools. In some cases, the semi-automatic segmentation tools did not allow obtaining suitable results for all the structures of interest, and time-consuming manual corrections had to be done. For example, using AW-Server, MedInria, MIPAV, OsiriX and Olea Sphere, the 3D semi-automatic

tools had suitable performances only on the bladder segmentation and the rest of the organs were manually segmented. None of the analyzed software tools respected the segmentation time limits imposed by the clinical practice. However, the fastest segmentation results were obtained using Myrian Studio and ITK-SNAP. In particular Myrian Studio offers, within its various segmentation tools, a powerful tool to interpolate several manual segmentations on the 2D slices to obtain a 3D segmentation, strongly reducing the segmentation time of all the structures of interest. The segmentation time with ITK-SNAP was also shorter than for the other software tools, although slightly higher than the former. It benefits from a powerful and interactive 3D segmentation tool based on deformable models implemented in level-set algorithms. Even if this tool was not suitable for all the structures of interest, it allowed shortening the segmentation time for the bones and the bladder.

Both ITK-SNAP and Seg3D appear really usable, thanks to clear interfaces and to intuitive segmentation tools. The easy use is especially guaranteed by the fact that these software tools have a limited number of functionalities and that they are strictly dedicated to segmentation problems. Software tools such as 3D Slicer, AW-Server, Olea Sphere and Myrian Studio are also really usable but slightly less than the formers, due to a larger number of screen configurations and tools offered for various tasks (e.g segmentation, filtering, analysis, registration and tractography tools). It is important to remark that, as our team did not have previous experience of any of the software tools analyzed, the influence of the learning curve for each software was not considered. However, we can expect that all computation times would be reduced after user's training. Regarding the segmentation process, the main difficulties were strongly related to each anatomical structure (see Figure 4.2):

- The structure that raises the biggest segmentation difficulties is the colon, due to its complex 3D shape and the strong inhomogeneities induced by the presence of both air and matter. Moreover, on T2-w images, there are often unclear boundaries between the colon and the surrounding perirectal fat (Figure 4.2a). Hence its segmentation is guided by a prior anatomical knowledge in addition to the image information.
- The bones, even if not totally homogeneous, are better suited to be segmented with semi-automatic tools than the colon. Anyway, due to the large volume that they occupy on the image and the not totally suitable results given by the semi-automatic tools (manual correction are needed), the bone structure is the one that requires the longest segmentation time (Figure 4.2b).
- The bladder, appearing on the T2-w images as a homogeneous hyperintense region, is the easiest organ to segment and the available semi-automatic tools

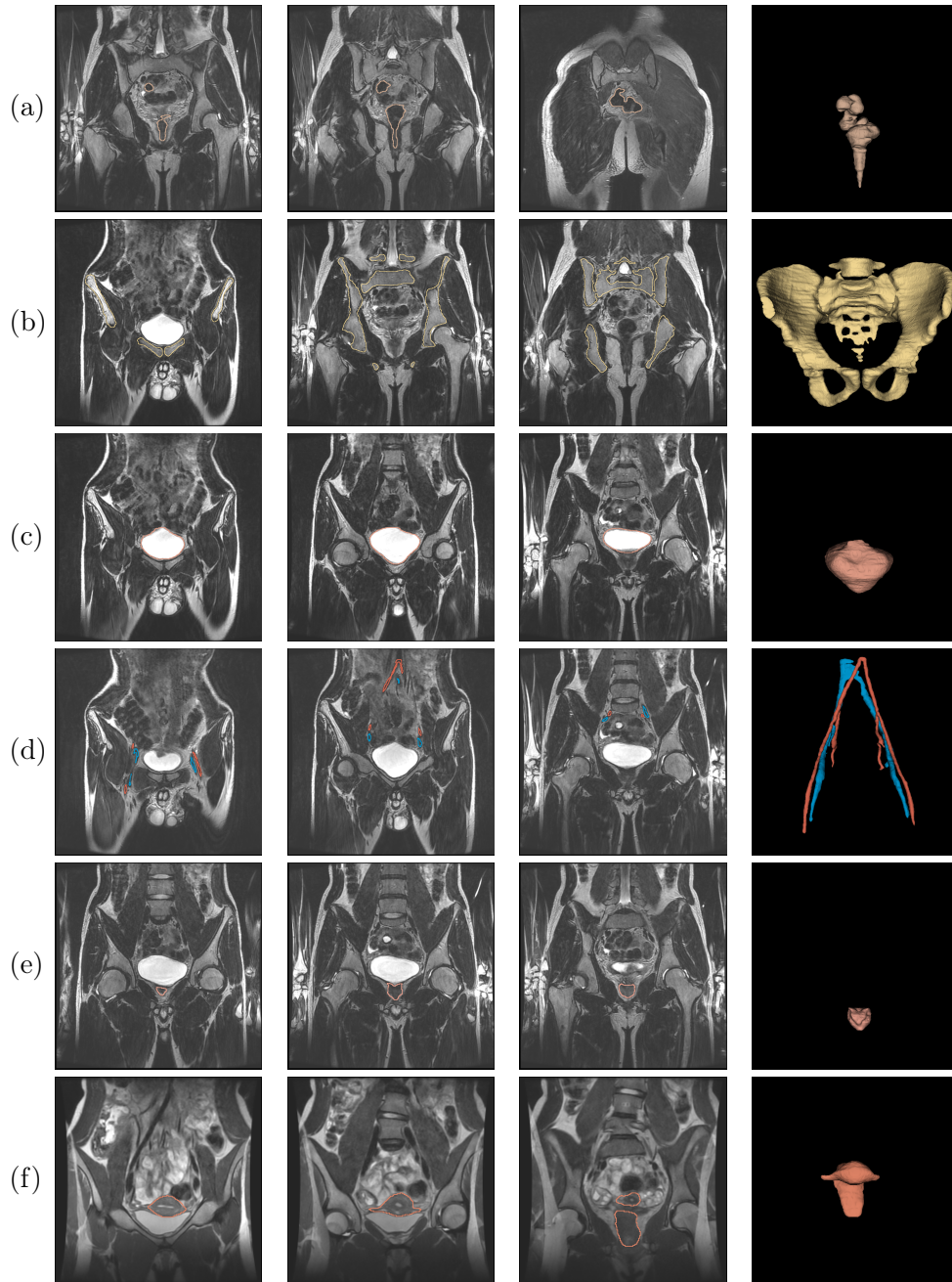


Figure 4.2: Example of organs segmentations in a few MRI coronal slices. From top to bottom: (a) rectum, (b) bones, (c) bladder, (d) veins (blue) and arteries (red), (e) prostate, and (f) uterus.

allow us to generally perform a fast and accurate segmentation. However,

the automatic segmentation tools do not allow taking into account both the bladder repletion (strongly hyperintense) and the bladder wall, that eventually have to be segmented (Figure 4.2c).

- The main pelvic vessels (aortal and vena cava bifurcation, iliac veins and arteries) are not difficult to visually identify but the available semi-automatic algorithms do not allow us to obtain suitable results. The main problems are related to the low contrast between the vessels and the surrounding tissues, and to the unclear boundaries between the veins and the arteries in the regions in which they are partially in contact (Figure 4.2d).
- The segmentation of the prostate and the uterus is difficult due to a poor contrast and not well defined boundaries with the surrounding tissues (Figure 4.2e and Figure 4.2f). The segmentation time for the uterus is higher than for the prostate due to its more complex shape and its bigger volume (67.5 cm^3 for the uterus, against 15.7 cm^3 for the prostate⁴). However, both structures are relatively quickly segmented in comparison to the others due to their limited size.

The problems encountered and the long time required to build the 3D models are thus related to the lack of organ-specific segmentation tools for the structures of interest in any of the software tools tested. For this reason, the extension criterion is crucial in the evaluation of the software potential. The plugins, do not only improve the segmentation performances, but can also be really useful in research works to test and evaluate innovative methods and algorithms. Even if most of the software tools can be extended by add-ons or plugins, as shown in Table 4.4, the ones that appear easier to extend, thanks to their modularity, their extensive documentation, tutorials and support provided for the developers, are 3D Slicer, ImageJ, MIPAV and Myrian Studio.

To conclude this survey, we can sum up some guidelines for the choice of a software for the pelvic surgical planning depending on the final result the user wants to achieve.

If the aim of the user is to obtain the reconstruction of the organs of interest (bones, bladder, colon, vessels, genital system) by segmenting (manually/semi-automatically) the image volumes of the patient, the best-ranked tools, according to our criteria, are ITK-SNAP and Myrian Studio. These two software tools are the fastest in terms of segmentation time, are really usable and offer a good 3D visualization of the segmentation results. Among these two software tools, the advantage of ITK-SNAP is the easier management of the output segmentation models, that can be easily exported in standard formats (e.g. `.vtk`, `.stl`) and

⁴Values estimated from the manual segmentations.

eventually imported in other software environments. Moreover, ITK-SNAP is multi-platform, while Myrian Studio runs only on Windows OS.

However, neither ITK-SNAP nor Myrian Studio offer tractography tools for the 3D reconstruction of the nerve fibers that could be really useful to integrate in the patient-specific 3D model. A possible solution, in order to obtain a complete patient model, could be to generate the segmentation models of the structures of interest within a software (e.g. ITK-SNAP), export the results and subsequently import them in a software that offers tractography tools. However, this procedure requires several steps and it would be clearly better for the user to have all the needed tools in the same software platform. Therefore, if the user also wants to consider the nerve fibers in the final 3D reconstruction, 3D Slicer is the software that best fits our requirements. In fact, even if using 3D Slicer the segmentation time is higher than with ITK-SNAP or Myrian Studio, and the GUI slightly less easy to use than the one of ITK-SNAP, 3D Slicer has good 3D visualization features and has the strong advantage of offering tractography tools. Note that recent versions of 3D Slicer include a better GUI with useful interpolation and visualization tools. Moreover in case of users willing to extend the software capabilities, since 3D Slicer can be easily extended with plugins, the segmentation time could be strongly reduced by implementing organ-specific segmentation methods.

As mentioned in Section 4.2.2, two 16 years old patients with a normal anatomy of the structures of interest were chosen for the evaluation of the segmentation time criterion, in order not to bias the software performances analysis with complex image interpretation issues. Surely, strong malformations raise more difficulties on the segmentation task, and the segmentation time would potentially increase compared to our case. Moreover, in case the user wants also to segment a potential tumor, this additional time has to be taken into account. The amount of the additional segmentation time depends on different factors that cannot be easily quantified, such as the anatomical experience of the user, the seriousness of the malformation or the tumor extension.

Another factor that could impact the segmentation time is the age of the patient. On the one side, considering younger patients will potentially lead to an additional time in the image-understanding task, due to a more complex anatomy. On the other side, with the same acquisition protocol, younger patients also mean less slices and smaller structures to segment. As in the case of pathological patients, the overall effect of these two opposite factors strongly depends on the user anatomical experience.

4.5 Conclusion

In this chapter, we highlighted the differences in performances of different software tools, according to a set of criteria defined for our specific needs in 3D modeling of abdomino-pelvic tumors and malformations in children, from MRI acquisitions. In the literature, few papers reviewed the various software tools able to read DICOM images with the aim of integrating clinical research and medical imaging [50, 71, 115]. In these studies, the authors distinguished open source, free and commercial tools, and analyzed them according to several general criteria such as usability, interface, data management and 2D and 3D viewing tools. In particular, Presti et al. [96], focused on the issues of image-guided surgery, by reviewing different software tools taking also into account the possibility of their integration in a portability workflow till the operating room. However, none of the previous studies considered the segmentation performances of the different software tools.

Thanks to our study we quantitatively demonstrated that none of the analyzed software meets the time criteria for segmentation needed in clinical practice. This clearly justifies the need of developing dedicated segmentation methods for pelvis structures in pediatric MRI. Finally, this study led us to choose 3D Slicer as as core software platform for developing these segmentation methods (Chapters 5, 6 and 7).

Chapter 5

Pelvic bones segmentation

Abstract

This chapter presents a semi-automatic method for the segmentation of the pelvic bones in T2-weighted MRI images. The proposed method consists of two main steps: i) a semi-automatic registration of age-specific bones templates with the target MRI; ii) a segmentation refinement, based on deformable models, that takes into account the local curvature of the pelvic bones. The performances of the proposed approach, validated on a set of 25 T2-w MRI volumes of pediatric patients, were quantitatively and qualitatively appreciated by medical experts. In order to deliver the clinicians with a user-friendly segmentation tool, the proposed method was implemented as a plug-in for the 3D Slicer platform. Finally, a part of this work has been published in [122].

Contents

5.1	Introduction	47
5.1.1	Context	47
5.1.2	Outline	47
5.2	Segmentation method: a template-based approach	47
5.2.1	Generation of anatomical templates	48
5.2.2	Pre-segmentation from closest template registration	48
5.2.3	Refined segmentation using deformable models	50
	Deformable model	50
	Constraints on the surface evolution	51
5.3	Results	52

5.3.1	Landmark selection	52
5.3.2	Qualitative evaluation of the segmentation results	53
5.3.3	Quantitative evaluation of the segmentation results . . .	53
5.4	Conclusion and discussion	59
5.4.1	Contributions	59
5.4.2	Perspectives	60

5.1 Introduction

5.1.1 Context

Pelvic bones constitute a core structure of the pelvis, which serves as a spatial reference for the surgical planning and 3D visualization. Moreover, due to the large volume that they occupy in the pelvic region, pelvic bones are the structures which require the highest time for segmentation when using manual segmentation tools (see Chapter 4).

As pointed out in Section 3.2, most of the existing methods are applied to CT images, using intensity-based approaches, or to adult images using strong shape priors in term of atlases or SSM, without taking into account the bones variability during growth. In this chapter we propose a new method for pediatric MRI and taking this variability into account.

5.1.2 Outline

In order to overcome the problems of the existing methods, we propose a semi-automatic approach for the segmentation of the pelvic bones in pediatric MRI. In particular, we propose a multi-template based approach, in which the different templates are representative of the different growing phases of the bone structures. The problem of variability in terms of connectivity is then solved by the choice of the closest bone template, and the shape variability is managed by a landmark-based user registration. A semi-automatic approach (user interaction for the landmark selection and then automatic processing) was preferred to a fully automatic one, giving to the user a better control on the final segmentation result and avoiding potential unexpected results in case of strong abnormalities of the patient anatomy.

To the best of our knowledge, this is the first study specifically addressing the segmentation of pelvic bones in pediatric MRI, whatever the patient's age.

5.2 Segmentation method: a template-based approach

Due to the complexity of the bones in the pelvic regions and their high variability during growth, we propose a multi-template based approach. The idea is to build a set of 3D bone templates at different ages, and to segment images of a patient by using the template corresponding to the closest age. The segmentation is performed in two steps. First, a semi-automatic pre-segmentation is based on

the registration of the chosen anatomical bones template to the target MRI. In the second step, the pre-segmentation is refined through the evolution of deformable models, in order to extract the final segmentation.

5.2.1 Generation of anatomical templates

In order to cope with the high variability in terms of connectivity of the children bones structure during their growth, we propose to build bones templates from pelvic CT exams of a few patients of different ages and sex. Although MRI is often the preferred modality for children, CT data are available for enough cases, and allow for an easy, accurate and fast segmentation of the bones. Note that this was done only for a few cases at different ages based on existing data from abdomino-pelvic CT performed for extrapelvic and extraosseous pathologies, and no specific CT acquisition was done for this study. To segment the CT volumes, we use the semi-automatic region competition method by Zhu and Yuille [141] implemented in ITK-Snap software [137]. Potential errors on the segmentation results are manually corrected.

Using this method, five anatomical templates (corresponding to 1, 2, 4, 9 and 15 years old children) were generated for each sex group, yielding a total of 10 templates. The different ages of the patients were chosen after analyzing a large dataset of CT scans, to extract the age ranges corresponding to the most significant anatomical changes during the ossification process and growth. Some 3D views of some anatomical templates are shown in Figure 5.1. The variation in terms of connectivity of the pelvic bones during the growth can be observed by the gradual fusion of the three structures of the hip bone (ilium, ischium and pubis).

5.2.2 Pre-segmentation from closest template registration

The pre-segmentation of the MRI volumes is obtained through thin-plate spline (TPS) registration [10, 99] between the chosen anatomical template and the target MRI volume. For each target MRI, in order to have a good representation of the bone connectivity, the template with the corresponding sex and the closest age was chosen.

The TPS-based registration method [10, 99] formalizes the deformation of an image M , considered as a grid structure, as an interpolation problem. Given two sets of points P_s and P_t in the grid, the optimal non-linear transformation T is obtained by ensuring the point-wise correspondence between the two sets [89]. The propagation of the deformation to the rest of the image grid is defined by the thin-plate interpolation model, that minimizes the bending energy [56]. An example of the deformation produced by the TPS interpolation on a 2D grid is shown in Figure 5.2.

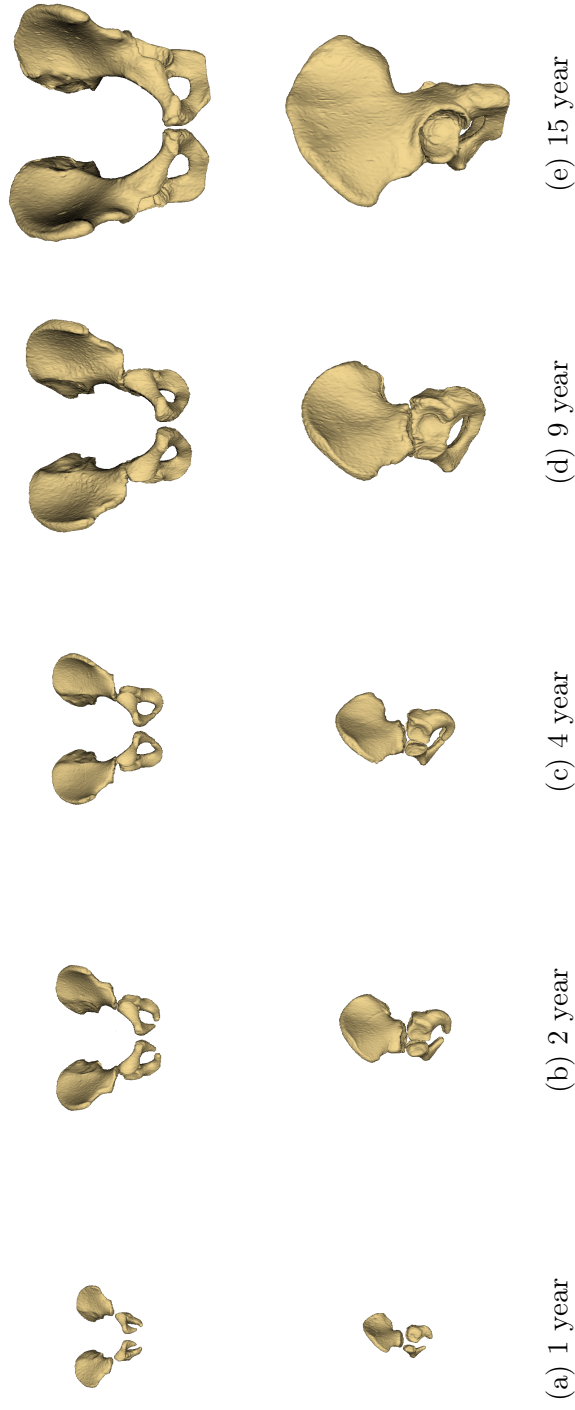


Figure 5.1: Coronal and sagittal views of the 3D bones templates, generated from male patients of different ages. In addition to the different scale of the models, it is possible to appreciate the gradual fusion of the three structures of the hip bone (ilium, ischium and pubis).

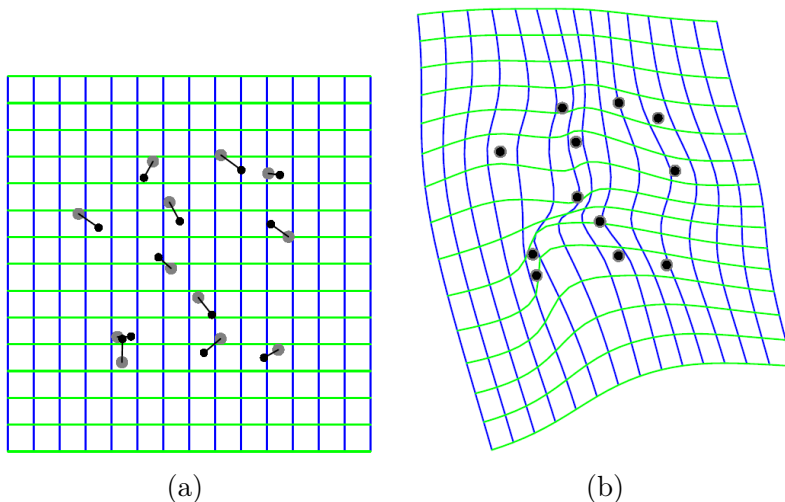


Figure 5.2: Example of thin plate spline registration on a 2D grid. a) Original grid. b) Transformed grid after applying the transformation. The small black points mark the positions of the source landmarks, the big gray points mark the target landmarks (drawn after image from [110]).

In our application the image M is the template image, the set P_s represents manually selected landmarks on the template image and the set P_t represents the anatomically corresponding landmarks manually selected on the target MRI image I . The pre-segmentation of the bones is then the image $M_t = T(M)$ resulting from the registration.

5.2.3 Refined segmentation using deformable models

The final segmentation of the bone structures relies on a parametric deformable model, initialized by the pre-segmentation M_t . An original feature of the proposed approach is that the landmarks used for the registration also constrain the evolution of the surface. We use the following notations: I is the MRI volume, surfaces are parametrized by (s, r) , $v(s, r)$ denotes a point of the evolving surface, and $v_0(s, r)$ the corresponding point on the initial surface given by M_t .

Deformable model

Given a parametric surface $v(s, r) = [x(s, r), y(s, r), z(s, r)]$, the evolution of the deformable model can be formulated starting from a force balance equation

$$F_{int}(s, r) + \gamma F_{ext}(s, r) = 0, \quad (5.1)$$

where $F_{int}(s, r) = \alpha F_{el}(s, r) + \beta F_{rig}(s, r)$, $F_{el}(s, r)$ and $F_{rig}(s, r)$ are the membrane and the thin-plate forces, respectively [130]:

$$F_{el}(s, r) = \frac{\partial v(s, r)}{\partial s} + \frac{\partial v(s, r)}{\partial r}, \quad (5.2)$$

$$F_{rig}(s, r) = \frac{\partial^2 v(s, r)}{\partial s^2} + 2 \frac{\partial^2 v(s, r)}{\partial s \partial r} + \frac{\partial^2 v(s, r)}{\partial r^2} \quad (5.3)$$

We propose to make the parameters α and β locally dependent on the curvature of the initial model $v_0(s, r) = v(s, r) |_{t=0}$, and then to keep these values during the model evolution:

$$\alpha(s, r) = \frac{\kappa_\alpha}{\sqrt{\left(\frac{\partial v_0(s, r)}{\partial s}\right)^2 + \left(\frac{\partial v_0(s, r)}{\partial r}\right)^2}} \quad (5.4)$$

$$\beta(s, r) = \frac{\kappa_\beta}{\sqrt{\left(\frac{\partial^2 v_0(s, r)}{\partial s^2}\right)^2 + 2 \left(\frac{\partial^2 v_0(s, r)}{\partial s \partial r}\right)^2 + \left(\frac{\partial^2 v_0(s, r)}{\partial r^2}\right)^2}} \quad (5.5)$$

where κ_α and κ_β are two constant parameters. These formulations of the parameters α and β allow us to maintain the shape of $v(s, r)$ consistent with the shape of $v_0(s, r)$, during its evolution. Since bones contain both regions with strong and low curvature, this characteristic is taken into account in the proposed method, which would not be possible with constant parameters. This approach assumes that, having an initialization close enough to the desired final configuration, the points of the evolving surface $v(s, r)$ will converge to final points that anatomically correspond to the ones of the initialization $v_0(s, r)$. This hypothesis is satisfied thanks to the first template registration step, that provides a good initialization. This allows defining α and β from the curvature on the initial surface v_0 .

The external force F_{ext} is chosen classically as the GVF force field [129], but computed from a filtered image volume I_{op} , resulting from a morphological opening of the image I (using a sphere of radius $r = 2$ mm as structuring element). This allows attenuating the image gradients generated by the small components of adipose tissues close to the target bones regions.

Constraints on the surface evolution

In order to manage the TPS registration (see Section 5.2.2), the most efficient approach for the selection of the landmarks P_s and P_t is to select them on the external borders of the bones structures, as shown in the example in Figure 5.3, at anatomical positions that are easy to identify. Therefore it is possible to assume that the points P_t , being part of the initialization $v_0(s, r)$, are already at the correct spatial positions for the final segmentation, and thus have to be considered as fixed

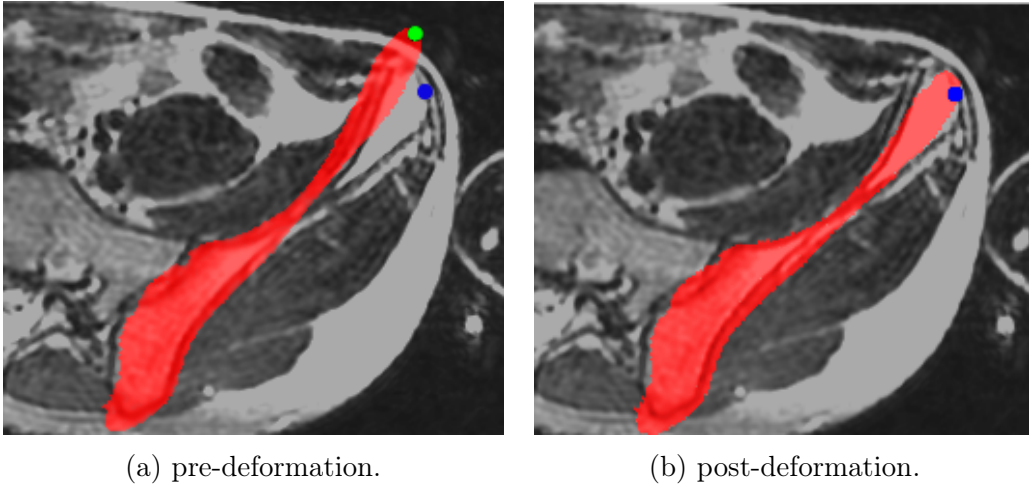


Figure 5.3: Example of a couple of landmark points and the resulting deformation on a MRI slice portion. The red region represents the current bone template mask. The landmarks are represented by green (P_s) and blue (P_t) points in the images.

points during the evolution of $v(s, r)$. Moreover, in order to cope with situations where a point of P_t (manually selected landmark) could potentially not be exactly in correspondence with a point of the surface $v_0(s, r)$, the fixed points are chosen as the closest points of $v_0(s, r)$ to the points P_t .

5.3 Results

The proposed method was tested on 25 T2-weighted volumic MRI images, acquired in the coronal plane, of patients between 1 and 18 years old (see Chapter 2).

5.3.1 Landmark selection

In our experiments, the selection of the landmarks was done in an iterative approach in which, for each new landmark selected, the user was able to visualize the deformed template resulting from all the landmarks previously selected. In this way the user, having no prior constraint on the number of landmarks and a clear visualization of the deformation effects, was able to fully control the registration procedure in order to achieve the desired result. Moreover, the user was able to select and to verify the position of the landmarks in the three different anatomical views (axial, coronal and sagittal). This procedure (see Section 8.2 for details about the GUI) was shown to be very efficient, and the feedback from the users was very positive. On the tested cases, an average of 20 landmarks, selected

as anatomically relevant points, were needed in order to manage the thin-plate registration and to obtain a good initialization for the next step.

The interaction time needed for the registration step was variable in function of the experience of the user: from around 5 min for an expert user to a maximum of 30 min for a new user (less than 5 full registration experiences), and this time decreases rapidly with more experience.

5.3.2 Qualitative evaluation of the segmentation results

Two examples of the complete segmentation pipeline on a 1 year old patient and on a 16 years old patient are shown in Figure 5.4 and in Figure 5.5, respectively. We can see from the results that the first thin-plate registration efficiently allows us to obtain a deformed template, which maintains the connectivity features of the original template. Moreover, thanks to the meaningful spatial positions of the user-selected landmarks, the final model does not contain unexpected spatial distortions. Such a registration allows us to obtain a pre-segmentation which is already close to the target bones on the MRI volumes. Finally, the proposed deformable model allows us to refine these results, obtaining a final segmentation which was positively appreciated by medical experts. Other qualitative results are shown in Figures 5.6-5.8.

5.3.3 Quantitative evaluation of the segmentation results

The performances of the proposed approach were validated through comparison with manual segmentations performed by medical experts and with results provided by other tested methods (standard deformable models).

More precisely, the following comparisons, in terms of DC and ASSD (see Section 2.3), have been performed:

- *Pre-segmentation vs Manual*: we estimated the DC and the ASSD between the pre-segmentation results, obtained through registration of the bones templates (see Section 5.2.2), and the manual segmentations.
- *Snake vs Manual*: we estimated the DC and the ASSD between the segmentation obtained with a standard parametric active contour (spatially constant α and β parameters), using the pre-segmentation as initialization, and the manual segmentations.
- *Snake_local vs Manual*: we estimated the DC and the ASSD between the segmentation obtained with a parametric active contour using the proposed locally dependent α and β parameters (see Equations 5.4 and 5.5), using the pre-segmentation as initialization, and the manual segmentations.

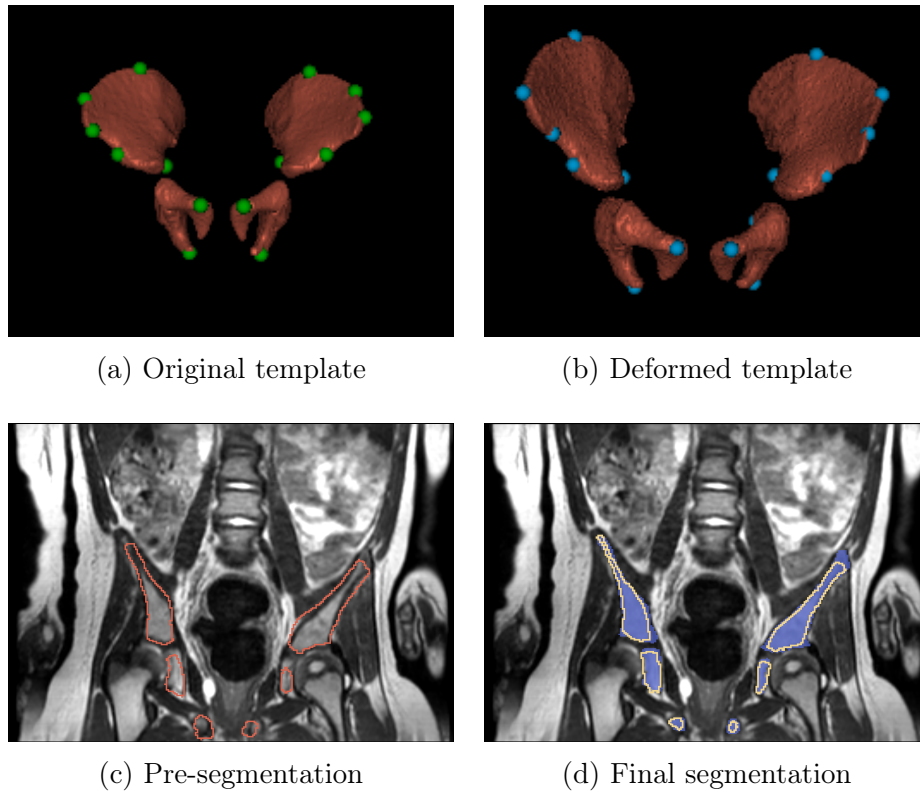


Figure 5.4: Example of segmentation results on a 1 year old patient. (a) Original template and source landmarks (green spheres). (b) Deformed template and target landmarks (blue spheres). (c) MRI slice with pre-segmentation (red contour). (d) MRI slice with final segmentation (yellow contour) and manual segmentation (blue mask).

- *Snake_land vs Manual*: we estimated the DC and the ASSD between the segmentation obtained with a standard parametric active contour, using the pre-segmentation as initialization and the user-selected landmarks as fixed points during the surface evolution, and the manual segmentations.
- *Snake_land_local vs Manual*: we estimated the DC and the ASSD between the complete proposed method, using the pre-segmentation as initialization, the user-selected landmarks as fixed points during the surface evolution and locally dependent parameters, and the manual segmentations.

The parameters for the evolution of the deformable model were experimentally set to: $\kappa_\alpha = 0.018$; $\kappa_\beta = 0.01$; $\gamma = 3$. For the tests *Snake vs Manual* and *Snake_land vs Manual* the constant α and β parameters were set, for each patient, as the mean values of $\alpha(s, r)$ and $\beta(s, r)$ along the initialization surface. The same

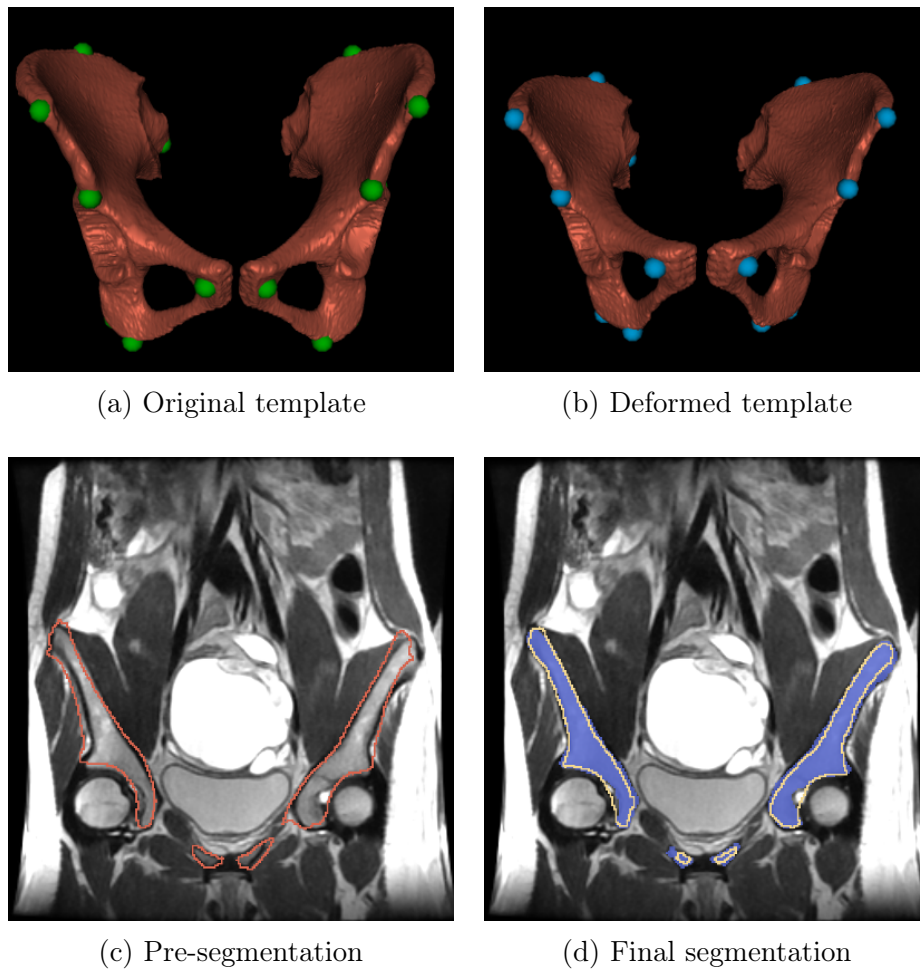


Figure 5.5: Example of segmentation results on a 16 year old patient. (a) Original template and source landmarks (green spheres). (b) Deformed template and target landmarks (blue spheres). (c) MRI slice with pre-segmentation (red contour). (d) MRI slice with final segmentation (yellow contour) and manual segmentation (blue mask).

parameters were used for the full MRI dataset. Finally, in order to evaluate the inter-user variability of the manual segmentation results, the DC and the ASSD were also evaluated between the manual segmentations performed by two different users.

The results in Figure 5.9 show that the user-guided template registration already provides a good initialization for the following segmentation. However, using a standard snake formulation does not significantly improve the results. More relevant improvements were obtained using either the local parameters or the evo-

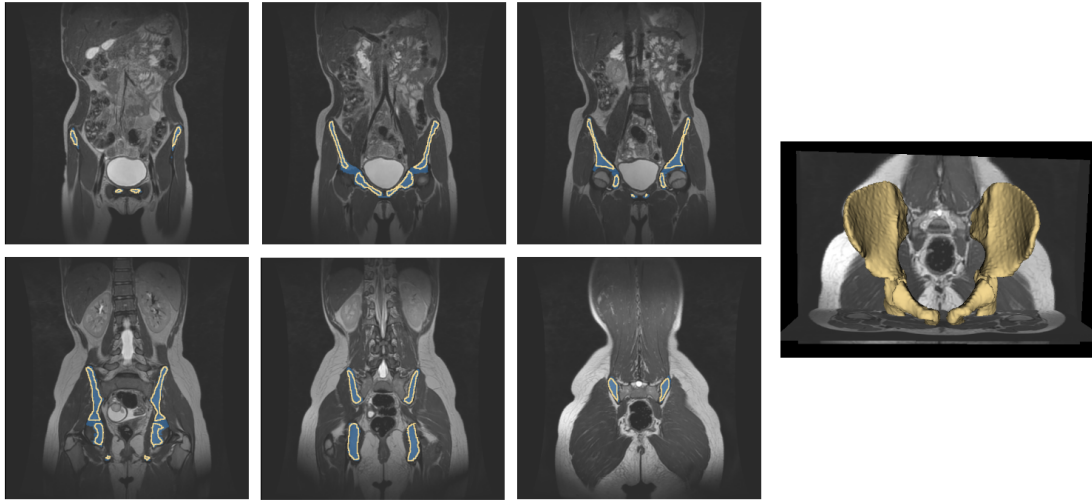


Figure 5.6: Qualitative segmentation results on a 9 years old patient. Six coronal views (left) and the 3D view (right) are displayed. The yellow contours represent the segmentation obtained using the proposed method. The blue masks represent the manual segmentation.

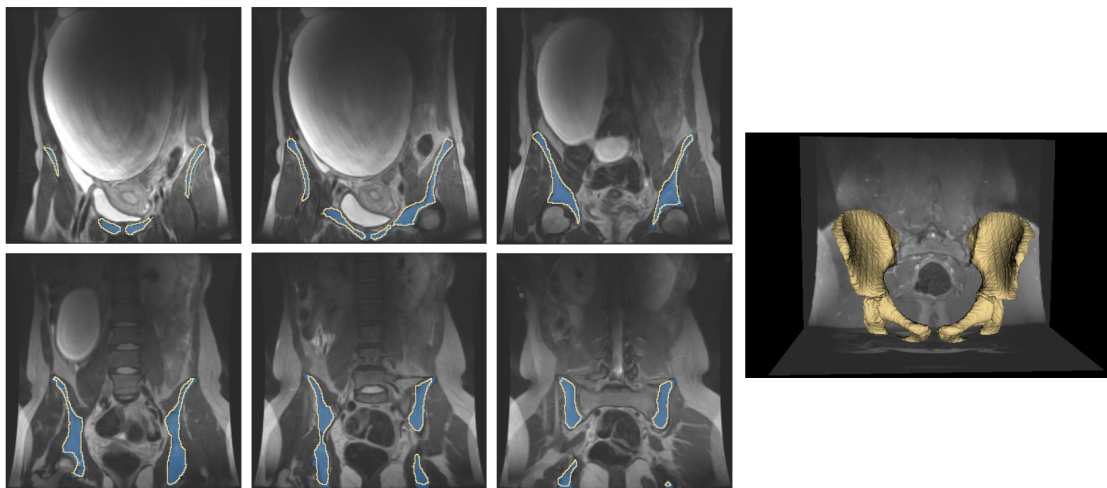


Figure 5.7: Qualitative segmentation results on a 15 years old patient. Six coronal views (left) and the 3D view (right) are displayed. The yellow contours represent the segmentation obtained using the proposed method. The blue masks represent the manual segmentation.

lution constraints given by the fixed landmarks, with no significant differences between the two approaches. The best results are obtained by combining these two contributions (green boxplots in Figure 5.9).

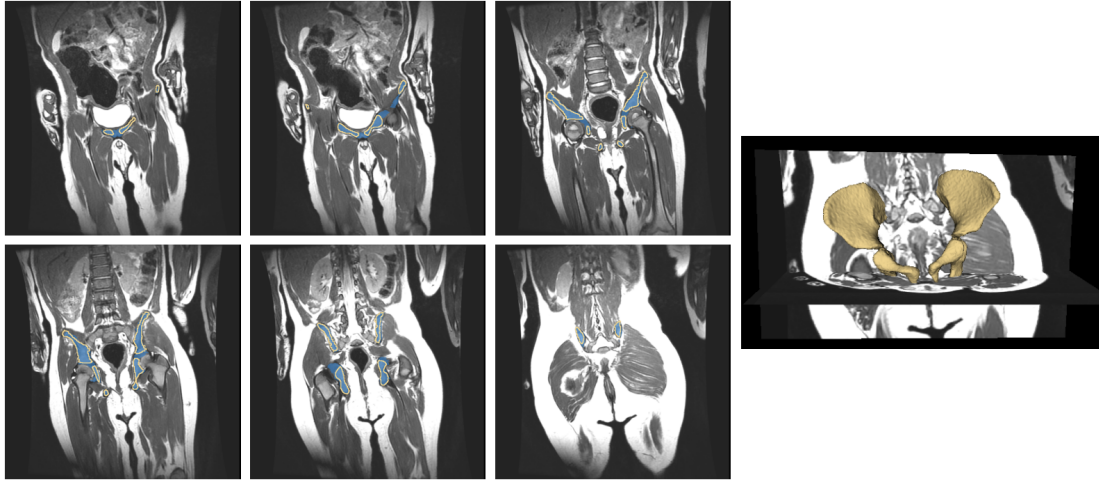
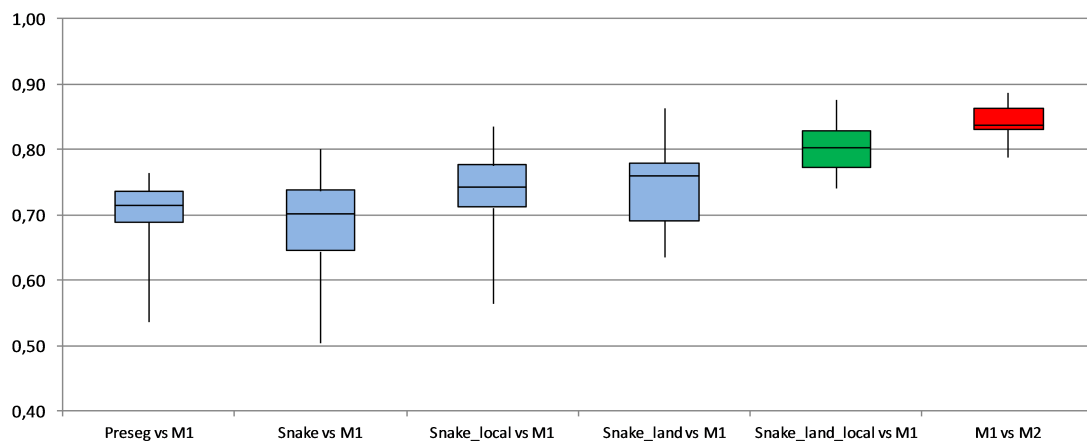


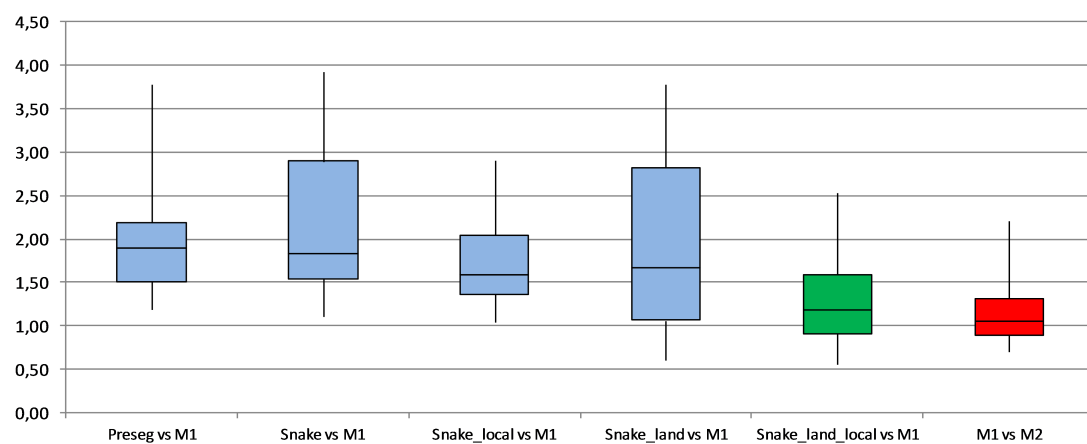
Figure 5.8: Qualitative segmentation results on a 2 years old patient. Six coronal views (left) and the 3D view (right) are displayed. The yellow contours represent the segmentation obtained using the proposed method. The blue masks represent the manual segmentation.

As already mentioned, the previous results were obtained using an average number of 20 user-selected landmarks, which was considered a good compromise between the user interaction time and the accuracy of the initialization. In order to analyze the effect on the final segmentation accuracy of the number of user-selected landmarks, 15 images (a subset of the full patients dataset) were segmented using different user-selected landmarks sets containing a different number of points. In particular, the tests were performed using 4 sets of 10, 20, 30 and 40 landmarks, respectively. These results are depicted in Figure 5.10. As expected, the higher the number of the user-selected landmarks, the higher the segmentation accuracy. However, there is not an extremely relevant performance increase using more than 20 landmarks, which is coherent with the user experience of the proposed tool.

In order to have a more consistent evaluation of the performances of the proposed method, we also looked at the relation between the DC of the segmentation results (*Snake_land_local*) and the age of the corresponding patients. As shown in Figure 6.7, there is not, qualitatively, a significant relation between the performances and the patients' age, which is very encouraging for our pediatric application. However, it is important to remark that our dataset (25 patients) is not large enough to test any statistical assumptions on the correlation between DC and patients' age.



(a) Dice.



(b) ASSD [mm].

Figure 5.9: Quantitative evaluation of the segmentation results in terms of Dice index and ASSD. Each boxplot represent the minimum and maximum values, the 1st and the 3rd quartile and the median value. The green boxplots represent the results obtained using the proposed method. Comparisons are done with respect to a first manual segmentation (M1). The red boxplots represent the comparisons between the manual segmentations performed by two different users (M1,M2).

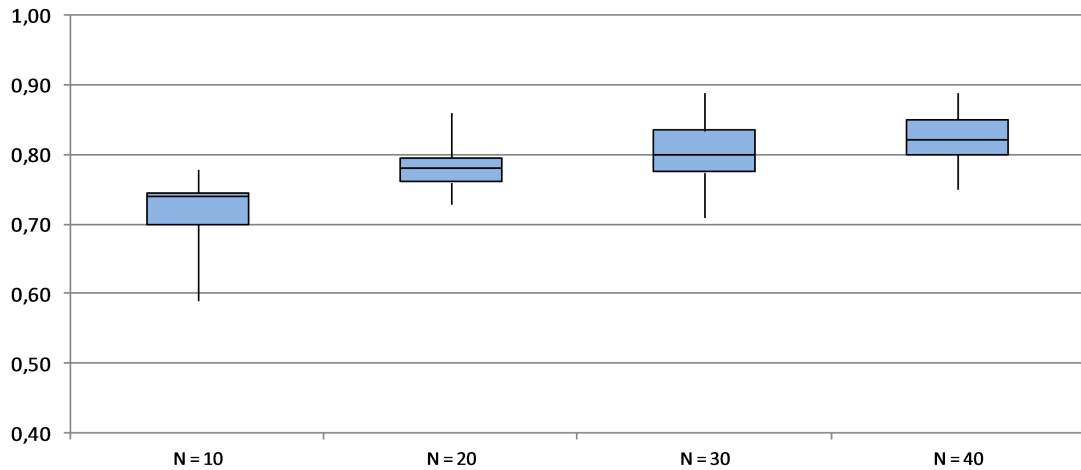


Figure 5.10: Evaluation of the results of the proposed method in terms of DICE index, for different numbers of user-selected landmarks.

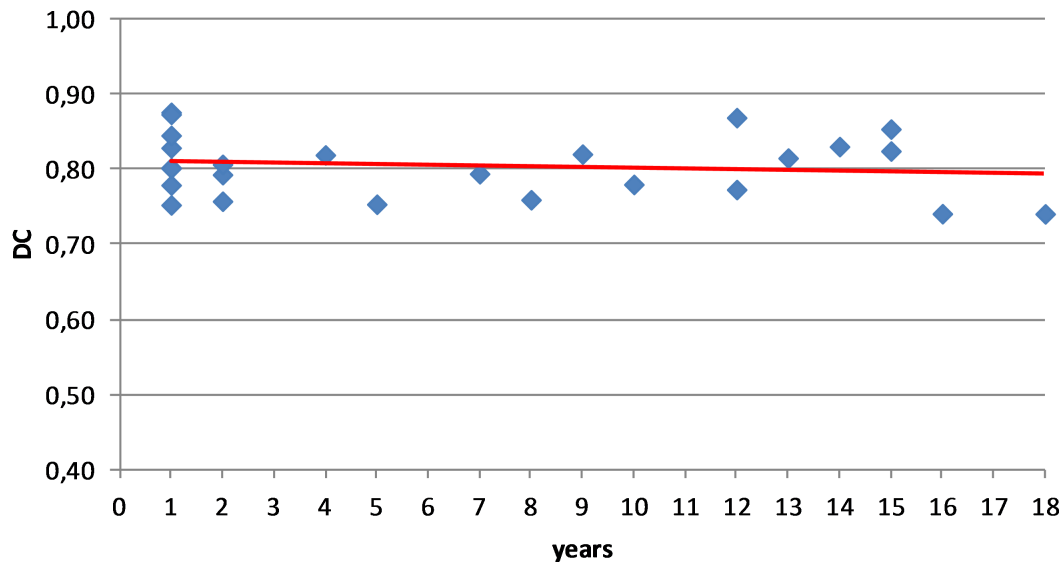


Figure 5.11: Dice score in function of the patients' age and corresponding linear regression line (red).

5.4 Conclusion and discussion

5.4.1 Contributions

In this chapter, we proposed a semi-automatic method for 3D segmentation of pelvic bones in pediatric MRI volumes. The method relies on two original features.

First, a small series of templates is built from CT data, and are used to initialize the segmentation under user’s control. This allows us i) to take into account the variability in terms of connectivity of the children bones structure during their growth and ii) to manage the bones shape variability thanks to the user-interaction. Then a second automatic step refines the segmentation using a deformable model in which regularization parameters depend on the local curvature of the bones. This is relevant since pelvic bones contain both almost flat zones and strong curved ones. Moreover, the user-selected landmarks, needed for the previous registration step, are here used as fixed anchors during the deformable model evolution. Finally, the proposed method was integrated as a plug-in for the software 3D Slicer, delivering a powerful tool and a user-friendly GUI to the clinicians (see Section 8.2 for more details).

The proposed method was evaluated on a varied database of 25 MRI volumes, obtaining an average accuracy in term of DC and ASSD of $DC = 0.80 \pm 0.04$ and $ASSD = 1.34 \pm 0.55 \text{ mm}$. The qualitative results were also positively evaluated by medical experts, who appreciated the first manual landmark selection, which was not tedious while guaranteeing a good initialization.

5.4.2 Perspectives

As detailed in Section 5.2.2 our method requires a set of user-selected landmarks, in order to manage the thin-plate registration. A potential improvement of the proposed method could be to avoid the user-interaction, automatically detecting meaningful landmarks in the MRI volume [20, 67]. However this approach, while reducing the user interaction time, could lead to unexpected results in case of wrong landmarks detection. This could consequently reduce the reliability of the entire segmentation framework, which is essential in clinical applications.

As discussed in Section 5.2.3, the landmarks for the registration are manually placed in correspondence of the external borders of the bones structure. However, our method does not deal with potential inaccurate landmarks selection. For this reason, a potential improvement to our method could be to automatically refine the landmark position (e.g. based on local image features, such as the intensity gradients).

Finally, a potential extension of this work could also concern the bones template selection, choosing the anatomically closest template instead of the closest age, in order to cope with potential abnormal child development. This would require to define an appropriate similarity measure between a template and an image.

Chapter 6

Pelvic vessels segmentation

Abstract

In this chapter, we propose a patch-based deep learning approach to segment pelvic vessels in 3D MRI images of pediatric patients. For a given T2-weighted MRI volume, a set of 2D axial patches is extracted using a limited number of user-selected landmarks. In order to take into account the volumetric information, successive 2D axial patches are combined together, producing a set of pseudo RGB color images. These RGB images are then used as input for a convolutional neural network (CNN), pre-trained on the ImageNet dataset, which results into both segmentation and vessel labeling as veins or arteries. The performances of the proposed method, validated on a dataset of 35 T2-w MRI volumes of pediatric patients, were quantitatively and qualitatively appreciated by medical experts ($ASSD = 0.89 \pm 0.07\text{mm}$, $DC = 0.79 \pm 0.02$). Moreover, in order to deliver a user-friendly tool to the clinicians, the proposed method was implemented as a plugin for the 3D Slicer platform. A part of this work has been published in [120] and a more complete and extended version has also been published in [121].

Contents

6.1	Introduction	63
6.1.1	Context	63
6.1.2	Outline	63
6.2	Segmentation method: a patch-based deep learning approach	63
6.2.1	Patches extraction	64
	Vascular tree reconstruction	64

Pseudo-RGB patches extraction	66
6.2.2 Deep CNN for patches segmentation	67
6.3 Results	68
6.3.1 Landmark selection	69
6.3.2 Qualitative results	69
6.3.3 Quantitative results	69
6.4 Conclusion and discussion	71
6.4.1 Contributions	71
6.4.2 Perspectives	72

6.1 Introduction

6.1.1 Context

Among all pelvic structures, the vessels are particularly important. Indeed, the preservation of the vascular structures during surgery is essential in order to avoid potential functional damages to the patient’s organs. As detailed in Section 3.3, most of the existing studies are applied to angiography images, which present strong vessels enhancement, and are not easy to extend to MRI images. In this context, deep learning methods, which have shown excellent performances in various medical imaging tasks, could be an interesting field to explore. However, deep learning methods usually require large datasets of manually annotated data, which could be a strong limit to their application, especially in pediatrics. Therefore, a transfer learning approach is proposed in this chapter.

6.1.2 Outline

We propose a patch-based deep learning approach that is, to the best of our knowledge, the first study on pelvic vessels segmentation in pediatric MRI. Starting from a set of user-selected landmarks, a series of patches containing the structures of interest is extracted. In this way, for each patient, the user can focus on the analysis of the vascular structures of surgical interest. Similarly to [131], the patches are generated by stacking the three successive slices (Section 6.2.1), forming pseudo-RGB images. This approach allows us to take into account the 3D information of the image while using a CNN pre-trained on ImageNet in a transfer learning approach (Section 6.2.2). Results are discussed in Section 6.3.

6.2 Segmentation method: a patch-based deep learning approach

The proposed method for the segmentation of the pelvic vessels consists of two main steps: a semi-automatic extraction of a set of axial patches containing the vascular structures of interest, followed by an automatic segmentation procedure based on CNN and transfer learning. The pipeline of the proposed method is depicted in Figure 6.1.

Preprocessing First, histogram equalization of each MRI volume is performed. Then, in order to reduce the noise, an anisotropic diffusion filter [93] is applied, taking into account the tubular structure of the vessels.

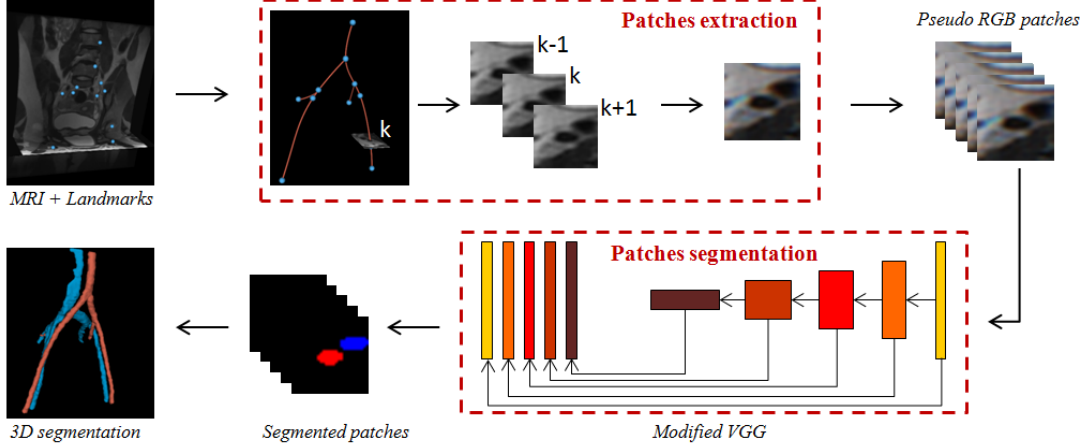


Figure 6.1: Pipeline of the proposed method. A set of 2D pseudo-RGB patches are extracted from the MRI volume and from a set of user-selected landmarks. Patches are then segmented through a modified version [131] of the VGG16 network [107], obtaining the 3D segmentation of the vessels.

6.2.1 Patches extraction

The definition of patches relies on three steps. First, some landmarks along the vessels are provided by the user. The only constraint is that these points should belong to the vessels. In particular, in case of bifurcations, the user can select landmarks on vessel branches in any order. The other two steps, detailed next, consist in reconstructing the vascular tree from the landmarks, and in defining patches centered on the vessels branches in each slice of the image volume.

Vascular tree reconstruction

Let $L = \{\varphi_i = (x_i, y_i, z_i) \in \Omega, i \in \{1 \dots n\}\}$ be the set of user-selected landmarks, where $n = |L|$ is the number of landmarks, $\Omega \subseteq \mathbb{R}^3$ is the image domain, and L is ordered decreasingly in z ($\forall i \in \{1 \dots n - 1\}, z_{i+1} \leq z_i$), hence in the cranio-caudal direction. The vascular tree is reconstructed iteratively by choosing, at each step i , the best candidate landmark $\varphi_c = (x_c, y_c, z_c)$ to be connected with φ_i , minimizing the following objective function, which combines shape and appearance information:

$$f(\varphi_i, \varphi_c) = \alpha \|\varphi_i - \varphi_c\|_2 + \beta \kappa(\varphi_i, \varphi_c, \varphi_{c-1}) + \gamma \sigma_{(\varphi_i, \varphi_c)}^2,$$

where φ_{c-1} is the landmark already connected with φ_c , such that $z_{c-1} > z_c$, κ is the local curvature, estimated as $\frac{1}{r}$ where r is the radius of the circle passing through the three points, σ^2 is the variance of the image intensity in a cylinder whose axis

is the line joining φ_i and φ_c and whose circular basis has a fixed radius r_c , and α, β, γ are constant weight values. Minimizing f means that the path should be formed by points as close as possible, forming a line as straight as possible, and whose spatial context is homogeneous in terms of intensity.

At each iteration i , the candidates φ_c are chosen as the landmarks that have $z_c > z_i$ and that are already connected to at most one landmark. This candidates selection allows us to take into account the fact that, in the pelvis, the different vessels branches are descending along the cranio-caudal direction. Furthermore, we can also automatically handle bifurcation points while avoiding anatomically incoherent connections (i.e. trifurcations). This procedure, repeated for each φ_i , results in an approximate reconstruction of the vascular tree, as shown in Figure 6.2. Further details on the proposed algorithm are given in Algorithm 1. The parameters for the reconstruction are experimentally set to $\alpha = 1$, $\beta = 200$, $\gamma = 10^3$, $r_c = 1 \text{ mm}$, producing a correct vascular tree reconstruction for all the patients present in the dataset.

```

input :  $L = \{\varphi_i = (x_i, y_i, z_i) \in \Omega, i \in \{1..n\}\}$ 
output:  $LC = \{\varphi_{conn_i} = (x_{conn_i}, y_{conn_i}, z_{conn_i}) \in \Omega, i \in \{1..n\}\}$ 

for  $i \leftarrow 1$  to  $n$  do
  if  $i=1$  then
     $\varphi_{conn_i} \leftarrow \{\}$ ;
  else
     $C_i \leftarrow L\{\varphi_c \mid z_c > z_i, N_{\varphi_c} < 2\}$ ;
     $v_i \leftarrow \{\}$ ;
     $k \leftarrow 0$ ;
    for  $k \leftarrow 1$  to  $|C_i|$  do
       $\varphi_c \leftarrow C_i[k]$ ;
       $v_i[k] \leftarrow f(\varphi_i, \varphi_c)$ ;
    end
     $\varphi_{conn_i} \leftarrow C_i[p] \mid v_i[p] = \min(v_i)$ ;
     $N_\varphi \leftarrow N_\varphi + 1 \mid \varphi \in L, \varphi \equiv \varphi_{conn_i}$ 
  end
end

```

Algorithm 1: Pseudo-code of the vascular tree reconstruction algorithm. Notations: φ represents a generic point in the image domain Ω , L represents the set of user-selected landmarks, ordered decreasingly in z , LC represents the set of upper connections ($z_{conn_i} > z_i$) of each element of L , C_i represents the set of candidate points for connection with the point φ_i , N_φ represents the number of upper connections of the point φ . Here, for any set A , $A[x]$ denotes the x^{th} element of A .

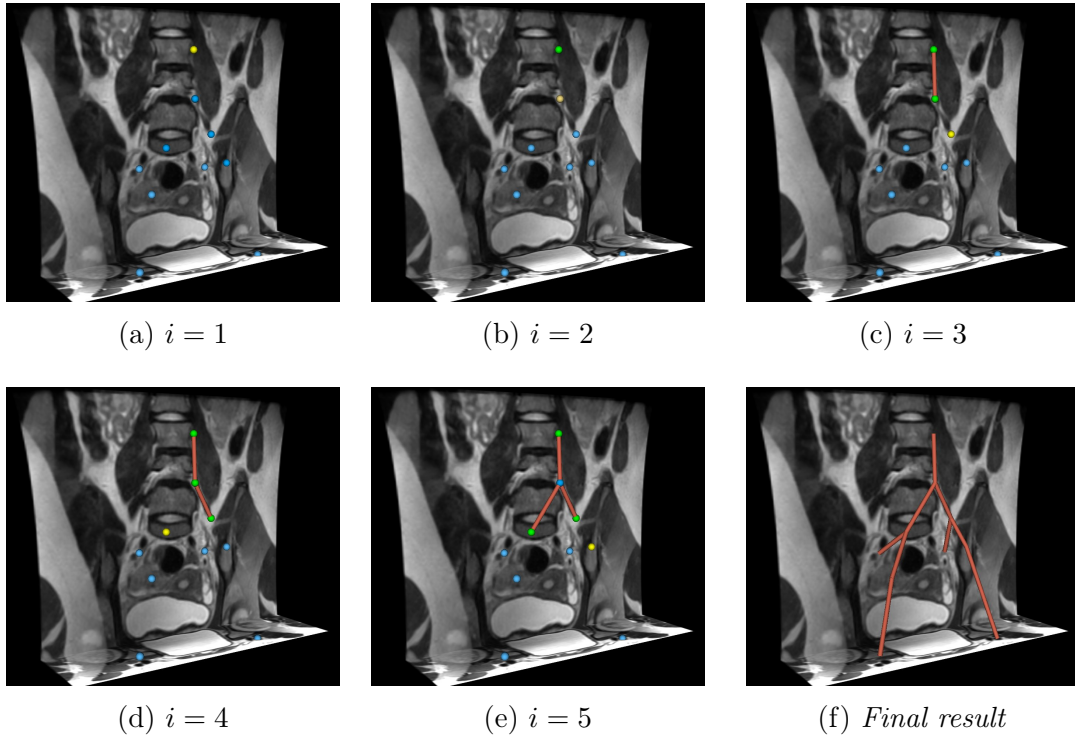


Figure 6.2: Example of reconstruction of the vascular tree (first five steps). In each image each blue sphere is a generic landmark, the yellow sphere is the landmark φ_i analyzed at step i and the green spheres are the candidate landmarks for connection φ_c . The vessel paths are represented in red.

Pseudo-RGB patches extraction

Once the vascular tree is obtained, each vessel branch is approximated by a spline. For every slice k , we first define p_k as the point where the spline intersects slice k . Then we extract a square patch ($N \times N$ pixels) centered at p_k . Every triple of successive patches ($k-1$, k and $k+1$) is interpreted as a pseudo-RGB patch, where each color channel is fed with a gray-level patch as illustrated in Figure 6.3, that incorporates the 3D information of successive patches. This procedure produces a set of pseudo-RGB patches, containing the vascular structures, that will be used as input for the segmentation method that follows. The patches dimensions were set to 31×31 pixels. Given the resolution of the images (average voxel size $0.92 \times 0.92 \times 0.74 \text{ mm}^3$) and the thickness of the vessels, the patches largely include the sections of the vessels.

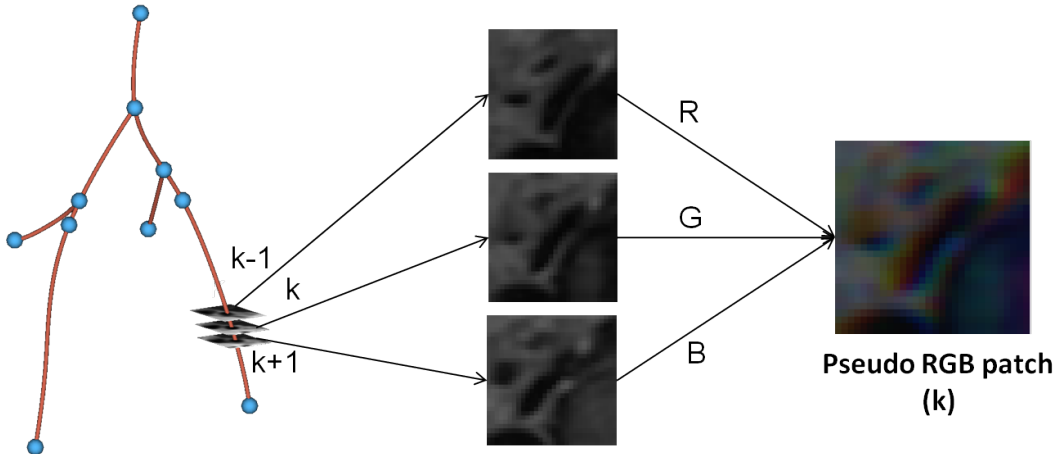


Figure 6.3: Pseudo RGB patches extraction for a given slice k .

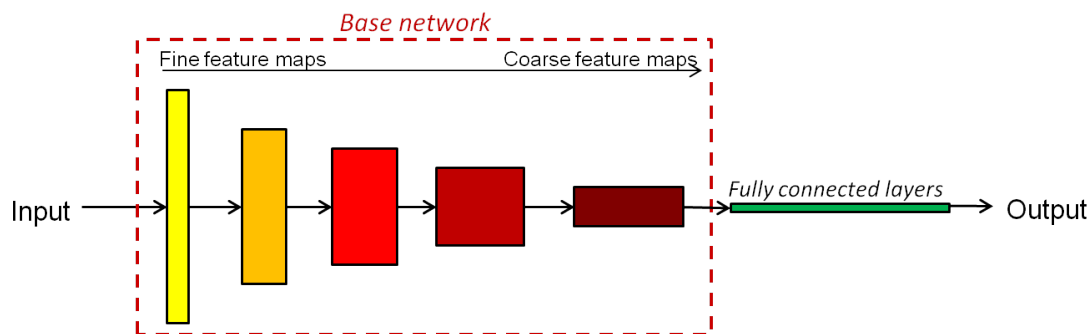
6.2.2 Deep CNN for patches segmentation

In this section, we propose to use CNN to segment the patches into vessel and non-vessel regions, and jointly classify the vessel regions into veins or arteries. To this aim, a modified version of the VGG-16 network [107], pre-trained on the ImageNet dataset [27] is employed.

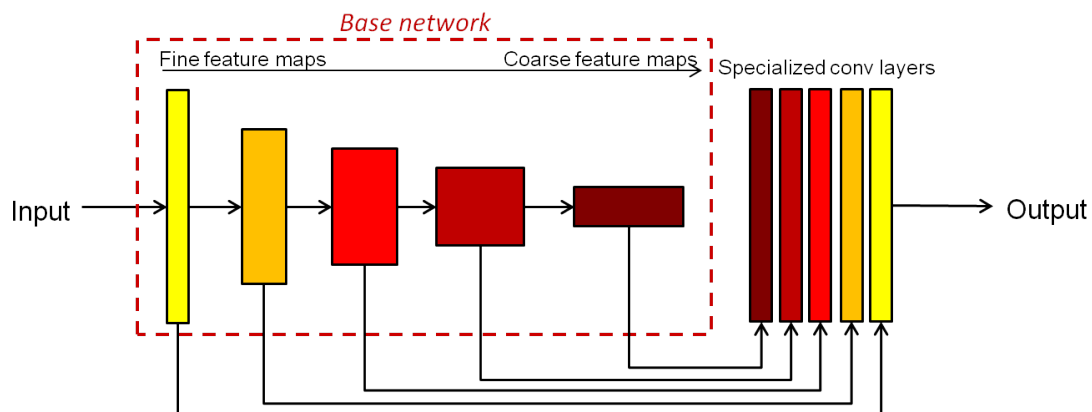
The network is built by removing the final fully connected layers of the pre-trained VGG-16 network, while preserving the 5 convolutional stages which constitute the *base network*. Each of these stages consists of Convolutional layers and Rectified Linear Unit layers. Each convolutional stage is connected with the following one by a Max Pooling layer. Starting from this *base network*, a modified network is then added, similarly to [77, 131], where a specialized convolutional layer (3×3 kernel size) with 16 features maps is inserted after the last convolutional layer of each stage. These specialized layers are resized to the original image size and concatenated together. Finally, the feature maps in the concatenated layers are linearly combined through a final convolutional layer (1×1 kernel), in order to produce the output segmented image. A graphical representation of the network architecture is depicted in Figure 6.4.

As previously mentioned, the layers of the *base network* are already pre-trained on the large ImageNet dataset of natural RGB images. For our application, the entire network is then fine-tuned with a training set of manually segmented patches. Each annotated patch consists of three labels, corresponding to vein, artery and background pixels. The network is trained for 115k iterations, with a constant learning rate $lr = 10^{-6}$, using a multinomial logistic loss function. The loss function is minimized using a stochastic gradient descent with momentum $m = 0.95$.

The analyzed patches, obtained as described in Section 6.2.1 and segmented using the CNN previously described, are then restored to their original position in the image domain $\Omega \in \mathbb{R}^3$, thus providing a classification into veins, artery and background of the whole image volume.



(a) Architecture of the VGG16 network.



(b) Architecture of the modified version of the VGG16 network.

Figure 6.4: CNN used in the proposed method. In our application the inputs and the outputs are, respectively, the pseudo-RBG patches and the corresponding segmentation result (each pixel is labeled as artery, vein, or background).

6.3 Results

The image dataset used in this study is composed of 35 T2-weighted MRI volumes, of patients between 1 and 18 years old. Images have different sizes and resolutions (average voxel size $0.92 \times 0.92 \times 0.74 \text{ mm}^3$).

All pelvic vessels of interest were manually segmented by medical experts and

labeled as veins or arteries. In particular, the following structures were segmented: the abdominal aorta, the inferior vena cava, the iliac arteries and the iliac veins.

6.3.1 Landmark selection

On the tested cases, 12 landmarks were needed, in average, for the vessels paths reconstruction (see Section 6.2.1), which required an interaction time of few minutes for each patient. The only guideline for the user was to select the landmarks inside the vessels lumen, which is easier to achieve by navigating through the axial views. This type of interaction was found reasonable by medical experts, and was considered as a good guarantee to obtain good results from the subsequent automatic steps.

6.3.2 Qualitative results

Some qualitative results are shown in Figure 6.5. In order to correctly interpret them, it is important to consider the anatomy of the vascular structures. The veins, due to their non rigid internal musculature, tend to collapse more than the arteries. This behavior usually leads to arteries that have a more circular shape in the axial section than veins. As shown in Figure 6.5a and Figure 6.5b, this feature appears to be effectively incorporated in our method, providing an overall good veins/arteries classification. Furthermore, we also noticed that most of the misclassification cases were locally confined to regions where this "shape feature" was not expressed. An illustrative example is shown in Figure 6.5c, where a vein with a strong circular shape is erroneously labeled as artery by our method. However, as can be seen in the 3D model of Figure 6.5d, the overall classification is very satisfying and was positively evaluated by medical experts.

6.3.3 Quantitative results

The performance of the proposed method was quantitatively evaluated using a 5-fold cross validation, which corresponds to a training and test set of 28 and 7 patients for each fold respectively. The segmentation accuracy was evaluated in terms of ASSD [mm] and DC (see Section 2.3) between the proposed segmentation and the corresponding manual segmentation provided by a medical expert. More precisely, the following comparisons were performed:

- Gray-level (2D) segmentation vs Manual: we estimated the DC and the ASSD between the segmentations obtained using the proposed method, but exploiting gray-level patches, and the manual segmentations. For a given

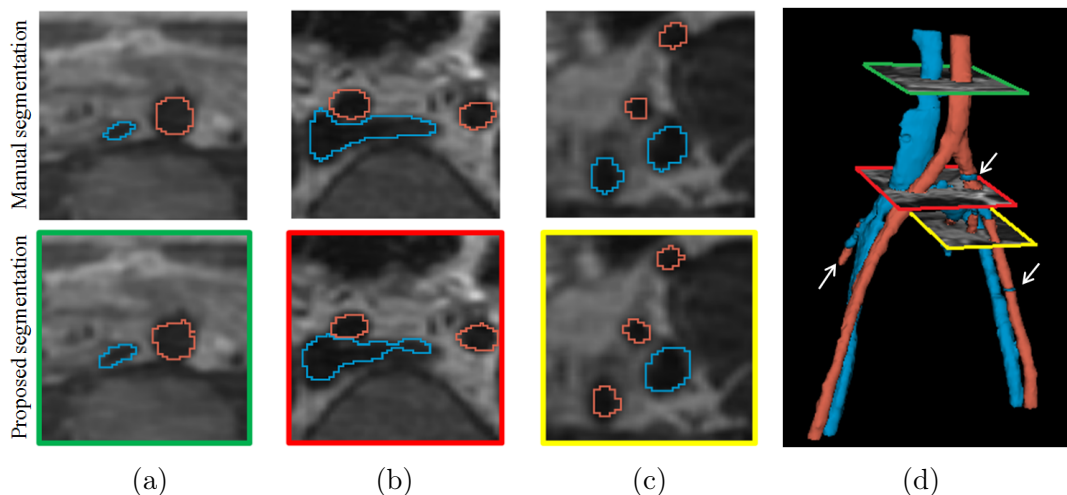


Figure 6.5: Examples of segmentation results. In (a), (b) and (c) the results on some axial sections are depicted. The red contours correspond to the arteries, and the blue ones to the veins. The final 3D model obtained from the segmentation is depicted in (d) with the same color conventions. The three patches in (a), (b) and (c) are shown in (d) with three different colors. Some examples of misclassification are indicated by white arrows.

slice k , a gray-level patch is defined as a pseudo-RGB image, in which each color channel corresponds to the same squared patch in k (see Section 6.2.1).

- Pseudo-RGB (3D-like) segmentation vs Manual: we estimated the DC and the ASSD between the segmentations obtained using the proposed method (pseudo-RGB patches obtained from successive slices) and the manual segmentations.

For each patient, these measures were evaluated for both the global vascular segmentation (fusion of vein and artery) and for veins and arteries separately. The average quantitative results for each fold are reported in Table 6.1. Finally, in order to evaluate the inter-user variability of the manual segmentation results, the DC and the ASSD were also evaluated between the manual segmentations performed by two different users.

The results obtained using the proposed method, also taking into account the images resolution, were considered satisfying by medical experts for surgical planning applications. As expected, results for a single structure (i.e. either artery or vein) were less accurate compared to the overall segmentation. This is mostly due to the additional classification task challenge. Nevertheless, the limited differences between the DC of the three columns in Table 6.1 (3D-like case) indicate

		Arteries		Veins		Arteries&Veins	
		DC	ASSD	DC	ASSD	DC	ASSD
Fold 1	2D	0.74	1.53	0.77	1.20	0.80	0.89
	3D-like	0.77	1.45	0.78	1.04	0.80	0.88
Fold 2	2D	0.69	1.49	0.65	2.50	0.73	1.14
	3D-like	0.71	1.38	0.72	2.21	0.79	0.96
Fold 3	2D	0.72	1.30	0.70	1.70	0.78	0.97
	3D-like	0.74	1.33	0.72	1.42	0.78	0.84
Fold 4	2D	0.65	1.92	0.68	2.26	0.78	1.12
	3D-like	0.74	1.31	0.78	1.46	0.81	0.80
Fold 5	2D	0.68	1.98	0.68	1.49	0.75	0.96
	3D-like	0.71	1.58	0.72	1.30	0.76	0.95
Mean±std	2D	0.69±0.03	1.64±0.29	0.70±0.05	1.83±0.54	0.77±0.03	1.02±0.11
	3D-like	0.73±0.02	1.41±0.11	0.75±0.03	1.49±0.44	0.79±0.02	0.89±0.07

Table 6.1: Quantitative evaluation of the segmentation results obtained with the proposed method (3D-like) and using gray level patches (2D), in terms of DC and ASSD [mm].

overall good classification performances. Moreover, as also shown in Figure 6.6, better results are obtained using pseudo-RGB (3D-like) than using gray-level (2D) patches. In particular, this effect is particularly relevant for the single veins and artery segmentation results, which indicates that the use of the 3D information is particularly important for the vein/artery classification task (more than just for the overall segmentation accuracy).

In order to have a more consistent evaluation of the performances of the proposed method, we also looked at the relation between the DC of the global segmentation (arteries and veins) and the age of the corresponding patients. As it is possible to see in Figure 6.7, the results do not appear to be strongly related with the patients' age, which is encouraging for our pediatric application. However, it is important to remark that our dataset (35 patients) is not large enough to test any statistical assumptions on the correlation between DC and patients' age.

6.4 Conclusion and discussion

6.4.1 Contributions

In this chapter we presented, to the best of our knowledge, the first study on pelvic vessels segmentation of pediatric MRI. We proposed a patch-based deep learning approach using transfer learning.

A main contribution of this work was the design of a semi-automatic method for the patches extraction, based on the structural information of the pelvic vascular

tree. This approach allows the user to focus, for each patient, on the vascular structures of surgical interest, while avoiding potential unexpected results. We also propose to use pseudo-RGB color patches, that incorporate the 3D information of successive slices. The use of these patches makes it possible to exploit a 2D CNN pre-trained on the ImageNet dataset, which allows us to train the network with a small training dataset. This is fundamental for medical applications where the number of annotated images is limited. It is important to remark that the same strategy, based on transfer learning, would have been difficult to employ with 3D CNNs. In fact, even if efficient implementations of 3D CNNs have been released [23, 33, 60, 83], there is a lack of publicly available 3D CNN models pre-trained on large datasets of 3D images [139].

Finally, the proposed method was integrated as a plug-in for the software 3D Slicer, delivering a powerful tool and a user-friendly GUI to the clinicians (see Section 8.2 for more details).

6.4.2 Perspectives

As future work, we plan to post-process our results in order to improve the vein/artery classification. This could be done, for instance, by analyzing the spatial consistency of the classes along the entire 3D model. Moreover, we also plan to investigate other methodologies that take into account the 3D information using more than three successive slices.

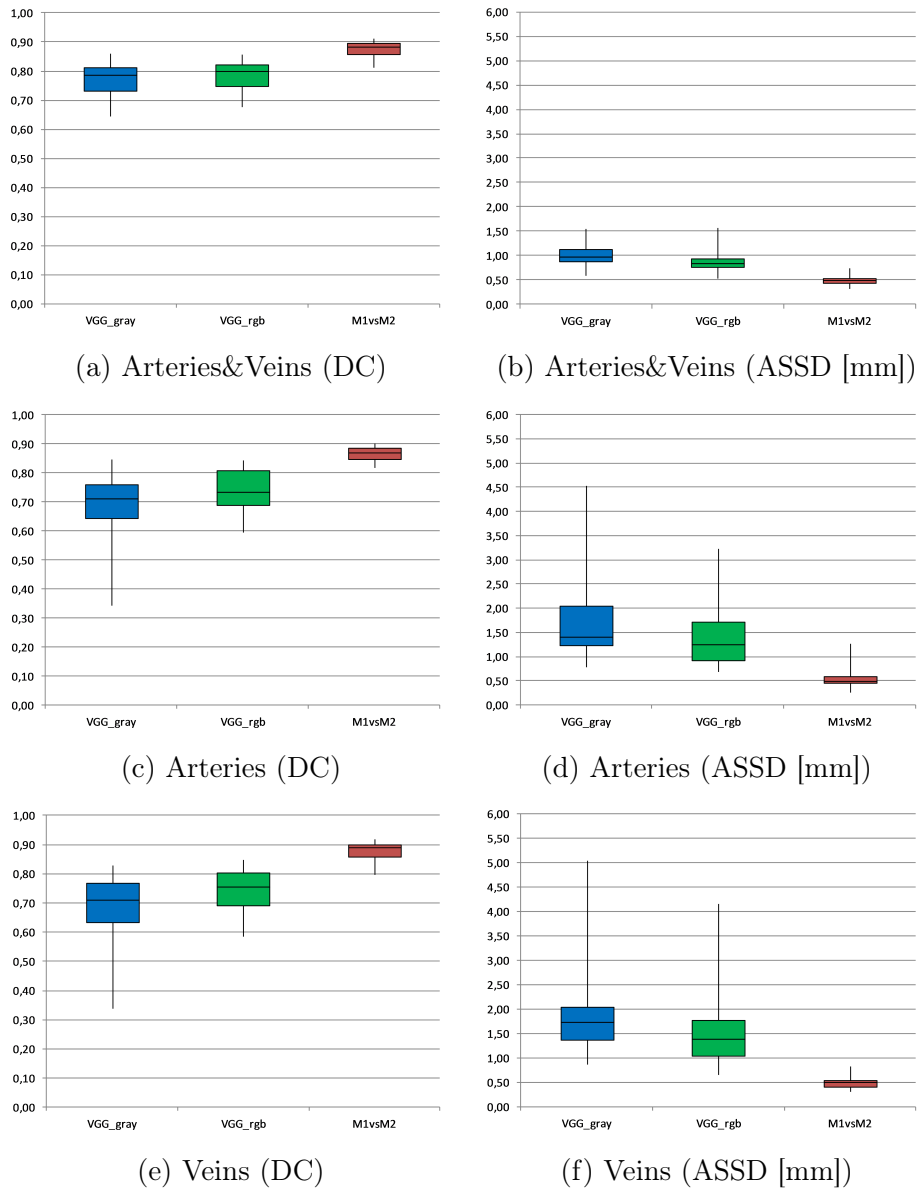


Figure 6.6: Quantitative evaluation of the segmentation results in terms of DC and ASSD. Each boxplot represents the minimum and maximum values, the 1st and the 3rd quartile and the median value. The blue boxplots represent the results obtained using the proposed method on gray-level (2D) patches. The green boxplots represent the results obtained using the proposed method on the pseudo-RGB (3D-like) patches. Comparison are done with respect to a first manual segmentation (M1). The red boxplots represent the comparisons between the manual segmentations performed by two different users (M1,M2).

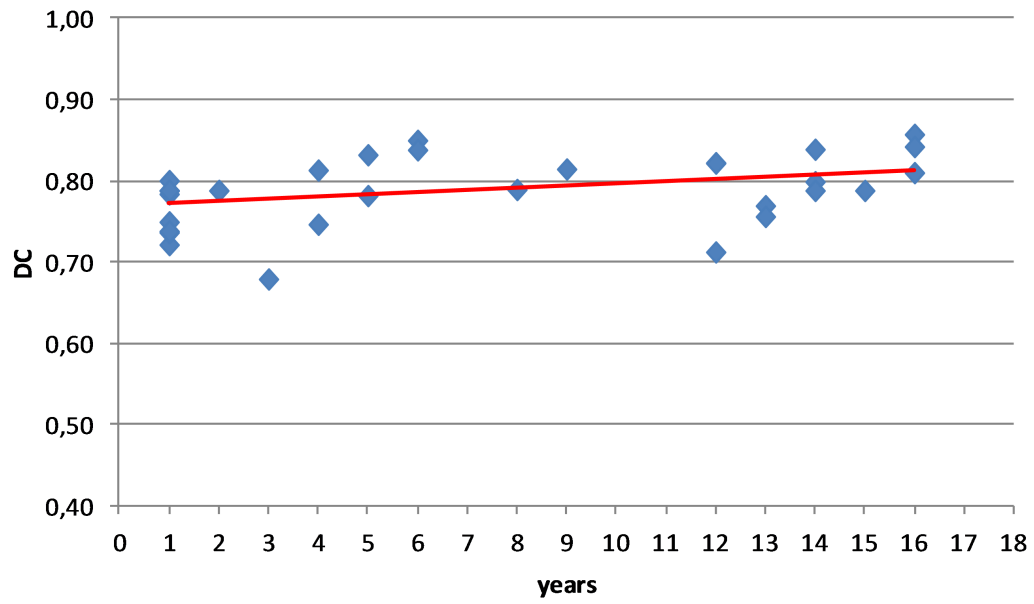


Figure 6.7: Dice score (arteries and veins) in function of the patients' age and corresponding linear regression line (red).

Chapter 7

Bladder segmentation

Abstract

This chapter presents a semi-automatic method for the segmentation of the urinary bladder in T2-weighted MRI images. The proposed method is based on a modified version of the Chan-Vese level-set model, aiming to obtain a robust pre-segmentation inside the bladder region, and on a parametric deformable model for the final segmentation refinement. The performances of the proposed approach, validated on a set of 25 T2-w MRI volumes of pediatric patients, were quantitatively and qualitatively appreciated by medical experts. Moreover, the method was implemented as a plug-in in the 3D Slicer platform, delivering a powerful and user-friendly bladder segmentation tool to the clinicians. This part of the work was done in collaboration with Luca De Masi (former research intern at IMAG2 laboratory, Imagine Institute).

Contents

7.1	Introduction	77
7.1.1	Context	77
7.1.2	Outline	77
7.2	Segmentation method: a deformable model approach	77
7.2.1	Pre-processing	77
7.2.2	Pre-segmentation using level-sets	78
7.2.3	Refined segmentation using parametric deformable models	80
7.3	Results	80
7.3.1	Qualitative results	80

7.3.2	Quantitative results	86
7.4	Conclusion	88
7.4.1	Contributions	88
7.4.2	Limits and perspectives	89

7.1 Introduction

7.1.1 Context

The bladder, due to its central position in the pelvis region, is very important to be integrated in the 3D patient’s model for surgical planning applications. As detailed in Section 3.4, most of the existing methods were developed for CT images. The few promising studies developed for MRI were based on deformable models approaches. However, none of the proposed methods was evaluated on pediatric populations, which generally presents higher intensity inhomogeneities and higher partial volume effects. This chapter addresses these issues.

7.1.2 Outline

The proposed segmentation pipeline includes three main steps: (i) pre-processing of the MRI images, (ii) pre-segmentation, and (iii) a final segmentation refinement. In order to apply the method, the user is required to select one point inside the bladder region. This is the only user interaction in the method and all the subsequent steps are automatic.

7.2 Segmentation method: a deformable model approach

7.2.1 Pre-processing

As first basic step of the processing, starting from one user-selected point inside the bladder region, the T2-w MRI volumes are cropped in order to reduce the amount of data to process in the following steps and the computational time. After obtaining the image ROI, the next step is to prepare the image for the segmentation by improving its quality. In particular, we propose to filter the image with a non-linear bilateral filter [91]. Given a pixel p , with intensity $I(p)$, in the image domain Ω , its filtered value $I^{bf}(p)$ is defined as:

$$I^{bf}(p) = \frac{1}{W^{bf}(p)} \sum_{q \in \Omega} I(q) G_{\sigma_s}(\|p - q\|) G_{\sigma_r}(|I(p) - I(q)|), \quad (7.1)$$

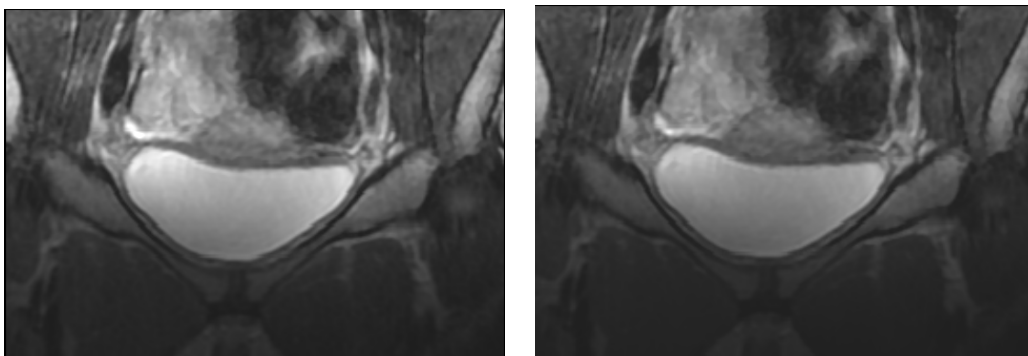
where:

$$G_{\sigma} = \frac{1}{\sqrt{2\pi}\sigma} e^{-\frac{x^2}{2\sigma^2}}, \quad (7.2)$$

$$W^{bf}(p) = \sum_{q \in \Omega} G_{\sigma_s}(\|p - q\|) G_{\sigma_r}(|I(p) - I(q)|) \quad (7.3)$$

The parameter σ_s defines the size of the spatial neighborhood used to filter a pixel, and σ_r controls how much the neighbor pixels are down-weighted because of their intensity difference. The term W_p^{bf} normalizes the sum of the weights.

This filtering was done in order to reduce the noisy components of the image and to increase the intensity homogeneity in the structure of interest, while preserving the edges. An example of the effect of the filter ($\sigma_s = 5$, $\sigma_r = 20$) is shown in Figure 7.1.



(a) Original image

(b) Filtered image

Figure 7.1: Example of bilateral filtering. One coronal slice of the volume is displayed.

7.2.2 Pre-segmentation using level-sets

After the pre-processing, having a bladder that appears more homogeneous (see Figure 7.1), the aim is to obtain a first segmentation using the intensity information of the image, using a level-set formulation. The proposed method is based on the Chan-Vese [18] formulation, but with the addition of an extra energy term:

$$E(C) = \mu \cdot \text{Area}(C) + \lambda_1 \int_{\text{inside}(C)} |I(x, y, z) - c_1|^2 dx dy dz + \lambda_2 \int_{\text{outside}(C)} |I(x, y, z) - c_2|^2 dx dy dz + \boxed{\eta \int_C L(x, y, z) dx dy dz}, \quad (7.4)$$

where C is the 3D surface, I is the filtered image, $\mu, \eta \geq 0$, $\lambda_1, \lambda_2 > 0$ are weights, c_1, c_2 are the mean intensity values inside and outside C and L is a *gradient-enhanced image*, obtained by subtracting the gradient magnitude from the filtered

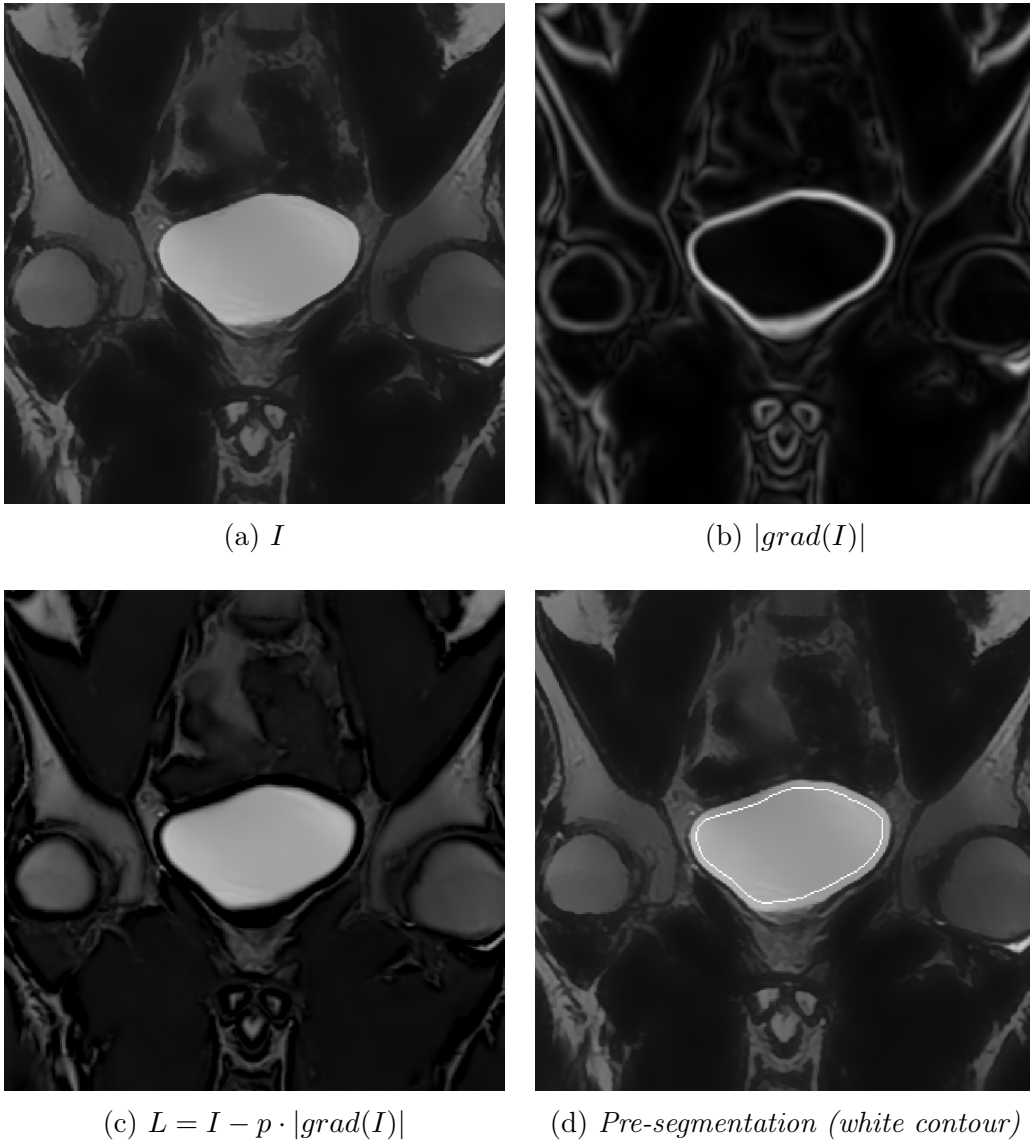


Figure 7.2: Gradient enhancement of the bladder: (a) original image, (b) image gradient magnitude, (c) image L , obtained by subtraction ($p = 8$) of the gradients to the original image, (d) Pre-segmentation result.

image (see Figure 7.2). The level set is initialized as a small sphere ($r = 2$) centered at a user-selected point and the parameters of the energy formulation were experimentally set to: $\mu = 0.1$, $\lambda_1 = 1.2$, $\lambda_2 = 1.2$, $\eta = 5$.

The additional term locally emphasizes the energy contribution of the hyper-intense interior region of the bladder while avoiding potential evolutions of the moving contour in the outside region (e.g due to the contribution of small hyper-

intense regions of adipose tissues surrounding the bladder).

Some examples of the pre-segmentation results are shown in Figure 7.2d and in Figure 7.3b. The segmentation masks are forced to be smaller than the actual bladder due to the effect of the energy term given by L , which indeed guarantees that the pre-segmentation is inside the bladder region. This initial segmentation is then refined, as described next.

7.2.3 Refined segmentation using parametric deformable models

The proposed approach for the final segmentation is based on a 3D deformable model, initialized using the pre-segmentation result and evolving under the effect of edge information resulting from a *Canny filtering* [15]. The Canny filtering produces an edge-map, denoted I_{canny} , of the image I . However, as can be seen in Figure 7.3c, potential intensity discontinuities inside the bladder region may lead to the detection of some extra edges. In order to eliminate the potential edges inside the bladder region, the result of the Canny filtering is refined using the pre-segmentation mask obtained in the previous steps, as shown in Figure 7.3.

Representing the parametric surface as $v(s, r) = [x(s, r), y(s, r), z(s, r)]$, the evolution of the model can be formulated, similarly to Equation 5.1, starting from a force balance equation:

$$F_{int} + F_{ext} = 0, \quad (7.5)$$

$$F_{int} = \alpha F_{el} + \beta F_{rig} + F_{ball}, \quad (7.6)$$

where $F_{ball} = \delta \vec{n}(s, r)$ is the balloon force [24], where $\vec{n}(s, r)$ is the normal to the surface $v(s, r)$ in (s, r) . In our experiments, the weights α , β and δ were set as constants (i.e. independent of (s, r)).

The external force is defined as [70]:

$$F_{ext} = \kappa \nabla (G_\sigma * I_{canny}) \quad (7.7)$$

where G_σ is a Gaussian kernel with standard deviation σ , and κ is a constant weight parameter.

The parameters that guide the evolution of the deformable model were experimentally set to: $\alpha = 1.4$, $\beta = 1.4$, $\delta = 0.6$, $\kappa = 5$ and $\sigma = 1$.

7.3 Results

7.3.1 Qualitative results

Some qualitative examples of the segmentation results are depicted in Figures 7.4-7.6, where it is possible to appreciate the good performance of the proposed method

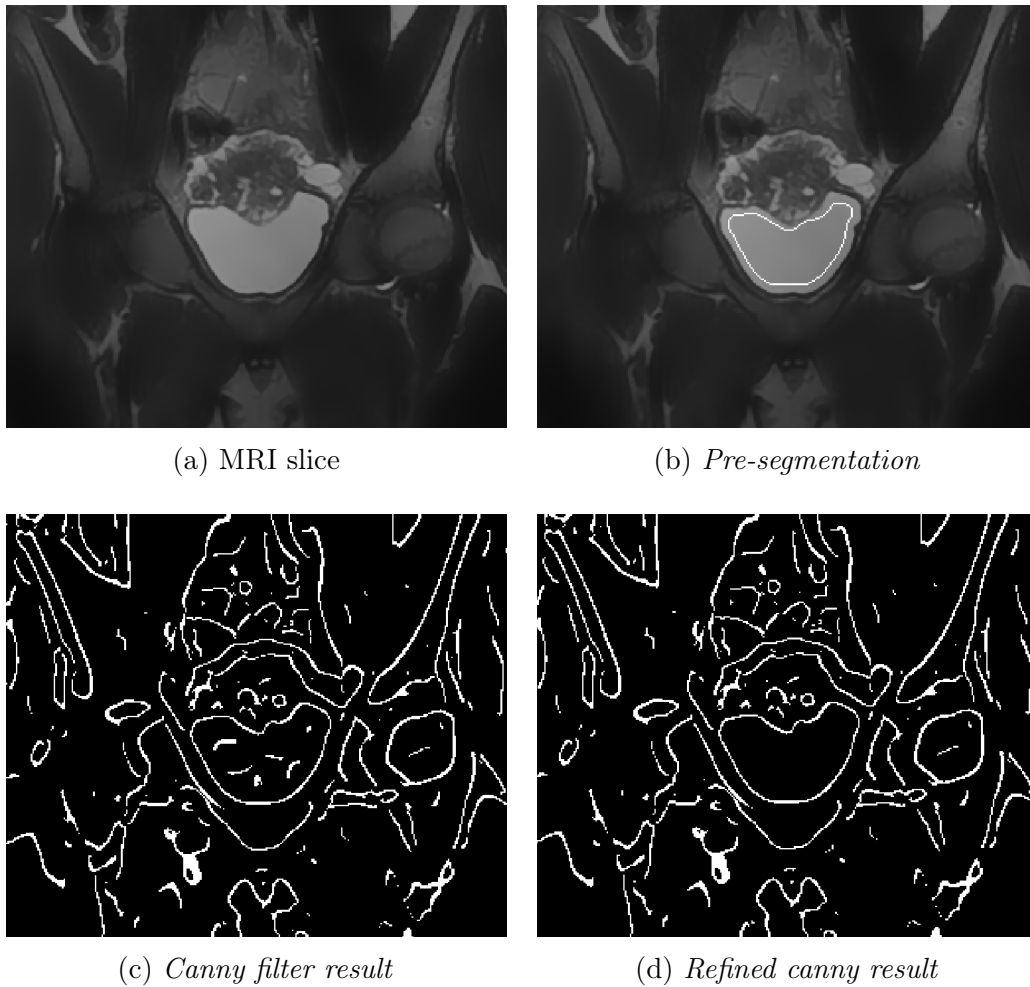
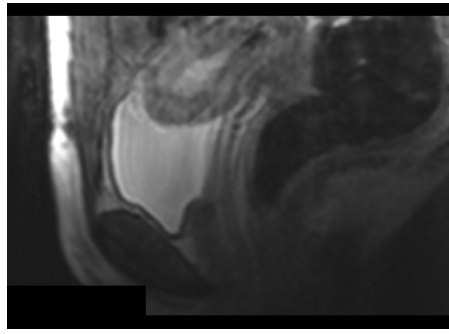
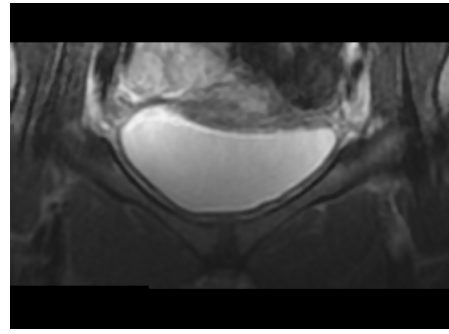


Figure 7.3: Refinement of the canny filtering, eliminating the edge-map components inside the pre-segmentation mask (inside the white contours in (b)).

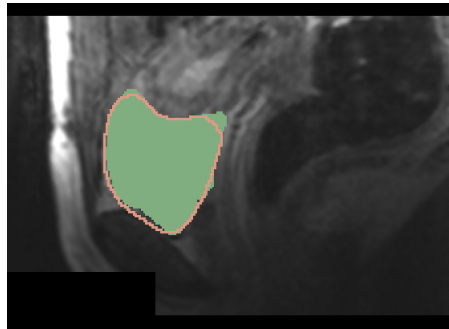
even in case of strong image artifacts (i.e. motion artifacts, bias field and partial volume effects). However, as shown in Figure 7.7, for one of the patients in the image dataset, our method does not provide suitable results. This can mostly be explained since our method does not take into account the configuration of partially empty bladder. It is important to point out that this particular condition is very difficult to address, due to the low contrast and the missing boundary information between the outer wall of the bladder and the surrounding tissues.



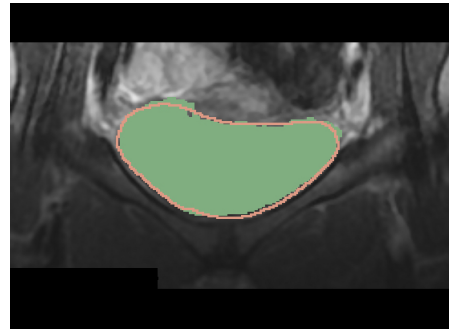
(a) Original image, *sagittal view*.



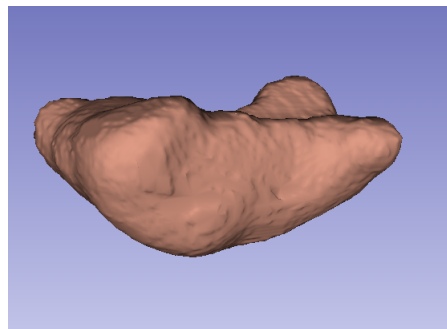
(b) Original image, *coronal view*.



(c) Segmentation, *sagittal view*.

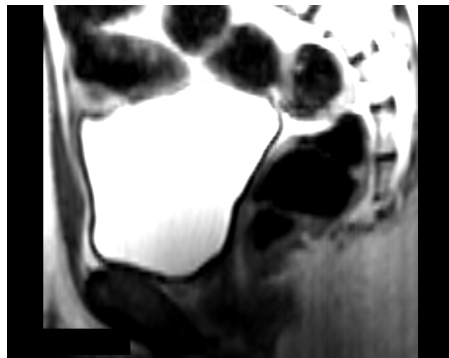


(d) Segmentation, *coronal view*.



(e) 3D Segmentation result.

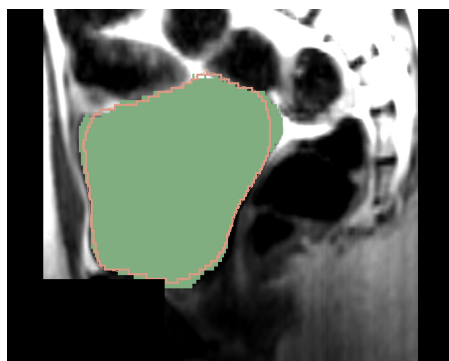
Figure 7.4: Example of segmentation results in case of motion artifacts and partial volume effects. The green label represents the manual segmentation and light brown contour the semi-automatic segmentation.



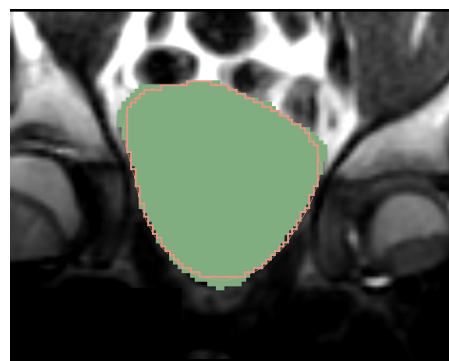
(a) Original image, *sagittal view*.



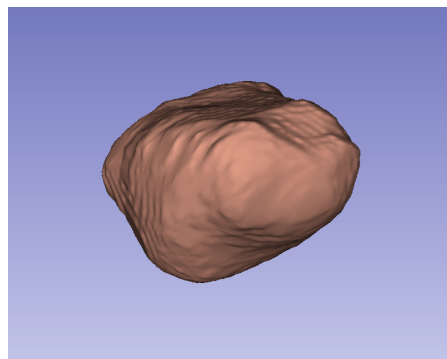
(b) Original image, *coronal view*.



(c) Segmentation, *sagittal view*.

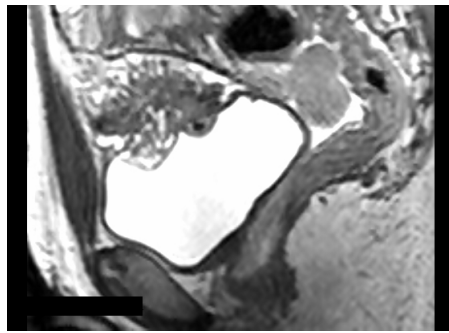


(d) Segmentation, *coronal view*.

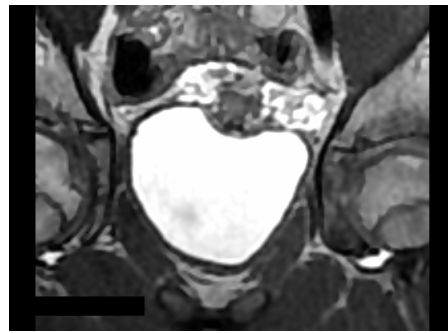


(e) 3D Segmentation result.

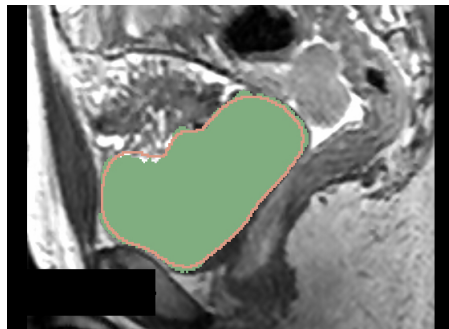
Figure 7.5: Example of segmentation results in case of bias field and partial volume effects. The green label represents the manual segmentation and light brown contour the semi-automatic segmentation.



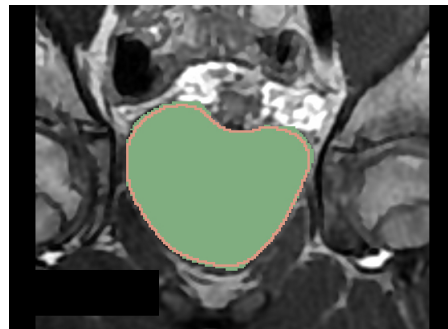
(a) Original image, *sagittal view*.



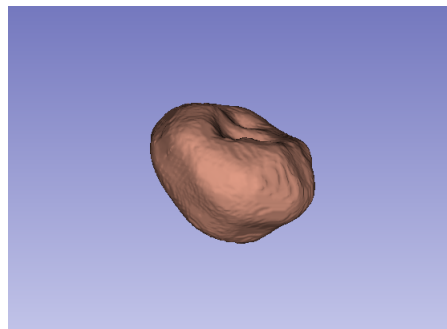
(b) Original image, *coronal view*.



(c) Segmentation, *sagittal view*.

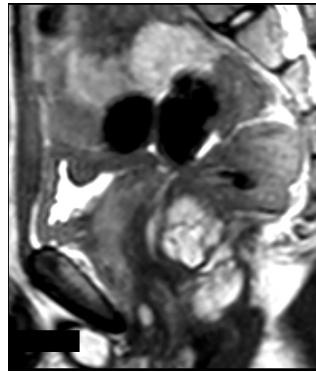


(d) Segmentation, *coronal view*.



(e) 3D Segmentation result.

Figure 7.6: Example of segmentation results in case of slight intensity inhomogeneity of the bladder. The green label represents the manual segmentation and light brown contour the semi-automatic segmentation.



(a) Original image, *sagittal view*.



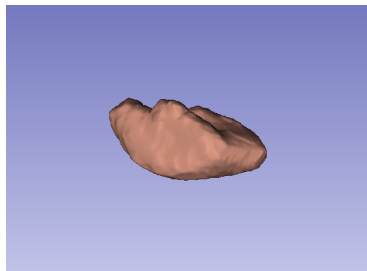
(b) Original image, *coronal view*.



(c) Segmentation, *sagittal view*.



(d) Segmentation, *coronal view*.



(e) 3D Segmentation result.

Figure 7.7: Example of segmentation results of the bladder, in case of partially empty bladder. The green label represents the manual segmentation and light brown contour the semi-automatic segmentation. The semi-automatic segmentation only provides the bright part of the bladder.

7.3.2 Quantitative results

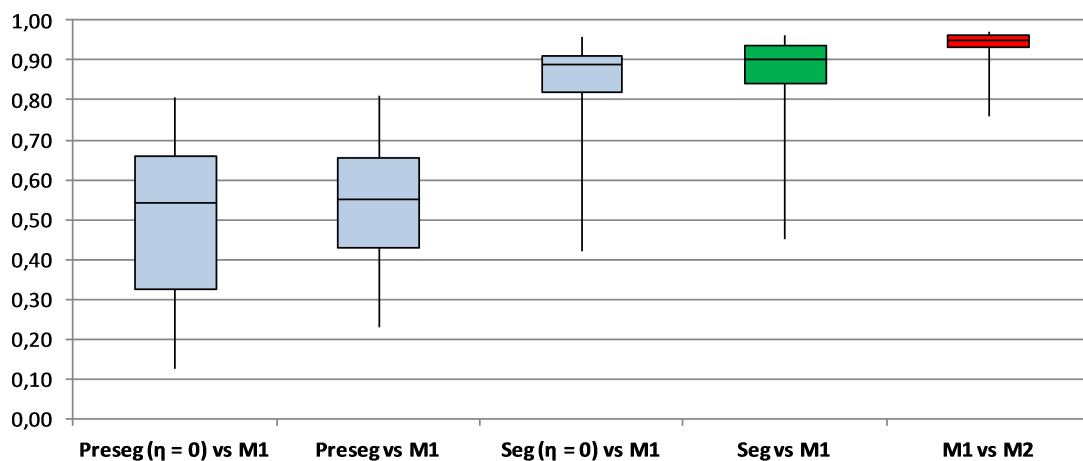
The performances of the proposed method were validated on a dataset of 25 T2-w MRI volumes, through comparisons, in terms of DC and ASSD (see Section 2.3), with manual segmentations performed by medical experts. More precisely, the following comparisons have been performed:

- Pre-segmentation ($\eta = 0$) vs Manual: we estimated the DC and ASSD between the pre-segmentation results obtained as detailed in Section 7.2.2, but discarding the effect of the image L (see Equation 7.4), and the manual segmentations.
- Pre-segmentation vs Manual: we estimated the DC and ASSD between the pre-segmentation results, obtained as detailed in Section 7.2.2, and the manual segmentations.
- Segmentation ($\eta = 0$) vs Manual: we estimated the DC and ASSD between the segmentation results obtained as detailed in Section 7.2.3, using the pre-segmentation ($\eta = 0$) as initialization, and the manual segmentations.
- Segmentation vs Manual: we estimated the DC and ASSD between the segmentation results obtained as detailed in Section 7.2.3, using the pre-segmentation as initialization, and the manual segmentations.

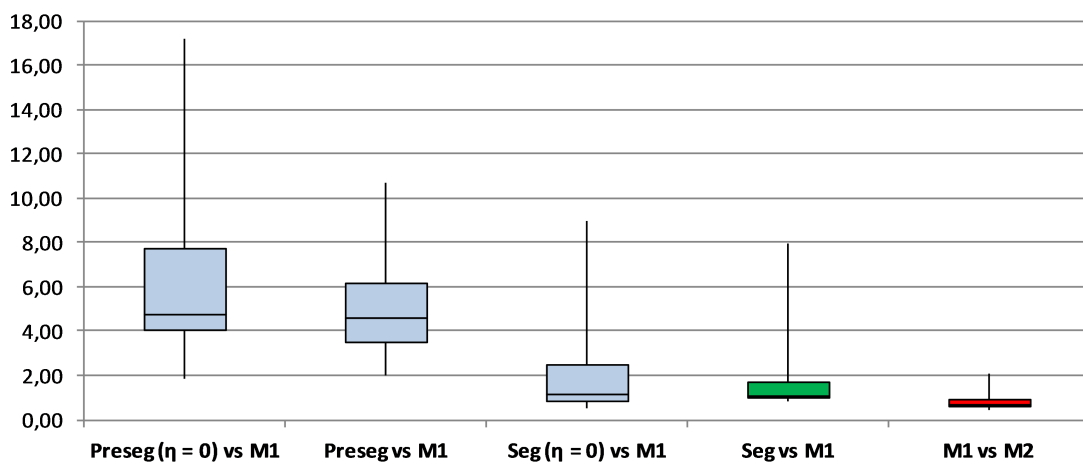
Finally, in order to evaluate the inter-user variability of the manual segmentation results, the DC and the ASSD were also evaluated between the manual segmentations performed by two different users.

The quantitative evaluation in Figure 7.8 shows, on the one side, that the pre-segmentation results, obtained either using the gradient-enhanced image L or not, are relatively low. On the other side, the final segmentations obtained by refining the pre-segmentation results are very accurate, both in terms of DC and ASSD. In particular, the best average results are obtained with the proposed method (green boxplot in Figure 7.8). However, even using our method, the results for one patient are not good enough: it is the case of the partially empty bladder, described in Section 7.3.1 and shown in Figure 7.7.

In order to have a more consistent evaluation of the performances of the proposed method, we also looked at the relation between the DC and the age of the corresponding patients. As it is possible to see in Figure 7.9, the results do not appear to be strongly related with the patients' age, which is encouraging for our pediatric application. However, it is important to remark that our dataset (25 patients) is not large enough to test any statistical assumption on the correlation between DC scores and patients' age, as already mentioned in the previous chapters.



(a) Dice.



(b) ASSD [mm].

Figure 7.8: Quantitative evaluation of the segmentation results in terms of Dice index and ASSD. Each boxplot represent the minimum and maximum values, the 1st and the 3rd quartile and the median value. The green boxplots represent the results obtained using the proposed method. Comparison are done with respect to a first manual segmentation (M1). The red boxplots represent the comparisons between the manual segmentations performed by two different users (M1,M2).

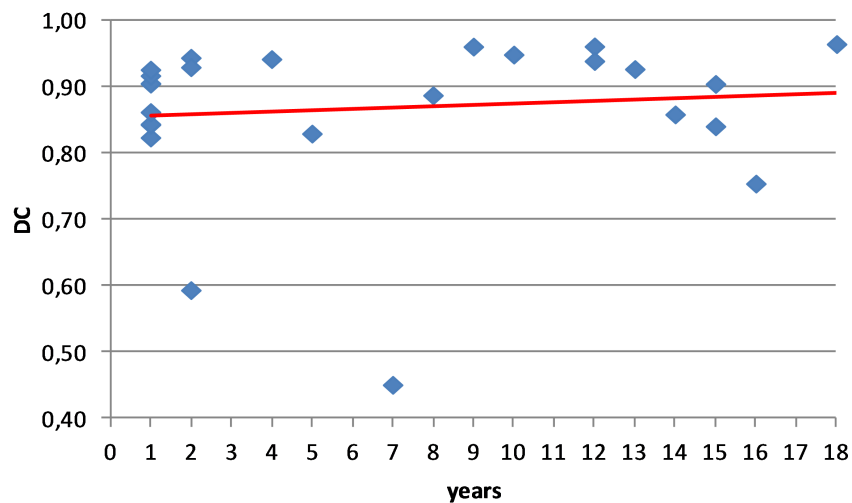


Figure 7.9: Dice score in function of the patients' age and corresponding linear regression line (red).

7.4 Conclusion

7.4.1 Contributions

In this chapter we presented a powerful segmentation tool for the segmentation of the urinary bladder in T2-w MRI images. The proposed method is based on a first pre-segmentation obtained using a modified version of the Chan-Vese [18] level set formulation. In particular, an additional term in the Chan-Vese energy formulation, allows us to give more importance to the large and hyperintense image regions. The pre-segmentation is then used as initialization for a deformable model, which evolves using the Canny edge map of the image, refined by eliminating non meaningful detected contours. Finally, the proposed method was integrated as a plug-in for the software 3D Slicer, delivering a powerful tool and a user-friendly GUI to the clinicians (see Section 8.2 for more details).

The proposed method was evaluated on a varied database of 25 MRI volumes, obtaining an average accuracy in terms of DC and ASSD of $DC = 0.87 \pm 0.12$ and $ASSD = 1.81 \pm 1.56 \text{ mm}$. Moreover, the results were qualitatively appreciated by medical experts and considered suitable for surgical planning applications.

7.4.2 Limits and perspectives

Our method addresses the segmentation of the inner wall of the bladder. Given the image resolution and the surgical planning application, in case of thin bladder wall (i.e. in case of bladder containing a relevant quantity of urine), which is the most frequent condition, our approach provides an accurate representation of the bladder volume. However, in case of partially empty bladder, the thickness of the bladder wall becomes relevant and the explicit segmentation of the outer wall of the bladder needs to be addressed (see Figure 7.7). It is important to remark that some existing methods already addressed this issue [35, 76]. However, these studies were applied to high resolution images of adult patients, in which the bladder wall is much easier to identify than for children.

Another improvement of the proposed method could concern the automatic extraction of a marker inside the bladder region, in order to automate the full procedure avoiding the needs of a user-selected landmark. An idea could be, similarly to [25], to use the relatively stable spatial position of the pelvic bones to extract a ROI containing the bladder. An intensity-based approach could then be used to extract a meaningful landmark. However, this kind of approach could be very sensitive in case of patients with strong tumors or malformations, which can produce strong deformations and/or displacements of the bladder within the pelvic region. Moreover, the selection of one point inside the bladder was not considered a tedious task by the users.

Chapter 8

3D modeling workflow and clinical applications

Abstract

In this chapter we present the integration of the developed segmentation methods into a complete workflow for surgical planning. First, we present the implementation of the developed methods, including GUIs, in the 3D Slicer platform. Secondly, we present the proposed workflow for surgical planning, going from image acquisition to 3D visualization in mobile devices. Finally, we present some clinical cases of patients affected by tumors and malformations, which are very interesting to show the potentials of 3D modeling in a surgical context.

Contents

8.1	Introduction	91
8.2	Graphical user interfaces	91
8.3	3D patient specific modeling workflow	97
8.4	Some clinical applications	99

8.1 Introduction

As discussed in Chapter 1, the aim of this work is to enhance surgical planning for pediatric patients, thanks to the introduction of patients specific 3D models in the clinical workflow. In this context, the generation of the patient 3D models, through dedicated segmentation methods (Chapters 5-7), is the first crucial challenge. However, in order to efficiently introduce the 3D modeling in the clinical workflow, two important considerations have to be done: i) the developed segmentation methods have to be used by clinicians, not necessarily with an image processing background, and ii) the generated 3D models have to be easily visualized and shared within the surgical staff. For these reasons, i) we decided to implement the developed methods as user friendly plug-ins in the 3D Slicer platform [38] (Section 8.2), and ii) we set-up a few steps workflow for 3D modeling, going from image acquisition to 3D visualization (Section 8.3).

Finally, in order to show the potential benefits of 3D modeling for surgical planning, we present in Section 8.4 some clinical cases of patients affected by tumors or malformations. Some of these examples also show the benefits of using 3D models during the post-operative phase.

8.2 Graphical user interfaces

As discussed in Chapter 4, 3D Slicer was chosen for the implementation of the segmentation methods described in Chapters 5-7. This choice was motivated by the modularity of the software architecture (please refer to [38] for further details), which allows us to easily extend the software capabilities with dedicated tools. Moreover, extensive documentation and tutorials for developers are provided. Another advantage of 3D Slicer is that it offers several interesting tools, such as easy-to-use manual segmentation tools and tractography tools. This allows us to obtain, within the same platform, complete patient-specific 3D models, including nerves fibers and structures for which dedicated methods have not been developed yet (e.g. colon, muscles, tumors).

The main GUI of 3D Slicer, depicting also the developed plug-ins, is shown in Figure 8.1. The patient's MRI image (DICOM) is first loaded from this GUI. Then the user can directly access to the developed plugins. The GUIs of the developed plug-ins, which were kept as simple as possible, are depicted in Figures 8.2-8.4.

The main user interaction steps, for each developed plugin, are:

- **Bones segmentation:** the user is first asked to input the patient data (age and sex). This information is used to automatically choose the closest anatomical bones template (see Section 5.2.1) for the pre-segmentation pro-

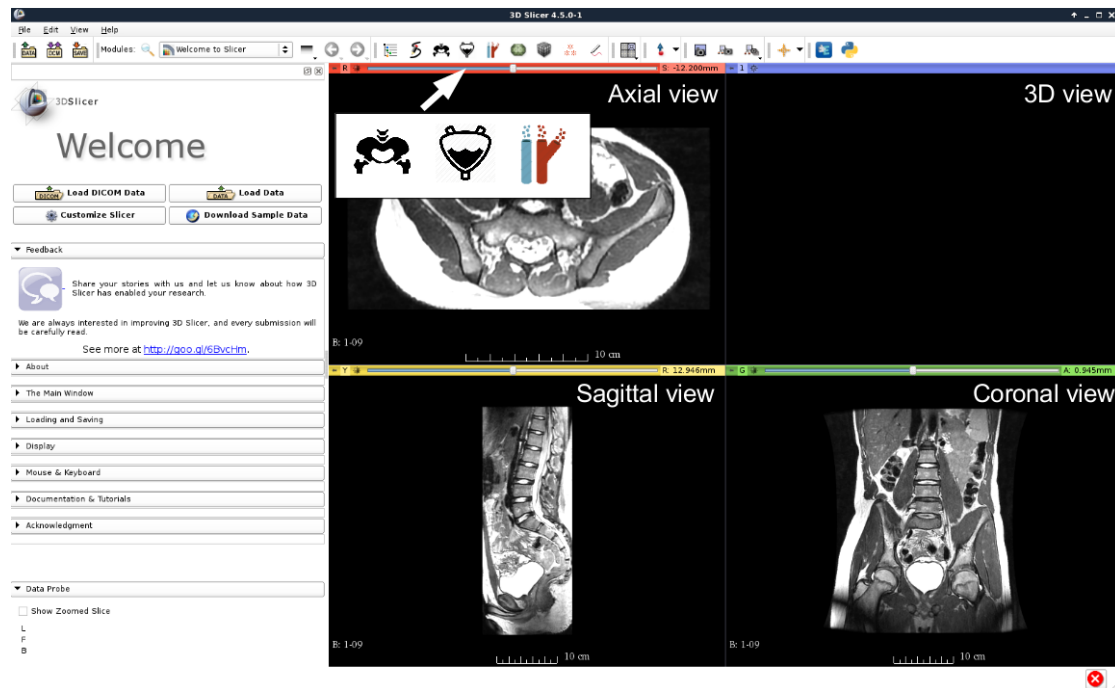


Figure 8.1: Main 3D Slicer [38] GUI. The dedicated methods for pelvic bones, vessels and bladder segmentation were implemented as plug-ins in the software platform.

cedure. Then the user performs interactively the template registration (see Section 5.2.2). This mainly consists in placing couples of landmarks, one in the template image and one in the MRI, at the corresponding anatomical positions. This procedure is performed iteratively and, for each couple of selected landmarks, the pre-segmentation is updated. This allows the user to stop the landmark selection procedure when he is satisfied by the pre-segmentation result. Then, by clicking "apply", the final segmentation is performed (see Section 5.2.3) and the 3D model is generated. These steps are automatic.

- **Vessels segmentation:** the user selects a set of landmarks inside the vessels of interest. This procedure is normally performed by navigating through the axial slices, where the vessels section are more clearly visible. Note that no particular order is required during the landmark selection procedure. When clicking on "apply", the vessels paths are reconstructed (Section 6.2.1), the segmentation is performed (see Section 6.2.2) and the 3D model is generated. No further interaction is required for these steps.
- **Bladder segmentation:** similarly to the vessels plugin, the user is asked

to select one landmark inside the bladder region. When clicking on "apply", the segmentation is performed (Section 7.2) and the 3D model is generated, again automatically.

It is important to remark that, once the target structures are segmented using the developed plug-ins, the user has the possibility to manually refine the segmentation results. This can be done using several tools, such as "draw" or "paint", already implemented in 3D Slicer.

The design of the proposed GUIs was the result of a strict collaboration with the surgeons involved in the project, who particularly appreciated the usability of the proposed solutions.

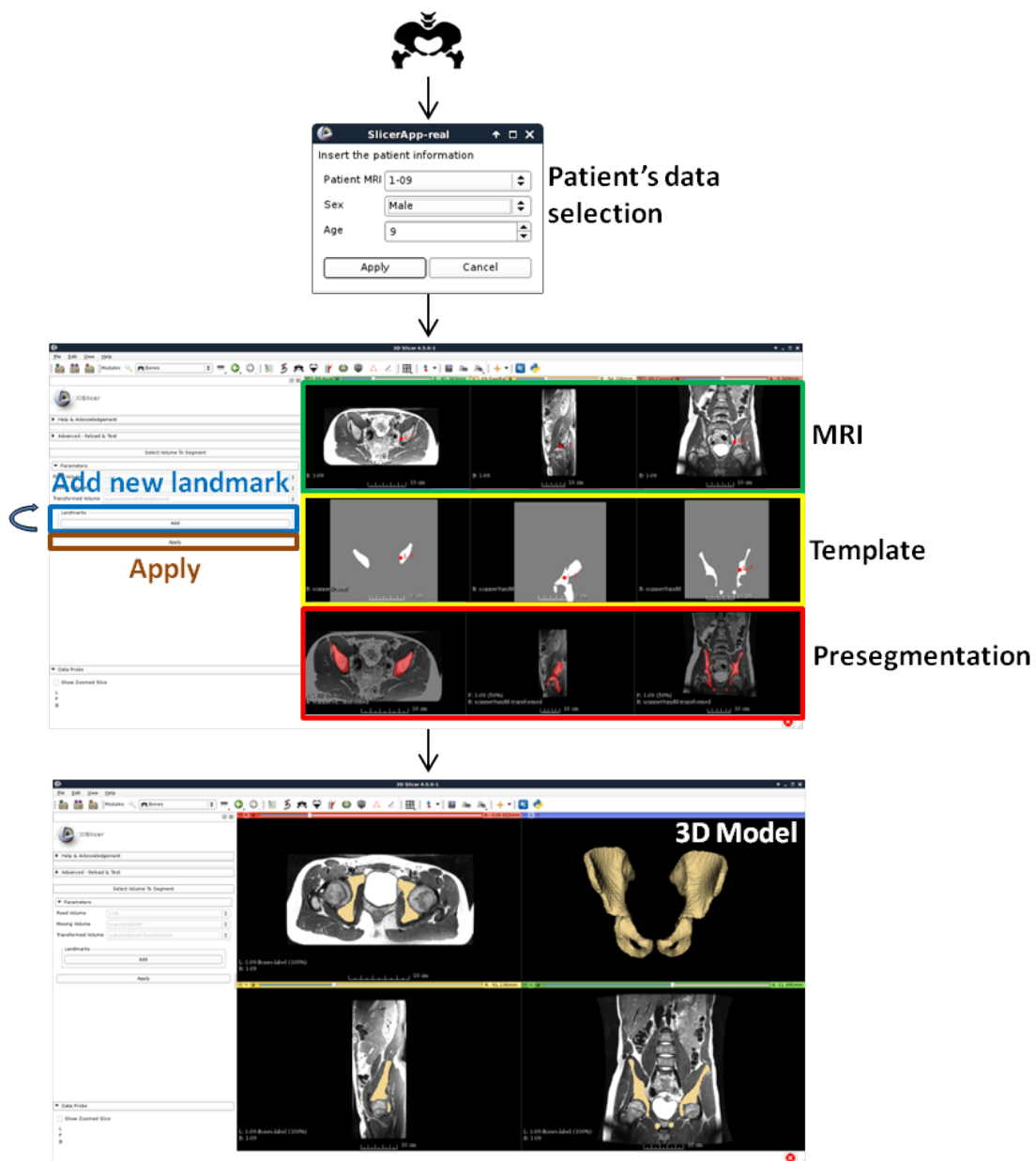


Figure 8.2: Pelvic bones segmentation plug-in. i) The user inputs the patient's data. ii) The user performs the template registration, selecting iteratively couples of landmarks (one in the template and one in the MRI). The pre-segmentation (red label) is updated at each couple of landmarks selection. iii) When clicking on "apply" the final segmentation is performed and the 3D model is generated.

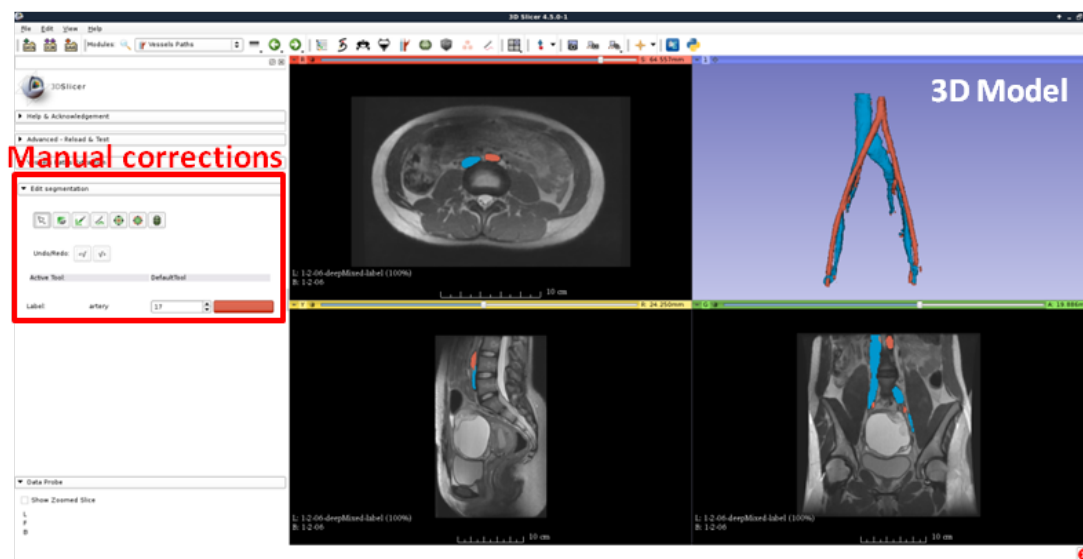
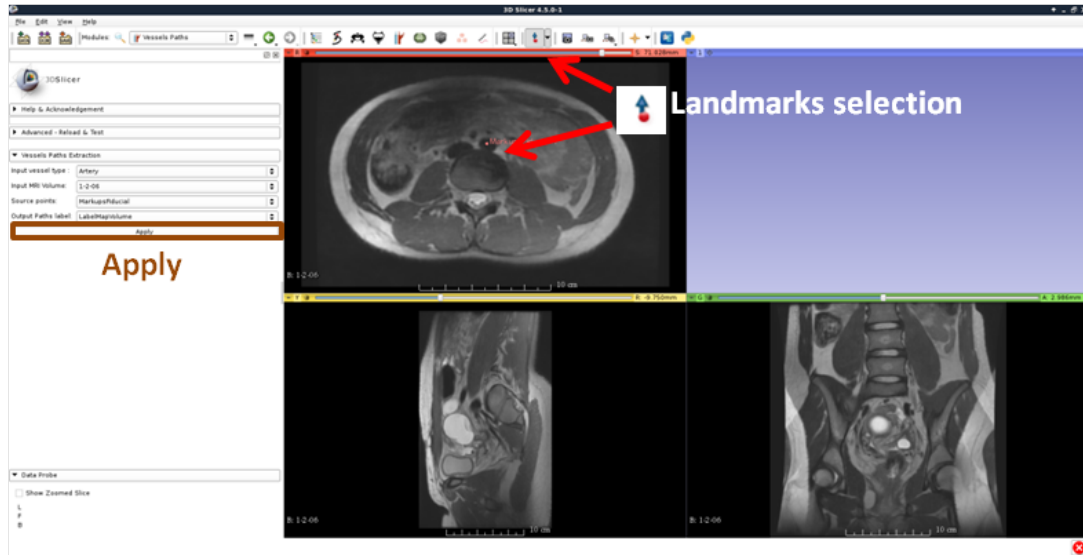


Figure 8.3: Pelvic vessels segmentation plug-in. i) The user selects a set of landmarks inside the vessels of interest. ii) When clicking on "apply", the segmentation is performed and the 3D model is generated. A new screen for eventual manual corrections is also displayed.

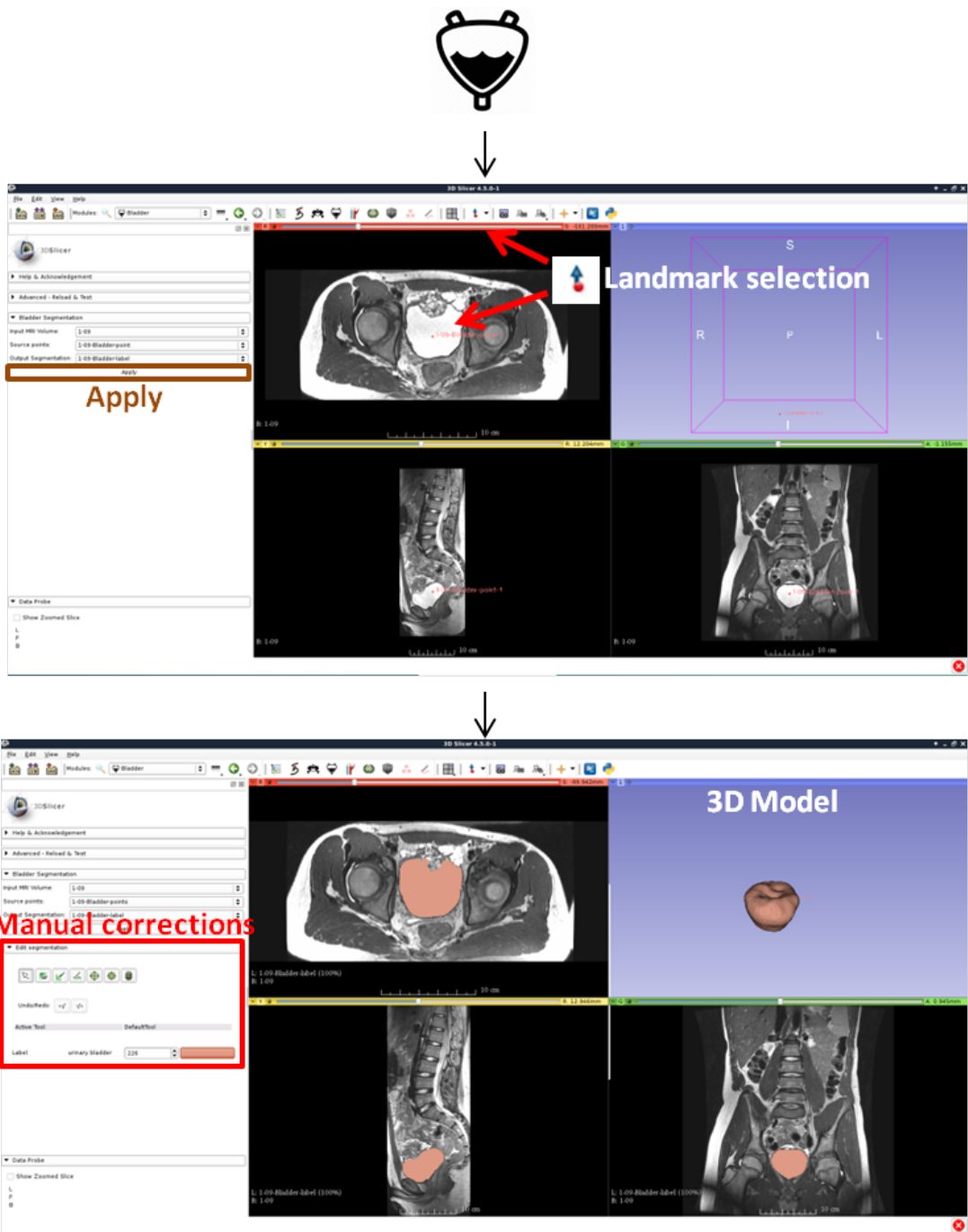


Figure 8.4: Bladder segmentation plug-in. i) The user selects one landmark inside the bladder. ii) When clicking on "apply", the segmentation is performed and the 3D model is generated. A new screen for eventual manual corrections (e.g. partially empty bladder) is also displayed.

8.3 3D patient specific modeling workflow

The adopted workflow for patient-specific 3D modeling procedure, from image acquisition to 3D visualization, is depicted in Figure 8.5. Once the MRI acquisition is performed, the patient's data and the clinical report are uploaded into the PACS (picture archiving and communication system). The PACS can be accessed from multiple dedicated workstations within the hospital, which allows surgeons to download the patient's MRI (DICOM) on the local workstation dedicated to the creation of the 3D models. Once downloaded, the patient's data are immediately anonymized with a dedicated software. The anonymized DICOM images are then processed by the surgeon within the 3D Slicer platform, opportunely extended with the developed segmentation plugins, in order to generate the patient specific 3D models. These models are then saved (.obj, .stl or .vtk formats) on the local server and are directly accessible for 3D visualization within the 3D Slicer platform. However, using this configuration, the surgeon can access 3D models only from the 3D modeling workstation. This could strongly limit the effective integration of 3D modeling in the clinical workflow. For this reason, the patients 3D models (collected into a compressed folder exportable from 3D Slicer) are uploaded on a database hosted on the server of the Imagine Institute. This database is accessible through the web platform "eCohorte"¹, developed by the Data Science group of the Imagine Institute. In this way, the patients 3D models can be downloaded with any connected mobile device and visualized with several free mobile applications (e.g. Emb3D² and many others). This allows the clinicians to access the 3D models remotely, without the need of a fixed workstation. This could be particularly useful, for instance:

- during the patients and parents information phase, both in the pre-operative and post-operative periods;
- during the surgical staff meetings, where the clinical case is discussed and the surgical planning is established;
- during the intervention, by connecting the device to fixed screens (see Figure 8.6), in order to have an enhanced visualization of the patient's anatomy.

¹<http://www.institutimagine.org/fr/la-recherche/8-plateformes-technologiques/260-data-science.html>

²<https://www.emb3d.com/>

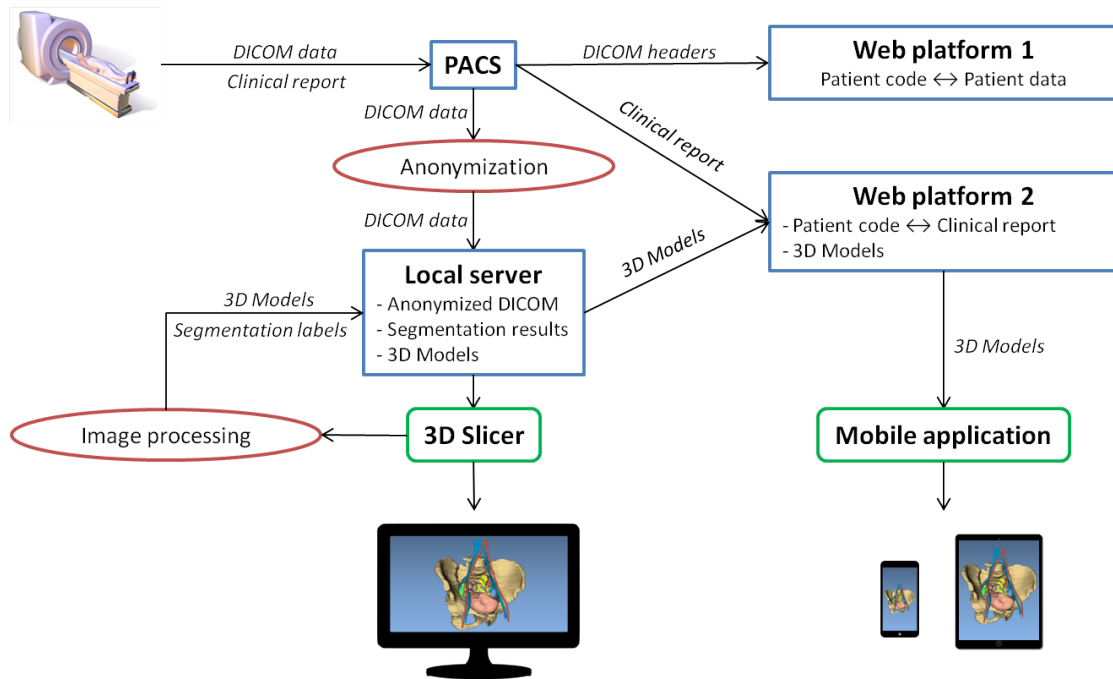


Figure 8.5: 3D modeling framework, from image acquisition to 3D visualization.

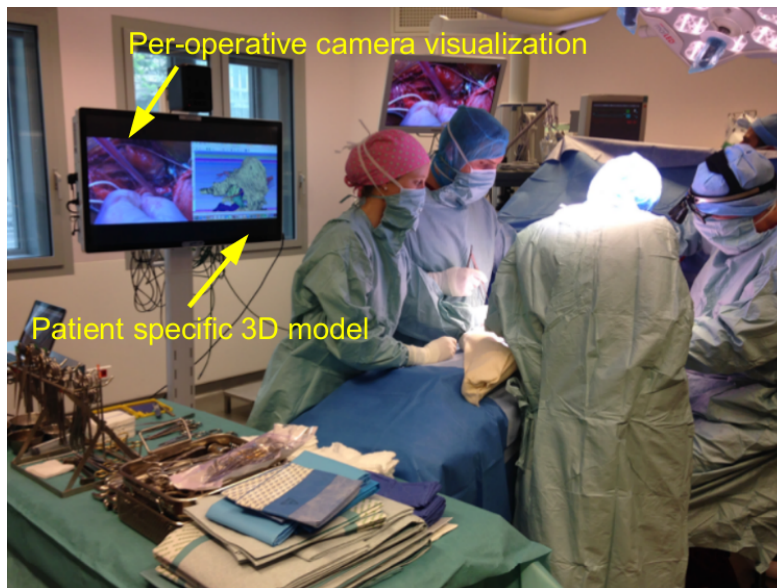


Figure 8.6: Integration of the patients specific 3D models in the surgical room, here for a classical open intervention.

8.4 Some clinical applications

As introduced in Chapter 1, patient specific 3D modeling can be extremely useful for the two major fields of pediatric surgery: tumors and malformations.

In oncology, 3D modeling can be extremely useful in daily practice for surgical planning, allowing the surgeons to better understand the spatial relationships between the tumor and the surrounding structures. In fact, a correct anatomical understanding can help during the tumor resection procedure, preserving as much as possible the surrounding structures. For instance, Figure 8.7 depicts the clinical relevance of the 3D segmentation, notably of the pelvic vessels, in a pediatric patient (8 years old) affected by ovarian teratoma. The patient specific 3D model eases the analysis of the spatial relations between the tumor and the right iliac vessels, which are essential for surgical planning.

Figure 8.8 depicts the 3D modeling of a 7 years-old patient with a rhabdomyosarcoma of the right obturator muscle, which has complex interactions with the surrounding structures (notably with the pelvic bones).

Another relevant clinical example, with particular focus on 3D modeling of the pelvic nerves, is presented in Figure 8.9. It depicts the 3D modeling, obtained from pre-operative and post-operative images, of a patient affected by neurofibroma. In particular, the pre-operative 3D model shows the tumor, which was removed through robotic surgery, in close contact with the sacral plexus. In the weeks following the operation, the patient presented sensory deficits of the left leg calf and of the plantar vault. The post-operative neurotractogram confirms partial interruption of left S2 sacral root, which is consistent with the patient's clinical symptoms. First, this case validates the accuracy of the pelvic network anatomy delivered by pelvic neurotractography. Secondly, it demonstrates its importance in surgical planning in order to improve patients outcome (it is important to remark that, for this case, both 3D models were performed during the post-operative period).

Pelvic malformations, especially ARM [3], are another kind of diseases which can particularly benefit from 3D modeling. In fact, these rare pediatric pathologies strongly modify the standard patient's anatomy, which becomes particularly complex to analyze by visual analysis of the MRI images (slice by slice). A particularly complex case of ARM is depicted in Figure 8.10. It depicts the 3D modeling of a pediatric patient (9 years old) affected by cloacal malformation, which consists on confluence of the rectum, vagina, and urethra into a single common channel. The 3D model helps understanding this complex anatomy and planning the surgery.

It is important to remark that these 3D models, even if strongly appreciated by the surgeons, were used in a research context and that a rigorous clinical validation will be necessary for their introduction in clinical practice.

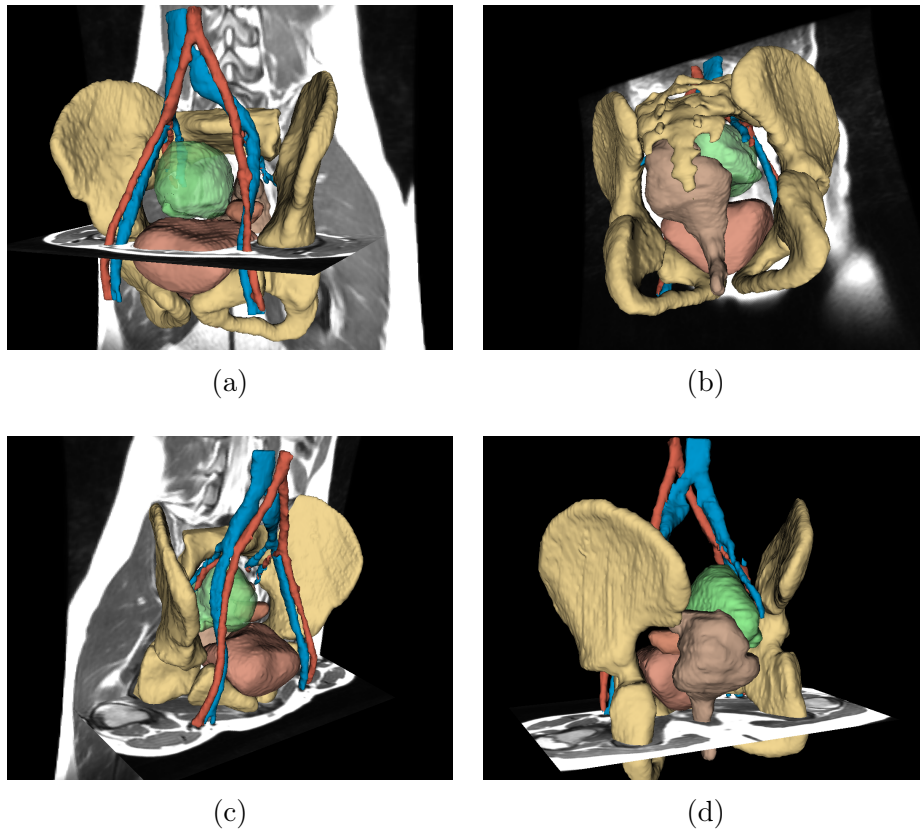


Figure 8.7: Example of 3D patient specific pelvic model of a 8 years old patient, affected by ovarian teratoma (green). The arteries (red), the veins (blue), the bladder (light brown) and the bones (yellow) are segmented with the proposed methods. The other pelvic structures (sacrum, colon, and left ovary) are manually segmented.

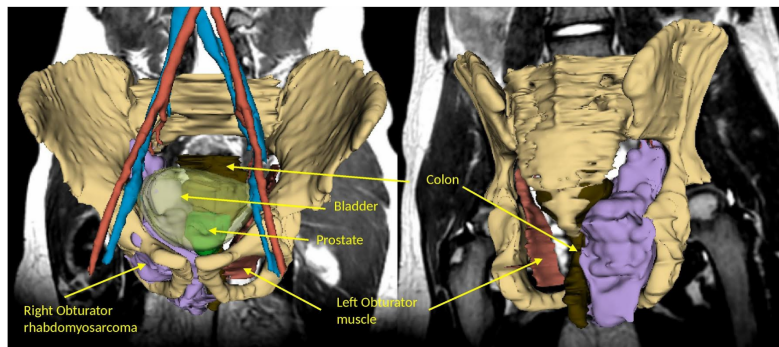
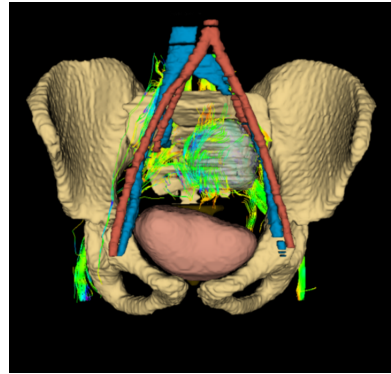


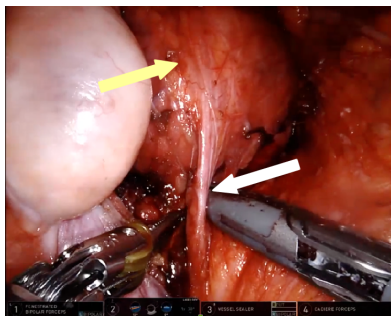
Figure 8.8: 3D modeling of a 7 years-old patient with a rhabdomyosarcoma of the right obturator muscle (anterior and posterior views). Note the complex 3D shape of the tumor and its spatial relations with the surrounding structures.



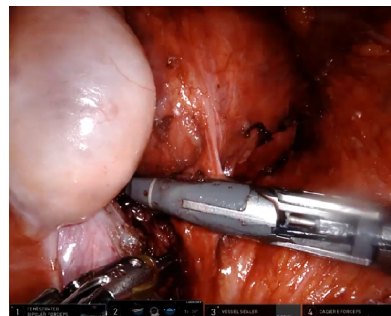
(a) Pre-operative MRI slice.



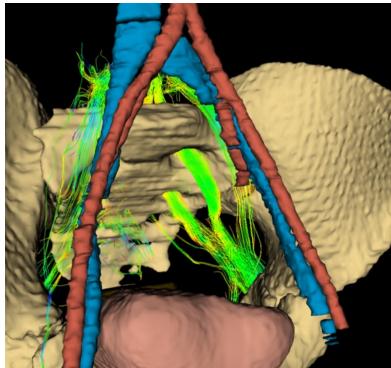
(b) Pre-operative 3D model.



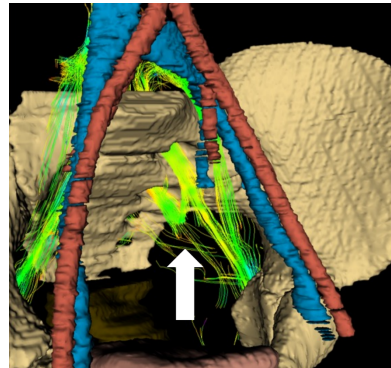
(c) Surgery.



(d) Surgery, potential nerve cut.



(e) Pre-operative 3D model.



(f) Post-operative 3D model.

Figure 8.9: Pre-operative (e) and post-operative (f) 3D modeling of a patient affected by pelvic neurofibroma. The tumor is indicated with a yellow arrow in (a) and with the gray label in (b). Images in (c) and (d) were taken during the robotic surgery intervention. In (c) the tumor is indicated with a yellow arrow and the potential nerve with a white arrow. The tumor is not depicted in (e) for better visibility of the left sacral roots.

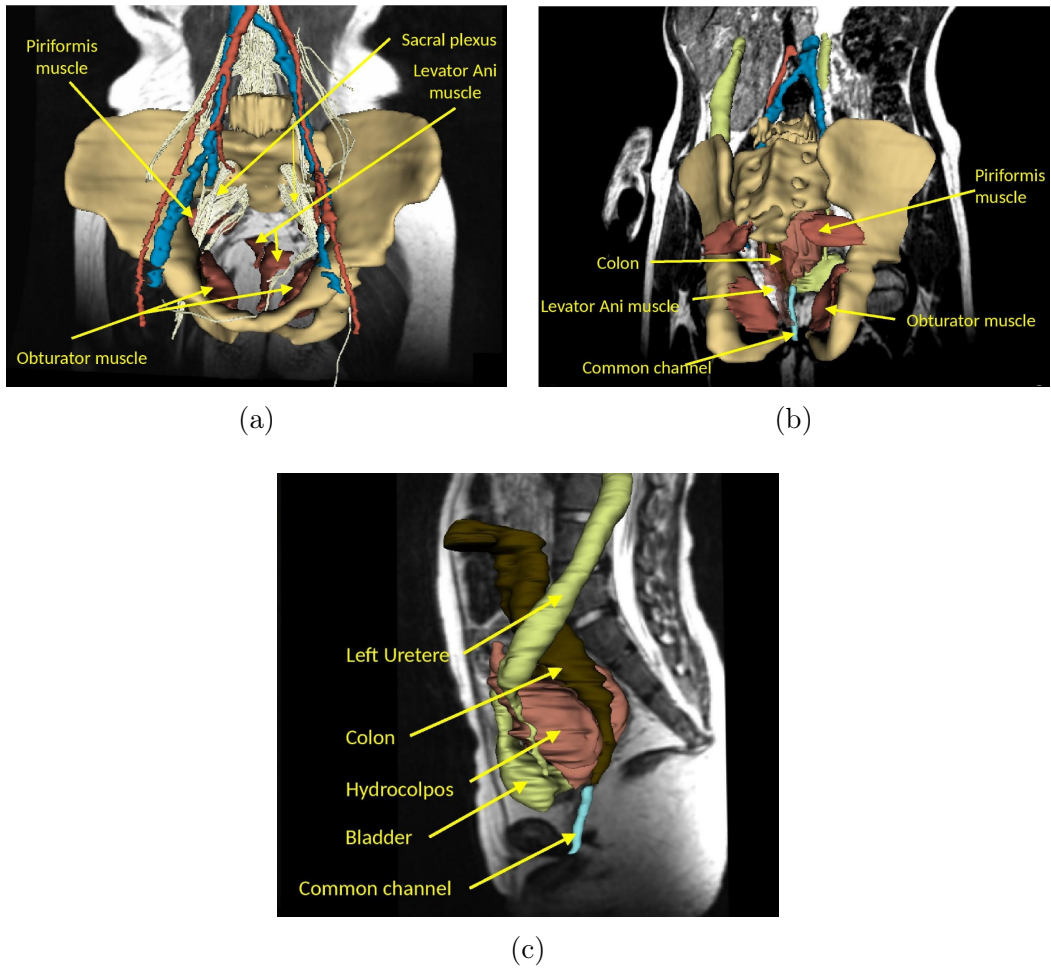


Figure 8.10: 3D modeling of a 9 years old patient with a non repaired cloacal malformation. (a) Coronal view integrating the sacral tractogram. Note the asymmetry of levator ani muscles. (b) Coronal posterior view, showing the muscular system and the common channel. (c) Left sagittal view. Note the compression by the hydrocolpos (distension of the vagina caused by accumulation of fluid due to the vaginal obstruction) on the left uretere.

Chapter 9

Conclusion and future work

9.1 Conclusion

A clear understanding of the patient's anatomy is essential for the surgical planning procedure. This is especially the case for the pelvic region, in which most of the involved structures are soft and deformable, leading to a strong anatomical inter-patient variability. This variability is even more important in pediatrics, where the anatomy varies with the patient's age. Moreover, all these difficulties are clearly emphasized in case of rare tumors and malformations.

In this context, patient specific 3D modeling, obtained from segmentation of MRI images, can be an extremely powerful tool to enhance surgical planning, which is the main aim of this work.

However, in the literature, there is a strong lack of segmentation methods for pelvic structures in pediatric images. In fact, the segmentation task is more difficult in pediatric images than in adult images, because of the nature of the target structures (e.g. shape variability during growth, high partial volume effect) and harder constraints on the imaging acquisitions (e.g. no CT or angiography acquisitions, low image resolution).

For this reason, the first part of this work consisted on the evaluation of the surgeons' capabilities to obtain patient specific 3D models, using existing software tools. We analyzed and extensively evaluated a set of 3D segmentation and visualization platforms, which can be used for pelvic MRI images. This review was a major contribution of this work, and it was the first review, to the best of our knowledge, that took into account the segmentation performances in its analysis. With this review, on the one hand, we provided generic guidelines for the choice of the most suitable software tools for surgeons that would like to introduce a 3D patient-specific pelvic model, obtained from MRI, in their surgical planning routine. On the other hand, we quantitatively demonstrated that none

of the analyzed software tools meets the time criteria for segmentation needed in clinical practice for pelvic interventions in pediatric patients. This clearly justifies the need of developing dedicated segmentation methods for pelvis structures in pediatric MRI. Finally, this review allowed us to define the development strategy for the novel segmentation methods: we chose 3D Slicer as core software platform for developing the segmentation methods, as dedicated plugins.

In particular, in this work, we focused on three main pelvic structures: the pelvic bones, the pelvic vessels and the bladder.

Concerning the pelvic bones, most of the existing methods were applied to CT images, using intensity-based approaches, or to adult images using strong shape priors in terms of atlases or statistical shape models, without taking into account the bones variability during growth. In order to solve this issue, we proposed a semi-automatic method, based on template registration and deformable models. The main contribution of this work was the introduction of a set of bones templates, specific for different patients ages, in the segmentation pipeline. This allowed us to take into account the variability in terms of connectivity of the bones during growth. Moreover, using a user-guided landmark registration procedure, we also handled the bones shape variability between patients. The final automatic processing step refined the segmentation using a deformable model in which regularization parameters depend on the local curvature of the bones. This is relevant since pelvic bones contain both almost flat zones and strong curved ones. Moreover, the user-selected landmarks, needed for the previous registration step, were used as fixed anchors during the deformable model evolution. The results obtained with the proposed method were positively evaluated, both quantitatively and qualitatively, by pediatric surgeons for surgical planning applications. Potential limits of our approach could concern cases of extreme pelvic bones malformations (e.g. missing part of the bones). It could then be very difficult to register the anatomical templates (representing standard bones anatomy) to such complex cases, even with a user-guided registration. However, it is important to remark that such cases are very rare and that they were not present in our patients dataset.

Concerning the pelvic vessels, most of the existing studies were applied to angiography images, which present strong vessels enhancement, and they are not easy to extend to MRI images. We proposed a patch-based deep learning approach using transfer learning. The main contribution of this work was the design of a semi-automatic method for the patches extraction, based on the structural information of the pelvic vascular tree. This approach allows the user to focus, for each patient, on the vascular structures of surgical interest, while avoiding potential unexpected results. We also propose to use pseudo-RGB color patches, that incorporate the 3D information of successive slices. The use of these patches makes it possible to exploit a 2D CNN pre-trained on the ImageNet dataset, which

allows us to train the network with a small training dataset. This is fundamental for medical applications where the number of annotated images is limited. The results obtained with the proposed method were positively evaluated, even though some local vein/artery classification errors, by pediatric surgeons for surgical planning applications. Potential limits of our work could concern cases of vessels with complex 3D paths, such as the small pelvic vessels. In fact, the proposed method relies on the hypothesis that the vessels branches are descending along the cranio-caudal direction, which is the case for the main pelvic vessels (aorta, vena cava, iliac arteries and veins) but not necessarily for small vessels. However, it is important to remark that these small vessels are not clearly visible in our images, due to their limited spatial resolution, and that they are not extremely relevant for surgical planning applications.

For the bladder, most of the existing segmentation methods were developed for CT images. However, none of the proposed methods was evaluated on pediatric populations, which generally present higher intensity inhomogeneities and higher partial volume effects. We proposed to apply a simple method based on deformable models. A first pre-segmentation is obtained using a modified version of the Chan-Vese level set formulation. The pre-segmentation is then used as initialization for a parametric deformable model, which evolves using the Canny edge map of the image, refined by eliminating non meaningful detected contours. Also in this case, the segmentation results were quantitatively and qualitatively evaluated, and overall appreciated, by pediatric surgeons. The main limit of our approach is that it does not take into account the outer wall of the bladder, which can produce unsatisfying results for patients with partially empty bladder. However, it is important to remark that, for most of the patients, the bladder wall thickness is negligible, also due to the limited images resolution.

All these segmentation methods were integrated in 3D Slicer, delivering powerful tools and user-friendly GUIs to the clinicians. Furthermore, we set up a processing and portability workflow for visualization of the 3D patient-specific models. This allowed surgeons to generate, visualize and share within the hospital the 3D models, thus enhancing the patient's anatomy understanding and, consequently, the surgical planning.

Finally, we also proposed a preliminary approach for 3D modeling of the pelvic nervous system, using DWI and tractography, which showed promising results for the spine nerves of sacral plexus.

In conclusion, we developed a set of segmentation tools for pediatric MRI images, which are fully integrated in a complete workflow for surgical planning, from image acquisition to 3D visualization.

9.2 Perspectives

Bones segmentation Concerning bones segmentation, potential improvements could concern the landmarks selection procedure. First, a future work could concern the automatic extraction (e.g. using machine learning methods) of meaningful landmarks in the MRI volume, in order to reduce the user interaction time. These landmarks could be used, for instance, to obtain a first rough template registration, that could be eventually refined by the user (e.g. by manually placing additional landmarks). Secondly, another potential improvement of the proposed method could concern the refinement of the landmarks position (e.g. based on local image features, such as the intensity gradients). This could allow dealing with potential inaccurate landmark selection by the user.

Other relevant improvements could concern the anatomical bones templates. First, it could be interesting to explore strategies to choose the anatomically closest template instead of the closest age, in order to cope with potential abnormal child development. This would require to define an appropriate similarity measure between a template and an MRI image. Secondly, it will be interesting to take the bones shape variability into account, in the segmentation framework, for given ranges of ages. This could be done, for instance, by building a statistical shape model for each range of ages, instead of choosing only one anatomical template. However, this would need many annotated MRI images, which are not currently available in pediatrics.

Vessels segmentation A potential improvement to the proposed methods could be to post-process our results in order to improve the vein/artery classification. This could be done, for instance, by analyzing the spatial consistency of the classes along the entire 3D model. Moreover, it could be interesting to investigate other methodologies that take into account the 3D information using more than three successive slices (e.g. directly using efficient implementations of 3D CNN, once more annotated data will be collected).

Bladder segmentation A potential improvement of the proposed bladder segmentation method could concern the segmentation of the outer wall of the bladder, which it was not addressed in our work. This could be done, similarly to other proposed methods [35, 76], using the already segmented inner bladder wall as initialization for a deformable model approach. However, in pediatrics, the extremely low contrast between the outer wall of the bladder and the surrounding tissues should be taken into account in the segmentation framework.

3D modeling of other pelvic structures This work addressed the segmentation of three pelvic structures: the bones, the vessels and the bladder. However, in order to obtain a complete patient specific 3D model, specific tools still have to be developed for other important structures, such as the colon, the genital system and the eventual tumors. For this reason a future work could address the challenging issue of segmentation of these structures. Moreover, as already done for the other structures, these methods should be implemented as 3D Slicer plugins, in order to provide a full set of usable and integrated segmentation tools to the user. Moreover, our preliminary work on the 3D modeling of nerve fibers has to be opportunely extended, aiming to reduce false positives and to model also the most peripheral nerves.

Non-overlapping constraints In this work, we decided to address independently the segmentation of each pelvic structure, in order to give higher flexibility to the segmentation pipeline. This is particularly important in case of pathologies, such as tumors and malformations, which can strongly modify the patients anatomy (e.g. missing structures or abnormal spatial relations between structures). However, once generated the complete patient specific 3D model, the spatial relations between the segmented structures could be extremely useful to refine the segmentation results. For instance, a potential improvement of our work could concern the introduction, in the segmentation pipeline, of non-overlapping constraints between the segmented structures. This will result in a better consistency of the segmentation results between the different target structures and, consequently, in a more accurate patient specific 3D model.

Clinical evaluation Going further with the evaluation of the proposed segmentation methods, results should be validated on a larger patients dataset, which will require more manually annotated images. Moreover, in order to quantify the benefits of patient specific 3D models for pediatric patients, affected by pelvic tumors or malformations, a dedicated clinical study would be necessary. For instance, interesting evaluations could concern the number of surgical strategy modifications after visualizing the 3D models. The assessment of surgical outcome and patient's follow up could also benefit from 3D models, for instance by comparing patient's 3D models before and after the surgery.

From surgical planning to image guided surgery In the long term, an extremely interesting application could concern the integration of the 3D models in the per-operative visualization, in order to guide the surgical act. For robotic surgery, this would require a real time overlay of the pre-operative 3D models in the screen of the robot console. This is particularly challenging for the pelvis, and

even more in pediatrics, mainly because of the strong structures displacements and deformations during the surgical procedure compared with their positions and shapes in the pre-operative images.

Appendix A

Pelvic tractography

Abstract

This appendix presents a preliminary work on the integration of nerve fibers, obtained by tractography algorithms, into the patient specific pelvic 3D model. We propose to rely on whole-pelvis tractography, which provides a large set of fiber tracts within the pelvic region, and on a dedicated fiber segmentation approach. In particular, we propose to extract the sacral plexus using the prior anatomical knowledge on the nerves fiber paths respect to a set of predefined anatomical structures. This part of the work was done in collaboration with Alessandro Delmonte (research engineer at IMAG2 laboratory, Imagine Institute) and Cécile Muller (pediatric surgeon, PhD candidate at IMAG2 laboratory, Imagine Institute).

Contents

A.1 Introduction	110
A.1.1 Context	110
A.1.2 Diffusion MRI and tractography	110
A.2 Pelvic tractography segmentation	113
A.2.1 Modeling the spatial relations	113
A.2.2 Definition of the main pelvic nerves paths	116
A.3 Preliminary results	118
A.4 Conclusion	120

A.1 Introduction

A.1.1 Context

The pelvic nervous system is extremely complex and difficult to observe. In the literature, its anatomical description is based on ex-vivo analysis of adult patients. The evolution of the pelvic nervous anatomy during growth and its modifications in pathological cases (e.g. malformation) is currently poorly known.

In the context of pelvic surgery, preserving peripheral nerves is essential: any lesion of the nervous system may have a major impact on the patients' quality of life, especially in children. Unfortunately, in clinical practice, the patient's specific nervous anatomy is generally not analyzed during surgical planning, due to the lack of imaging techniques routinely available for its visualization. Indeed, due to their small size, peripheral nerves are extremely difficult to see in CT or in standard anatomical MRI images.

In the literature, studies on nerve fibers analysis are mostly focused on brain white matter. They rely on tractography algorithms applied to diffusion MRI images.

A.1.2 Diffusion MRI and tractography

Diffusion MRI is an imaging technique that estimates the water particles diffusion, also called Brownian motion [54], in a tissue, along a certain spatial direction. One of the mostly used extensions of Diffusion MRI is called *Diffusion Tensor Imaging* (DTI) [68], which estimates the diffusion property of the tissues in multiple directions, creating a diffusion matrix (a tensor) that characterizes the anisotropic behavior of water particles in the 3D space. This diffusion tensor can be considered as a three-dimensional structure with three principal diffusivities (eigenvalues) associated with three mutually perpendicular principal directions (eigenvectors).

The directional and magnitude information of the anisotropic diffusion of the individual voxels can be combined together in order to reconstruct the paths of fiber tracts. This technique, also known as *tractography*, relies on the assumption that adjacent voxels with a similar orientation of their principal anisotropic diffusion direction are likely to belong to the same fiber tract [57].

Several tractography algorithms exist, based either on deterministic or probabilistic approaches [29]. The formers, which are the most intuitive ones, are based on three main steps: i) initialization, ii) propagation and iii) termination. The initialization consists in choosing a set of points (or seeds), from which fibers will be tracked. The propagation mainly consists in connecting image points based on the diffusivity values along the principal diffusion direction. Finally, the termination consists in stopping the fiber tracking under given conditions. The termination

criteria are generally based on the values of anisotropic diffusion, the length and the local curvature of the reconstructed fibers.

Depending on the initialization approach, it is possible to divide tractography methods in two groups:

- **ROI-based tractography** The most common method for isolating groups of fibers (or bundles), based on tractography, is the manual placement of regions of interest (ROIs) into the images, which are used as starting seeds for the algorithm (e.g. in [116] for the pelvic nerves). Other inclusion or exclusion ROIs can also be eventually selected to refine the tractography results (e.g. in [85]). However the ROI selection procedure is tedious, time consuming and the results are poorly reproducible [140].
- **Whole-image tractography** Different approaches create seed points within the entire image, in order to generate a model of the whole fibers inside the image. These methods generate a huge number of fiber tracts, which are very difficult to analyze, both qualitatively and quantitatively (see Figure A.1a). For this reason, in order to keep only the relevant (or to "segment") fiber tracts, post-processing steps are usually required. The post processing could rely, for instance, on clustering algorithms [88, 124, 125] or, similarly to the ROI-based methods, on inclusion or exclusion criteria within predefined ROIs [2, 123] (see Figure A.1).

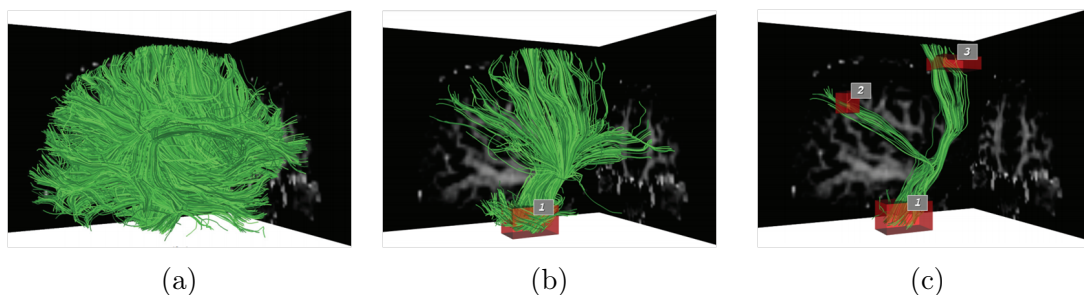


Figure A.1: Example of segmentation of white matter tracts. (a) Whole-brain tractography. (b) Tracts segmentation using the relation *crossing (1)*. Tracts segmentation using the relation $\{crossing (1) AND crossing (2)\} OR \{crossing (1) AND crossing (3)\}$. Figure drawn from [2].

On the one hand, the drawback of clustering algorithms is that, while automatically grouping similar fibers, it is very difficult to incorporate meaningful anatomical information in their formulation. On the other hand, manual selection of ROIs is tedious, poorly reproducible and the inclusion/exclusion criteria could

not be sufficient for describing fiber tracts with convoluted paths (e.g. most of peripheral pelvic nerves). For this reason, in [126], the authors propose to describe the different white matter fiber tracts by defining their spatial relations (e.g. crossing, anterior, superior, endpoints in, ...) with predefined anatomical structures, obtained from automated segmentation of the brain tissues (see Figure A.2). In this way, the authors provide an easy way of describing (and segment) even complex fiber tracts thanks to the clinicians anatomical knowledge, represented in a near-to-English textual language.

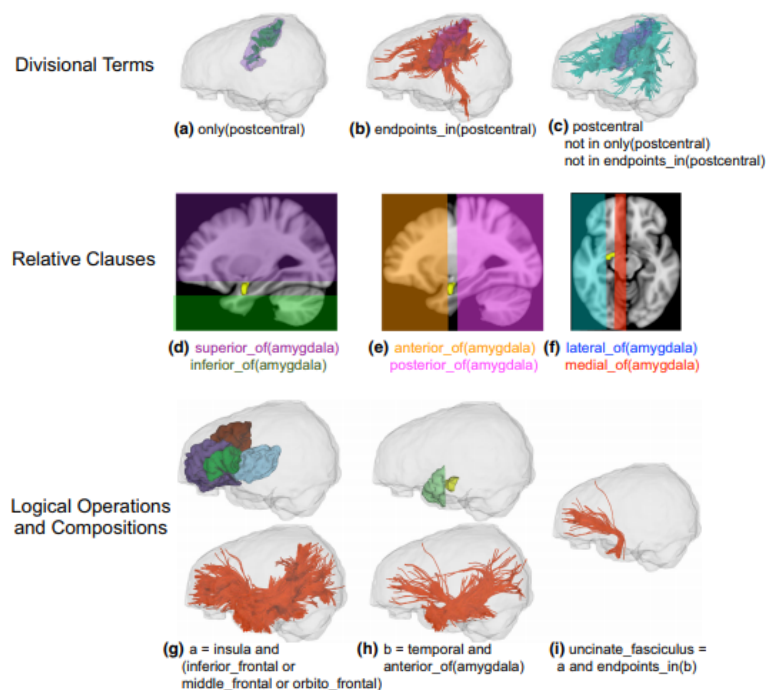


Figure A.2: Schematic example of the work in [126], applied to white matter tracts segmentation.

This approach, due to its flexibility, seems particularly interesting for pelvic tractography applications. However, for the pelvis, there is a strong lack of peripheral nerves descriptions that could be directly used in a computational framework. In fact, in the pelvis, the fiber paths descriptions often refer to anatomical regions that are very difficult to identify in the MRI images (e.g. the great sciatic foramen, which is a region defined by two pelvic ligaments which are extremely difficult to see in MRI). For this reason a new set of definitions, which rely on structures that can be identified and segmented from standard MRI images (in our application, from T2-w MRI), is essential.

Another difficulty of the pelvic application is that the pelvis is composed of a

large number of soft tissues with high diffusivity (e.g. the muscles), This is not the case for the brain, where only the white matter, which is the structure of interest, has diffusion properties. Moreover, the pelvic images are generally noisier than the brain ones, especially in pediatrics, due to higher patients motion. An example of whole-pelvis tractography is depicted in Figure A.3.

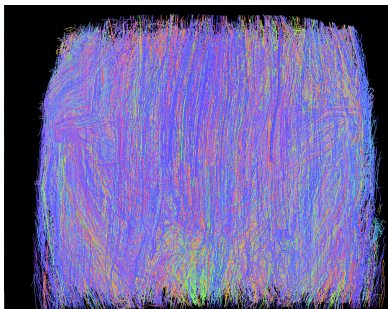


Figure A.3: Example of whole-pelvis tractography (coronal view).

A.2 Pelvic tractography segmentation

In order to extend the method in [126] to the segmentation of the pelvic nervous system, we propose i) an alternative modeling for the spatial relations and ii) a new set of definitions for the pelvic nerves paths.

A.2.1 Modeling the spatial relations

As it is possible to see in Figure A.2, in [126] the authors propose to model the directional spatial relations (e.g. superior, inferior, ...) with standard bounding boxes. On the one hand, this type of representation has the advantage to be very easy to compute. On the other hand, it could not be optimal to represent spatial relations with respect to small structures or with complex shape.

For this reason, we propose to model the spatial relations using a *directional cone*, whose aperture Φ represents the strictness of the spatial relation, which can be tuned by the user. A schematic representation of this modeling is shown in Figure A.4. This is a simplification of the fuzzy relations defined in [9], which proved to be sufficient in this preliminary application and it is faster to compute.

This way of modeling spatial relations was employed for the following definitions: *anterior*, *posterior*, *superior*, *inferior*, *medial* and *lateral*. The *medial* and *lateral* definitions were preferred to the *right* and *left* ones, since the former ones

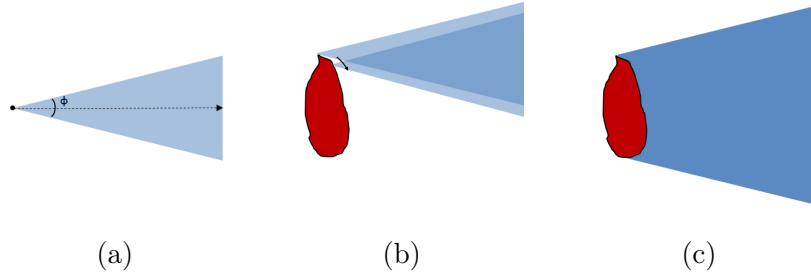


Figure A.4: Example of the modeling of the spatial relation $right_of(Structure)$ in a 2D plane. (a) Primitive cone, with axis directed along the right direction and aperture angle Φ . (b) The primitive cone is translated in each border point (black) of the reference structure (red). This can also be expressed as a *dilation* of the reference structure, using the cone as structuring element. (c) Final spatial dilation (blue), obtained as the union of all the border points dilations, representing the $right_of$ region of the reference structure.

are the mostly used in the medical terminology. Moreover, since the pelvic structures of interest are symmetric with respect to the sagittal plane, this avoid to duplicate *left* and *right* relations.

Another contribution with respect to the study in [126], is the definition of two other spatial relations: *between* and *proximity*. Concerning the *between* relation, the axis of the directional cone is aligned with the segment joining the center of mass of the two structures. The directional spatial dilations are then computed separately for the two structures and their intersection is kept as final *between* region (see Figure A.5). This is again a simplification of the dilation-based method proposed in [9]. The *proximity* relation is represented by thresholding the distance transform, in mm , of the reference structure (see Figure A.6).

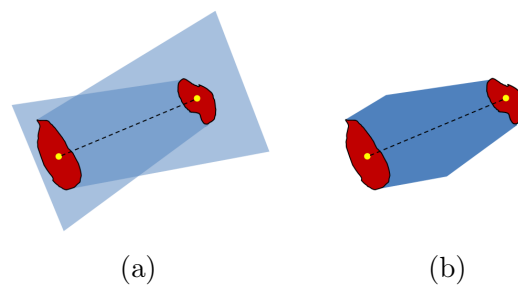


Figure A.5: Graphic representation of the *between* relation. (a) The spatial dilations (light blue) are computed separately for the two reference structures (red). (b) The *between* spatial dilation (blue), obtained as intersection of the single-structure dilations. The structures centers of mass are depicted in yellow.



Figure A.6: Graphic representation of the *proximity* relation. The reference structure is depicted in red, the proximity region is depicted in blue.

The complete list of spatial and pathway relations is detailed in Table A.1. Note that the pathway relations are the same as the ones described in [126].

	Relations
Spatial relations	anterior_of(Structure, Aperture, Percentage) posterior_of(Structure, Aperture, Percentage) superior_of(Structure, Aperture, Percentage) inferior_of(Structure, Aperture, Percentage) medial_of(Structure, Aperture, Percentage) lateral_of(Structure, Aperture, Percentage) between(Structure1, Structure2, Percentage) proximity_of(Structure, Length, Percentage)
Pathway relations	crossing(Structure, Percentage) only_in(Structure) not_in(Structure) endpoints_in(Structure) both_endpoints_in(Structure)

Table A.1: *Structure* represents the reference anatomical structure, from which the spatial relation is computed. *Aperture* $[0, \pi]$ represents angle of the directional cone, tuning the strictness of the spatial relation. *Percentage* $[0, 100]$ represents the percentage of a given fiber tract that must lie inside a spatial dilation, in order to satisfy the relation.

A.2.2 Definition of the main pelvic nerves paths

The spatial and pathway relations detailed in Table A.1 can be combined together, using AND, OR and NOT operators, in order to obtain the definitions (or *queries*) of pelvic nerves paths of interest. In particular, the first nervous structures of interest concern the sacral plexus: the sacral spine nerves S1, S2, S3, S4 and the lumbar spinal nerve L5. For a detailed anatomical description of the sacral plexus refer to [34].

From a detailed analysis of the sacral plexus anatomy, we define the following queries (the input parameters, such as *Aperture* and *Percentage*, are here omitted for better readability):

- L5 = crossing(VertebralCanalL5)
and (not posterior_of(Sacrum))
and posterior_of(Vein)
and posterior_of(Artery)
and posterior_of(Uretere)
and proximity_of(Uretere)
and posterior_of(Ovary)
and proximity_of(Ovary))
and anterior_of(PiriformisMuscle)
and superior_of(IschialSpine)
and anterior_of(IschialSpine)
and posterior_of(ObturatorMuscle)
and not crossing(SacralHoleS1)
and not crossing(SacralHoleS2)
and not crossing(SacralHoleS3)
and not crossing(SacralHoleS4)
and not (anterior_of(LevatorAniMuscle)
or posterior_of(LevatorAniMuscle))
and anterior_of(L5Vertebra)
and posterior_of(L5Vertebra)
- S1 = crossing(SacralHoleS1)
and anterior_of(Sacrum)
and posterior_of(Vein)
and posterior_of(Artery)
and posterior_of(Ovary)
and superior_of(PiriformisMuscle)
and anterior_of(PiriformisMuscle)
and superior_of(IschialSpine)
and anterior_of(IschialSpine)

- and posterior_of(ObturatorMuscle)
 - and not crossing(SacralHoleS2)
 - and not crossing(SacralHoleS3)
 - and not crossing(SacralHoleS4)
 - and not crossing(VertebralCanalL5)
 - and not (anterior_of(LevatorAniMuscle)
 - or posterior_of(LevatorAniMuscle))
 - and anterior_of(L5Vertebra)
 - and posterior_of(L5Vertebra)
- S2 = crossing(SacralHoleS2)
 - and anterior_of(Sacrum)
 - and posterior_of(Vein)
 - and posterior_of(Artery)
 - and posterior_of(Ovary)
 - and lateral_of(Colon)
 - and lateral_of(Genital)
 - and superior_of(PiriformisMuscle)
 - and anterior_of(PiriformisMuscle)
 - and superior_of(IschialSpine)
 - and anterior_of(IschialSpine)
 - and posterior_of(ObturatorMuscle)
 - and not crossing(SacralHoleS1)
 - and not crossing(SacralHoleS3)
 - and not crossing(SacralHoleS4)
 - and not crossing(VertebralCanalL5)
 - and not (anterior_of(LevatorAniMuscle)
 - or posterior_of(LevatorAniMuscle))
- S3 = crossing(SacralHoleS3)
 - and anterior_of(PiriformisMuscle)
 - and medial_of(PiriformisMuscle)
 - and posterior_of(Vein)
 - and posterior_of(Artery)
 - and posterior_of(Ovary)
 - and lateral_of(Colon)
 - and lateral_of(Genital)
 - and superior_of(IschialSpine)
 - and anterior_of(IschialSpine)
 - and posterior_of(ObturatorMuscle)
 - and not crossing(SacralHoleS1)


```

and not crossing(SacralHoleS2)
and not crossing(SacralHoleS4)
and not crossing(VertebralCanalL5)
and not (anterior_of(LevatorAniMuscle)
or posterior_of(LevatorAniMuscle,aperture=0))
S4 = crossing(SacralHoleS4)
and inferior_of(PiriformisMuscle)
and superior_of(CoccygealMuscle)
and posterior_of(Colon)
and lateral_of(Colon)
and posterior_of(Genital)
and lateral_of(Genital)
and posterior_of(Ovary)
and posterior_of(Uretere)
and superior_of(IschialSpine)
and anterior_of(IschialSpine)
and (not crossing(SacralHoleS1))
and (not crossing(SacralHoleS2))
and (not crossing(SacralHoleS3))
and (not crossing(VertebralCanalL5))
and not (posterior_of(LevatorAniMuscle)
or anterior_of(LevatorAniMuscle))

```

A.3 Preliminary results

We performed whole-pelvis tractography (see Figure A.3) for one control adult patient and we segmented the sacral plexus using the queries previously defined. The reference anatomical structures were segmented from T2-w MRI, either with the developed semi-automatic tools (see Chapters 5, 6 and 7) or manually. The patient specific 3D model including these structures is depicted in Figure A.7. The choice of using one adult patient for this evaluation was mostly due to i) the difficulties of segmenting all the structures needed for the queries (e.g. the muscles) in pediatric patients, and ii) the need for images with low noise. With this test, we wanted to show a first proof-of-concept of tractography segmentation using spatial relations. The complete definition of queries and their use for pediatric tracts recognition is still ongoing.

The proposed method, as depicted in Figure A.8, provides promising visual results of the sacral plexus tracts from whole-pelvis tractography. However, the segmented tractography contains a large number of false positives fiber tracts (in particular for S4), which makes the results not yet sufficient for surgical planning

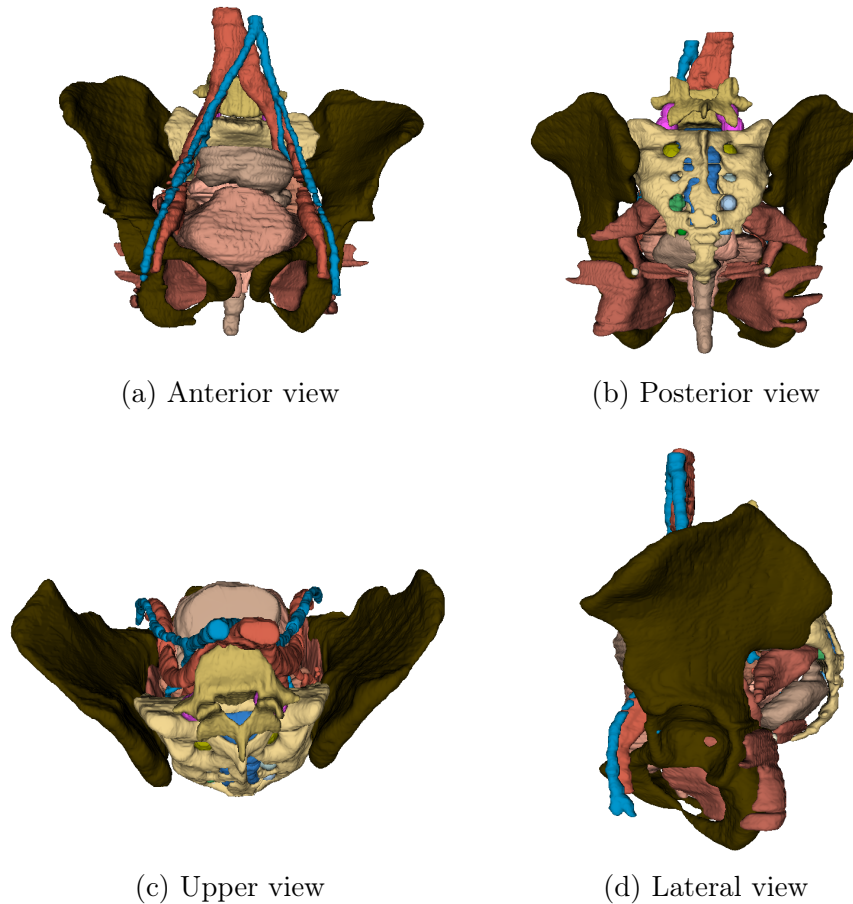


Figure A.7: Patient specific 3D model of a control adult patient, including all the structures needed for the queries defined in Section A.2.2.

applications. For this reason, a refinement of the proposed queries is necessary to address this issue. It is also important to remark that these results could also be improved with a better tuning of the tractography algorithm parameters, such as the termination criteria (see Section A.1.2 for details).

Even if the main objective of the introduction of the queries was the segmentation of the whole-pelvis tractography, another interesting application is their application for refinement (or filtering) of the results obtained by standard ROI-based methods. In fact, even performing tractography starting from a set of user-selected seeds, false positives are often present (see Figure A.9a). Moreover, the filtering procedure, not having to deal with the large number of tracts present in whole-pelvis tractography, can be performed using very simple queries such as, for the complete sacral plexus:

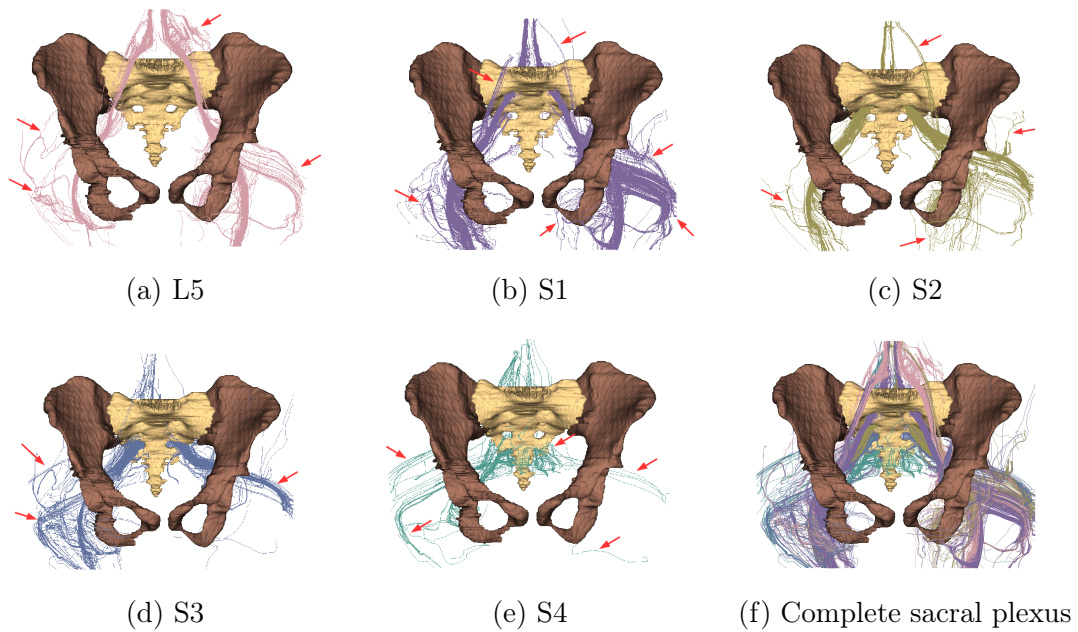


Figure A.8: Whole-pelvis tractography segmentation results for the sacral plexus. Groups of false positive fiber tracks are indicated with red arrows.

- Sacral_Plexus = (crossing(VertebralCanalL5)
and not anterior_(ObturatorMuscle))
or (crossing(SacralHoleS1)
and not (anterior_(LevatorAniMuscle)
or posterior_(LevatorAniMuscle)))
or crossing(SacralHoleS2)
or crossing(SacralHoleS3)

It is important to note that the S4 spinal nerve was not detected using the ROI-based method, which motivates the absence of a corresponding query.

A.4 Conclusion

Pelvic nerves 3D modeling is nowadays a major challenge in order to enhance surgical planning, both for pediatric and adult patients. In pediatrics, the 3D models of nerves may also be useful to better describe the anomalies of the spinal cord and/or muscles frequently associated, for instance, with ARM. This should be useful not only to refine the classification of these malformations, but also to evaluate the impact of the different types of surgical approaches and of potential rehabilitation techniques (neuromodulation, physiotherapy).

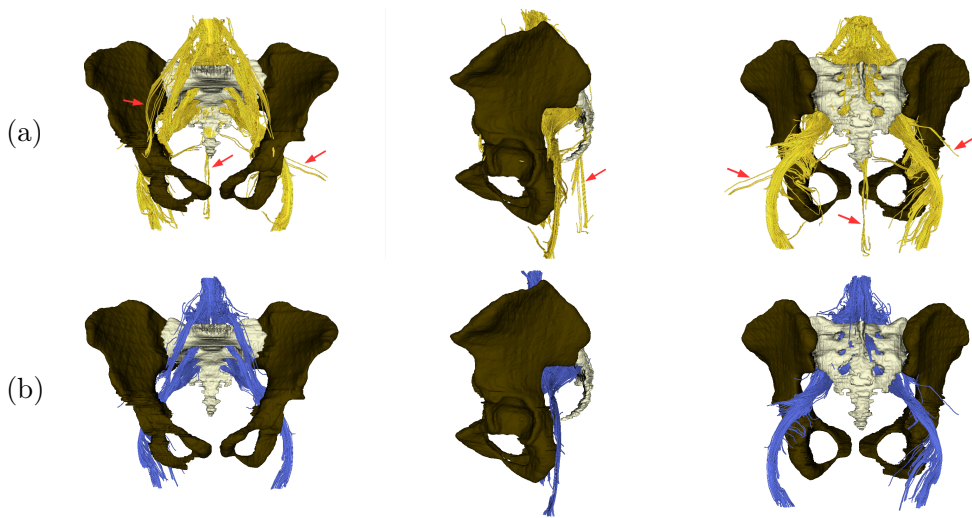


Figure A.9: Filtering of the ROI-based tractography thanks to the nerves paths queries. (a) ROI-based tractography (yellow) with anatomically incoherent fiber tracts (red arrows), (b) refined tractography (blue).

ROI-based tractography methods are the only ones that were previously applied to the pelvic region (e.g. in [116]), leading to promising results for the sacral plexus (from L4 to S3). However, the manual placement of the seeds is very tedious and poorly reproducible. Moreover, the manual procedure is very complex, which lead to discard the modeling of the most peripheral pelvic nerves (which are actually the most relevant in the surgical context).

A potential solution to these problems could be to bypass the manual seeds placement, by applying whole-pelvis tractography. For this reason, we proposed a novel approach for extracting the sacral plexus from whole-pelvis tractography, based on the anatomical description of the nerve fibers paths with respect to the surrounding anatomical structures.

Due to the exploratory nature of this work, we tested our approach only on one control adult patient and we obtained promising visual results on sacral plexus 3D modeling. However, due to the large number of false positives, these results are not satisfying for surgical planning applications and a great research effort still has to be done. Potential future work could concern: i) more accurate definitions of the nerves fibers paths, and ii) the application of fuzzy spatial relationships [9] in the paths definitions, as also done in [26], which would be extremely useful to model their intrinsic imprecision.

Finally, our method also showed interesting results if used as a filtering approach for the ROI-based tractography, reducing anatomically incoherent false positives fiber tracts.

Bibliography

- [1] ABABNEH, S. Y., PRESCOTT, J. W., AND GURCAN, M. N. Automatic graph-cut based segmentation of bones from knee magnetic resonance images for osteoarthritis research. *Medical Image Analysis* 15, 4 (2011), 438–448.
- [2] AKERS, D., SHERBONDY, A., MACKENZIE, R., DOUGHERTY, R., AND WANDELL, B. Exploration of the brain’s white matter pathways with dynamic queries. In *Proceedings of the conference on Visualization’04* (2004), IEEE Computer Society, pp. 377–384.
- [3] ALAMO, L., MEYRAT, B. J., MEUWLY, J.-Y., MEULI, R. A., AND GUDINCHET, F. Anorectal malformations: finding the pathway out of the labyrinth. *Radiographics* 33, 2 (2013), 491–512.
- [4] ANTUNES, S. G., SILVA, J. S., AND SANTOS, J. B. A level set segmentation method of the four heart cavities in pediatric ultrasound images. In *International Conference Image Analysis and Recognition* (2010), Springer, pp. 99–107.
- [5] AREZOOMAND, S., LEE, W.-S., RAKHRA, K. S., AND BEAULÉ, P. E. A 3D active model framework for segmentation of proximal femur in MR images. *International Journal of Computer Assisted Radiology and Surgery* 10, 1 (2015), 55–66.
- [6] BANIK, S., RANGAYYAN, R. M., AND BOAG, G. S. Delineation of the pelvic girdle in computed tomographic images. In *IEEE Canadian Conference on Electrical and Computer Engineering (CCECE 2008)* (2008), pp. 179–182.
- [7] BANIK, S., RANGAYYAN, R. M., AND BOAG, G. S. Automatic segmentation of the ribs, the vertebral column, and the spinal canal in pediatric computed tomographic images. *Journal of Digital Imaging* 23, 3 (2010), 301–322.

- [8] BAR, Y., DIAMANT, I., WOLF, L., LIEBERMAN, S., KONEN, E., AND GREENSPAN, H. Chest pathology detection using deep learning with non-medical training. In *IEEE 12th International Symposium on Biomedical Imaging (ISBI)* (2015), pp. 294–297.
- [9] BLOCH, I. Fuzzy spatial relationships for image processing and interpretation: a review. *Image and Vision Computing* 23, 2 (2005), 89–110.
- [10] BOOKSTEIN, F. Principal warps: Thin-plate splines and the decomposition of deformations. *IEEE Transactions on Pattern Analysis and Machine Intelligence* 11, 6 (1989), 567–585.
- [11] BOSKAMP, T., RINCK, D., LINK, F., KUMMERLEN, B., STAMM, G., AND MILDENBERGER, P. New vessel analysis tool for morphometric quantification and visualization of vessels in CT and MR imaging data sets. *Radiographics* 24, 1 (2004), 287–297.
- [12] BOURGEAT, P., FRIPP, J., STANWELL, P., RAMADAN, S., AND OURSELIN, S. MR image segmentation of the knee bone using phase information. *Medical Image Analysis* 11, 4 (2007), 325–335.
- [13] BROWN, M. S., FENG, W. C., HALL, T. R., MCNITT-GRAY, M. F., AND CHURCHILL, B. M. Knowledge-based segmentation of pediatric kidneys in CT for measurement of parenchymal volume. *Journal of Computer Assisted Tomography* 25, 4 (2001), 639–648.
- [14] BUENO, G., FISHER, M., BURNHAM, K., MILLS, J., AND HAAS, O. Automatic segmentation of clinical structures for RTP: Evaluation of a morphological approach. In *Medical Image Understanding and Analysis* (2001), pp. 73–76.
- [15] CANNY, J. A computational approach to edge detection. *IEEE Transactions on Pattern Analysis and Machine Intelligence*, 6 (1986), 679–698.
- [16] CARBALLIDO-GAMIO, J., BELONGIE, S. J., AND MAJUMDAR, S. Normalized cuts in 3-D for spinal MRI segmentation. *IEEE Transactions on Medical Imaging* 23, 1 (2004), 36–44.
- [17] CERROLAZA, J. J., SAFDAR, N., PETERS, C. A., MYERS, E., JAGO, J., AND LINGURARU, M. G. Segmentation of kidney in 3D-ultrasound images using Gabor-based appearance models. In *Biomedical Imaging (ISBI), 2014 IEEE 11th International Symposium on* (2014), IEEE, pp. 633–636.

- [18] CHAN, T. F., AND VESE, L. A. Active contours without edges. *IEEE Transactions on Image Processing* 10, 2 (2001), 266–277.
- [19] CHANDRA, S. S., XIA, Y., ENGSTROM, C., CROZIER, S., SCHWARZ, R., AND FRIPP, J. Focused shape models for hip joint segmentation in 3D magnetic resonance images. *Medical Image Analysis* 18, 3 (2014), 567–578.
- [20] CHEN, C., AND ZHENG, G. Fully automatic segmentation of AP pelvis X-rays via random forest regression with efficient feature selection and hierarchical sparse shape composition. *Computer Vision and Image Understanding* 126 (2014), 1 – 10.
- [21] CHU, C., BAI, J., WU, X., AND ZHENG, G. MASCG: multi-atlas segmentation constrained graph method for accurate segmentation of hip CT images. *Medical Image Analysis* 26, 1 (2015), 173–184.
- [22] CIBC, 2016. Seg3D: Volumetric Image Segmentation and Visualization. Scientific Computing and Imaging Institute (SCI), Downloaded from: <http://www.seg3d.org>.
- [23] ÇIÇEK, Ö., ABDULKADIR, A., LIENKAMP, S. S., BROX, T., AND RONEBERGER, O. 3D U-net: learning dense volumetric segmentation from sparse annotation. In *International Conference on Medical Image Computing and Computer-Assisted Intervention (MICCAI)* (2016), Springer, pp. 424–432.
- [24] COHEN, L. D., AND COHEN, I. Finite-element methods for active contour models and balloons for 2-D and 3-D images. *IEEE Transactions on Pattern Analysis and Machine Intelligence* 15, 11 (Nov. 1993), 1131–1147.
- [25] COSTA, M. J., DELINGETTE, H., AND AYACHE, N. Automatic segmentation of the bladder using deformable models. In *Biomedical Imaging: From Nano to Macro, 2007. ISBI 2007. 4th IEEE International Symposium on* (2007), IEEE, pp. 904–907.
- [26] DELMONTE, A., BLOCH, I., HASBOUN, D., MERCIER, C., PALLUD, J., AND GORI, P. Segmentation of White Matter Tractograms Using Fuzzy Spatial Relations. In *Organization for Human Brain Mapping* (Singapore, Singapore, June 2018).
- [27] DENG, J., DONG, W., SOCHER, R., LI, L.-J., LI, K., AND FEI-FEI, L. ImageNet: A Large-Scale Hierarchical Image Database. In *IEEE Conference on Computer Vision and Pattern Recognition (CVPR)* (2009).

- [28] DESCOTEAUX, M., COLLINS, L., AND SIDDIQI, K. A multi-scale geometric flow for segmenting vasculature in MRI. In *Computer Vision and Mathematical Methods in Medical and Biomedical Image Analysis*. Springer, 2004, pp. 169–180.
- [29] DESCOTEAUX, M., DERICHE, R., KNOSCHE, T. R., AND ANWANDER, A. Deterministic and probabilistic tractography based on complex fibre orientation distributions. *IEEE transactions on medical imaging* 28, 2 (2009), 269–286.
- [30] DEVI, C. N., CHANDRASEKHARAN, A., SUNDARARAMAN, V., AND ALEX, Z. C. Neonatal brain MRI segmentation: A review. *Computers in Biology and Medicine* 64 (2015), 163 – 178.
- [31] DICE, L. R. Measures of the amount of ecologic association between species. *Ecology* 26, 3 (1945), 297–302.
- [32] DIETRICH, R., AND KANGARLOO, H. Pelvic abnormalities in children: assessment with MR imaging. *Radiology* 163, 2 (1987), 367–372.
- [33] DOU, Q., YU, L., CHEN, H., JIN, Y., YANG, X., QIN, J., AND HENG, P.-A. 3D deeply supervised network for automated segmentation of volumetric medical images. *Medical Image Analysis* 41 (2017), 40–54.
- [34] DRAKE, R., VOGL, A. W., AND MITCHELL, A. W. *Gray’s Anatomy for Students E-Book*. Elsevier Health Sciences, 2009.
- [35] DUAN, C., LIANG, Z., BAO, S., ZHU, H., WANG, S., ZHANG, G., CHEN, J. J., AND LU, H. A coupled level set framework for bladder wall segmentation with application to MR cystography. *IEEE Transactions on Medical Imaging* 29, 3 (2010), 903–915.
- [36] EHRHARDT, J., HANDELS, H., PLOTZ, W., AND POPPL, S. Atlas-based recognition of anatomical structures and landmarks and the automatic computation of orthopedic parameters. *Methods of Information in Medicine* 43, 4 (2004), 391–397.
- [37] FANG, X.-S., ET AL. The extruded generalized cylinder: A deformable model for object recovery. In *Computer Vision and Pattern Recognition, 1994. Proceedings CVPR’94., 1994 IEEE Computer Society Conference on* (1994), IEEE, pp. 174–181.
- [38] FEDOROV, A., BEICHEL, R., KALPATHY-CRAMER, J., FINET, J., FILLION-ROBIN, J.-C., PUJOL, S., BAUER, C., JENNINGS, D., FENNESSY,

- F., SONKA, M., ET AL. 3D Slicer as an Image Computing Platform for the Quantitative Imaging Network. *Magnetic Resonance Imaging* 30, 9 (2012), 1323–1341.
- [39] FERRARI, V., CARBONE, M., CAPPELLI, C., BONI, L., MELFI, F., FERRARI, M., MOSCA, F., AND PIETRABISSA, A. Value of multidetector computed tomography image segmentation for preoperative planning in general surgery. *Surgical Endoscopy* 26, 3 (Mar 2012), 616–626.
- [40] FISCHL, B. FreeSurfer. *NeuroImage* 62, 2 (2012), 774 – 781.
- [41] FOUQUIER, G., ANQUEZ, J., BLOCH, I., FALIP, C., AND ADAMSBAUM, C. Subcutaneous adipose tissue segmentation in whole-body MRI of children. In *Iberoamerican Congress on Pattern Recognition* (2011), Springer, pp. 97–104.
- [42] FRANGI, A. F., NIESSEN, W. J., VINCKEN, K. L., AND VIERGEVER, M. A. Multiscale vessel enhancement filtering. In *International Conference on Medical Image Computing and Computer-Assisted Intervention (MICCAI)* (1998), Springer, pp. 130–137.
- [43] GANGWAR, T., CALDER, J., TAKAHASHI, T., BECHTOLD, J. E., AND SCHILLINGER, D. Robust variational segmentation of 3D bone CT data with thin cartilage interfaces. *Medical Image Analysis* 47 (2018), 95–110.
- [44] GARNIER, C., KE, W., AND DILLENSEGER, J.-L. Bladder segmentation in MRI images using active region growing model. In *Engineering in Medicine and Biology Society, EMBC, 2011 Annual International Conference of the IEEE* (2011), IEEE, pp. 5702–5705.
- [45] GAURIAU, R. *Shape-based approaches for fast multi-organ localization and segmentation in 3D medical images*. Phd thesis, Telecom ParisTech, June 2015.
- [46] GEFFROY, D., RIVIÈRE, D., DENGHIEN, I., SOUÉDET, N., LAGUITTON, S., AND COINTEPAS, Y. Brainvisa: a complete software platform for neuroimaging. In *Python in Neuroscience Workshop* (2011), Euroscipy, Paris.
- [47] GERIG, G., KUBLER, O., KIKINIS, R., AND JOLESZ, F. A. Nonlinear anisotropic filtering of MRI data. *IEEE Transactions on Medical Imaging* 11, 2 (1992), 221–232.
- [48] GILLES, B., AND MAGNENAT-THALMANN, N. Musculoskeletal MRI segmentation using multi-resolution simplex meshes with medial representations. *Medical Image Analysis* 14, 3 (2010), 291–302.

- [49] HAACKE, E. M., BROWN, R. W., THOMPSON, M. R., VENKATESAN, R., ET AL. *Magnetic resonance imaging: physical principles and sequence design*, vol. 82. Wiley-Liss New York:, 1999.
- [50] HAAK, D., PAGE, C.-E., AND DESERNO, T. M. A survey of DICOM viewer software to integrate clinical research and medical imaging. *Journal of Digital Imaging* 29, 2 (2016), 206–215.
- [51] HEIMANN, T., AND MEINZER, H.-P. Statistical shape models for 3D medical image segmentation: A review. *Medical Image Analysis* 13, 4 (2009), 543 – 563.
- [52] HEIMANN, T., VAN GINNEKEN, B., STYNER, M. A., ARZHAeva, Y., AURICH, V., BAUER, C., BECK, A., BECKER, C., BEICHEL, R., BEKES, G., ET AL. Comparison and evaluation of methods for liver segmentation from CT datasets. *IEEE Transactions on Medical Imaging* 28, 8 (2009), 1251–1265.
- [53] HERNÁNDEZ-HOYOS, M. *Segmentation anisotrope 3D pour la quantification en imagerie vasculaire par résonance magnétique*. PhD thesis, Lyon, INSA, 2002.
- [54] HIDA, T. Brownian motion. In *Brownian Motion*. Springer, 1980, pp. 44–113.
- [55] HILTUNEN, J., SUORTTI, T., ARVELA, S., SEPPÄ, M., JOENSUU, R., AND HARI, R. Diffusion tensor imaging and tractography of distal peripheral nerves at 3T. *Clinical Neurophysiology* 116, 10 (2005), 2315 – 2323.
- [56] HOLDEN, M. A review of geometric transformations for nonrigid body registration. *IEEE Transactions on Medical Imaging* 27, 1 (2008), 111–128.
- [57] HUISMAN, T. Diffusion-weighted and diffusion tensor imaging of the brain, made easy. *Cancer Imaging* 10, 1A (2010), S163.
- [58] IŞGUM, I., BENDERS, M. J., AVANTS, B., CARDOSO, M. J., COUNSELL, S. J., GOMEZ, E. F., GUI, L., HÜPPI, P. S., KERSBERGEN, K. J., MAKROPOULOS, A., ET AL. Evaluation of automatic neonatal brain segmentation algorithms: the NeoBrainS12 challenge. *Medical Image Analysis* 20, 1 (2015), 135–151.
- [59] JENKINSON, M., BECKMANN, C. F., BEHRENS, T., WOOLRICH, M. W., AND SMITH, S. M. FSL. *NeuroImage* 62, 2 (2012), 782 – 790. 20 Years of fMRI.

- [60] KAMNITSAS, K., LEDIG, C., NEWCOMBE, V. F., SIMPSON, J. P., KANE, A. D., MENON, D. K., RUECKERT, D., AND GLOCKER, B. Efficient multi-scale 3D CNN with fully connected crf for accurate brain lesion segmentation. *Medical Image Analysis* 36 (2017), 61 – 78.
- [61] KIRBAS, C., AND QUEK, F. A review of vessel extraction techniques and algorithms. *ACM Computing Surveys (CSUR)* 36, 2 (2004), 81–121.
- [62] KNUTSSON, H., AND ANDERSSON, M. Morphons: Segmentation using elastic canvas and paint on priors. In *12th IEEE International Conference on Image Processing (ICIP 2005), Genova, Italy, 11 Sep-14 Sep 2005* (2005), pp. 1226–1229.
- [63] KRČAH, M., SZÉKELY, G., AND BLANC, R. Fully automatic and fast segmentation of the femur bone from 3D-CT images with no shape prior. In *Biomedical Imaging: From Nano to Macro, 2011 IEEE International Symposium on* (2011), IEEE, pp. 2087–2090.
- [64] KULLBERG, J., KARLSSON, A.-K., STOKLAND, E., SVENSSON, P.-A., AND DAHLGREN, J. Adipose tissue distribution in children: Automated quantification using water and fat MRI. *Journal of Magnetic Resonance Imaging* 32, 1 (2010), 204–210.
- [65] LAMECKER, H., SEEBASS, M., HEGE, H., AND DEUFLHARD, P. A 3D statistical shape model of the pelvic bone for segmentation. In *Medical Imaging* (2004), vol. SPIE 5370, pp. 1341–1351.
- [66] LAW, M. W., AND CHUNG, A. C. Efficient implementation for spherical flux computation and its application to vascular segmentation. *IEEE Transactions on Image Processing* 18, 3 (2009), 596–612.
- [67] LAY, N., BIRKBECK, N., ZHANG, J., AND ZHOU, S. K. Rapid multi-organ segmentation using context integration and discriminative models. In *Information Processing in Medical Imaging* (Berlin, Heidelberg, 2013), J. C. Gee, S. Joshi, K. M. Pohl, W. M. Wells, and L. Zöllei, Eds., Springer Berlin Heidelberg, pp. 450–462.
- [68] LE BIHAN, D., MANGIN, J.-F., POUPON, C., CLARK, C. A., PAPPATA, S., MOLKO, N., AND CHABRIAT, H. Diffusion tensor imaging: concepts and applications. *Journal of Magnetic Resonance Imaging: An Official Journal of the International Society for Magnetic Resonance in Medicine* 13, 4 (2001), 534–546.

- [69] LESAGE, D., ANGELINI, E. D., BLOCH, I., AND FUNKA-LEA, G. A review of 3D vessel lumen segmentation techniques: Models, features and extraction schemes. *Medical Image Analysis* 13, 6 (2009), 819–845.
- [70] LI, B., AND ACTON, S. T. Active contour external force using vector field convolution for image segmentation. *IEEE transactions on image processing* 16, 8 (2007), 2096–2106.
- [71] LIAO, W., DESERNO, T. M., AND SPITZER, K. Evaluation of free non-diagnostic DICOM software tools. In *Proceedings of SPIE* (2008), vol. 6919, pp. 691903–691903.
- [72] LIN, Q. *Enhancement, detection, and visualization of 3D volume data*. PhD thesis, Linköping University, Department of Electrical Engineering, 2001.
- [73] LITJENS, G., KOOI, T., BEJNORDI, B. E., SETIO, A. A. A., CIOMPI, F., GHAFORIAN, M., VAN DER LAAK, J. A., VAN GINNEKEN, B., AND SÁNCHEZ, C. I. A survey on deep learning in medical image analysis. *Medical Image Analysis* 42 (2017), 60–88.
- [74] LORIGO, L. M., FAUGERAS, O., GRIMSON, W. E. L., KERIVEN, R., AND KIKINIS, R. Segmentation of bone in clinical knee MRI using texture-based geodesic active contours. In *International Conference on Medical Image Computing and Computer-Assisted Intervention* (1998), Springer, pp. 1195–1204.
- [75] LORIGO, L. M., FAUGERAS, O. D., GRIMSON, W. E. L., KERIVEN, R., KIKINIS, R., NABAVI, A., AND WESTIN, C.-F. Curves: Curve evolution for vessel segmentation. *Medical Image Analysis* 5, 3 (2001), 195–206.
- [76] MA, Z., JORGE, R. N., MASCARENHAS, T., AND TAVARES, J. M. R. Novel approach to segment the inner and outer boundaries of the bladder wall in T2-weighted magnetic resonance images. *Annals of Biomedical Engineering* 39, 8 (2011), 2287–2297.
- [77] MANINIS, K.-K., PONT-TUSET, J., ARBELÁEZ, P., AND VAN GOOL, L. Deep retinal image understanding. In *International Conference on Medical Image Computing and Computer-Assisted Intervention* (2016), Springer, pp. 140–148.
- [78] MATSUMOTO, J. S., MORRIS, J. M., FOLEY, T. A., WILLIAMSON, E. E., LENG, S., MCGEE, K. P., KUHLMANN, J. L., NESBERG, L. E., AND VRTISKA, T. J. Three-dimensional physical modeling: applications and experience at Mayo Clinic. *Radiographics* 35, 7 (2015), 1989–2006.

- [79] MAZONAKIS, M., DAMILAKIS, J., VARVERIS, H., PRASSOPOULOS, P., AND GOURTISOYIANNIS, N. Image segmentation in treatment planning for prostate cancer using the region growing technique. *The British Journal of Radiology* 74, 879 (2001), 243–249.
- [80] MCAULIFFE, M. J., LALONDE, F. M., MCGARRY, D., GANDLER, W., CSAKY, K., AND TRUS, B. L. Medical image processing, analysis and visualization in clinical research. In *14th IEEE Symposium on Computer-Based Medical Systems (CBMS)* (2001), pp. 381–386.
- [81] MCINERNEY, T., AND TERZOPOULOS, D. T-snakes: Topology adaptive snakes. *Medical Image Analysis* 4, 2 (2000), 73–91.
- [82] MENDOZA, C. S., KANG, X., SAFDAR, N., MYERS, E., MARTIN, A. D., GRISAN, E., PETERS, C. A., AND LINGURARU, M. G. Automatic analysis of pediatric renal ultrasound using shape, anatomical and image acquisition priors. In *International Conference on Medical Image Computing and Computer-Assisted Intervention* (2013), Springer, pp. 259–266.
- [83] MILLETARI, F., NAVAB, N., AND AHMADI, S.-A. V-net: Fully convolutional neural networks for volumetric medical image segmentation. In *3D Vision (3DV), 2016 Fourth International Conference on* (2016), IEEE, pp. 565–571.
- [84] MONTAGNAT, J. *Deformable modelling for 3D and 4D medical image segmentation*. PhD thesis, PhD thesis, Nice–Sophia Antipolis University, Nice, France, 1999.
- [85] MORI, S., AND VAN ZIJL, P. C. Fiber tracking: principles and strategies—a technical review. *NMR in Biomedicine: An International Journal Devoted to the Development and Application of Magnetic Resonance In Vivo* 15, 7-8 (2002), 468–480.
- [86] NILLESEN, M. M., LOPATA, R. G., GERRITS, I. H., KAPUSTA, L., HUISMAN, H. J., THIJSSSEN, J. M., AND DE KORTE, C. L. Segmentation of the heart muscle in 3-D pediatric echocardiographic images. *Ultrasound in Medicine & Biology* 33, 9 (2007), 1453–1462.
- [87] NILLESEN, M. M., LOPATA, R. G., HUISMAN, H., THIJSSSEN, J. M., KAPUSTA, L., AND DE KORTE, C. L. Correlation based 3-D segmentation of the left ventricle in pediatric echocardiographic images using radio-frequency data. *Ultrasound in Medicine & Biology* 37, 9 (2011), 1409–1420.

- [88] O'DONNELL, L. J., AND WESTIN, C.-F. Automatic tractography segmentation using a high-dimensional white matter atlas. *IEEE Transactions on Medical Imaging* 26, 11 (2007), 1562–1575.
- [89] OLIVEIRA, F., AND TAVARES, J. M. R. Medical image registration: a review. *Computer Methods in Biomechanics and Biomedical Engineering* 17, 2 (2014), 73–93.
- [90] PAN, S. J., AND YANG, Q. A survey on transfer learning. *IEEE Transactions on Knowledge and Data Engineering* 22, 10 (2010), 1345–1359.
- [91] PARIS, S., KORNPORST, P., TUMBLIN, J., DURAND, F., ET AL. Bilateral filtering: Theory and applications. *Foundations and Trends in Computer Graphics and Vision* 4, 1 (2009), 1–73.
- [92] PASQUIER, D., LACORNERIE, T., VERMANDEL, M., ROUSSEAU, J., LARTIGAU, E., AND BETROUNI, N. Automatic segmentation of pelvic structures from magnetic resonance images for prostate cancer radiotherapy. *International Journal of Radiation Oncology* Biology* Physics* 68, 2 (2007), 592–600.
- [93] PERONA, P., AND MALIK, J. Scale-space and edge detection using anisotropic diffusion. *IEEE Transactions on Pattern Analysis and Machine Intelligence* 12, 7 (1990), 629–639.
- [94] PETTERSSON, J., KNUTSSON, H., AND BORGA, M. Automatic hip bone segmentation using non-rigid registration. In *IEEE 18th International Conference on Pattern Recognition (ICPR'06)* (2006), vol. 3, pp. 946–949.
- [95] PHELLAN, R., AND FORKERT, N. D. Comparison of vessel enhancement algorithms applied to time-of-flight MRA images for cerebrovascular segmentation. *Medical Physics* 44, 11 (2017), 5901–5915.
- [96] PRESTI, G. L., CARBONE, M., CIRIACI, D., ARAMINI, D., FERRARI, M., AND FERRARI, V. Assessment of DICOM viewers capable of loading patient-specific 3D models obtained by different segmentation platforms in the operating room. *Journal of Digital Imaging* 28, 5 (Oct 2015), 518–527.
- [97] RIVIÈRE, D., GEFFROY, D., DENGHIEN, I., SOUÉDET, N., AND COINTEPAS, Y. Anatomist: a python framework for interactive 3D visualization of neuroimaging data. In *Python in Neuroscience Workshop* (2011).
- [98] ROCHERY, M., JERMYN, I. H., AND ZERUBIA, J. New higher-order active contour energies for network extraction. In *Image Processing, 2005. ICIP 2005. IEEE International Conference on* (2005), vol. 2, IEEE, pp. II–822.

- [99] ROHR, K., STIEHL, H. S., SPRENGEL, R., BUZUG, T. M., WEESE, J., AND KUHN, M. Landmark-based elastic registration using approximating thin-plate splines. *IEEE Transactions on Medical Imaging* 20, 6 (2001), 526–534.
- [100] ROSSET, A., SPADOLA, L., AND RATIB, O. OsiriX: an open-source software for navigating in multidimensional DICOM images. *Journal of Digital Imaging* 17, 3 (2004), 205–216.
- [101] SATO, Y., NAKAJIMA, S., ATSUMI, H., KOLLER, T., GERIG, G., YOSHIDA, S., AND KIKINIS, R. 3d multi-scale line filter for segmentation and visualization of curvilinear structures in medical images. In *CVRMed-MRCAS’97* (1997), Springer, pp. 213–222.
- [102] SCHMID, J., AND MAGNENAT-THALMANN, N. MRI bone segmentation using deformable models and shape priors. In *International Conference on Medical Image Computing and Computer-Assisted Intervention (MICCAI)* (2008), vol. 5241, pp. 119–126.
- [103] SCHNEIDER, C. A., RASBAND, W. S., AND ELICEIRI, K. W. NIH image to ImageJ: 25 years of image analysis. *Nature Methods* 9, 7 (2012), 671–675.
- [104] SEIM, H., KAINMUELLER, D., HELLER, M., LAMECKER, H., ZACHOW, S., AND HEGE, H. Automatic segmentation of the pelvic bones from CT data based on a statistical shape model. *Eurographics Workshop on Visual Computing for Biomedicine* (2008), 93–100.
- [105] SEIM, H., KAINMUELLER, D., LAMECKER, H., BINDERNAGEL, M., MALINOWSKI, J., AND ZACHOW, S. Model-based auto-segmentation of knee bones and cartilage in MRI data. *Medical Image Analysis for the Clinic: A Grand Challenge, Beijing* (2010).
- [106] SHIN, H.-C., ROTH, H. R., GAO, M., LU, L., XU, Z., NOGUES, I., YAO, J., MOLLURA, D., AND SUMMERS, R. M. Deep convolutional neural networks for computer-aided detection: CNN architectures, dataset characteristics and transfer learning. *IEEE Transactions on Medical Imaging* 35, 5 (2016), 1285–1298.
- [107] SIMONYAN, K., AND ZISSERMAN, A. Very deep convolutional networks for large-scale image recognition. *CoRR abs/1409.1556* (2014).
- [108] SMITH, F. W. The value of NMR imaging in pediatric practice: A preliminary report. *Pediatric Radiology* 13, 3 (May 1983), 141–147.

- [109] SONG, Q., LIU, Y., LIU, Y., SAHA, P. K., SONKA, M., AND WU, X. Graph search with appearance and shape information for 3-D prostate and bladder segmentation. In *International Conference on Medical Image Computing and Computer-Assisted Intervention* (2010), Springer, pp. 172–180.
- [110] SPRENGEL, R., ROHR, K., AND STIEHL, H. S. Thin-plate spline approximation for image registration. In *Engineering in Medicine and Biology Society, 1996. Bridging Disciplines for Biomedicine. Proceedings of the 18th Annual International Conference of the IEEE* (1996), vol. 3, IEEE, pp. 1190–1191.
- [111] SUNDGREN, P. C., AND LEANDER, P. Is administration of gadolinium-based contrast media to pregnant women and small children justified? *Journal of Magnetic Resonance Imaging* 34, 4 (2011), 750–757.
- [112] SUNG, G. T., AND GILL, I. S. Robotic laparoscopic surgery: a comparison of the da Vinci and Zeus systems. *Urology* 58, 6 (2001), 893–898.
- [113] TOLEDO, R., ORRIOLS, X., BINEFA, X., RADEVA, P., VITRIA, J., AND VILLANUEVA, J. J. Tracking elongated structures using statistical snakes. In *Computer Vision and Pattern Recognition, 2000. Proceedings. IEEE Conference on* (2000), vol. 1, IEEE, pp. 157–162.
- [114] TOUSSAINT, N., SOUPLET, J.-C., FILLARD, P., ET AL. MedINRIA: Medical image navigation and research tool by INRIA. In *MICCAI* (2007), vol. 7, p. 280.
- [115] VALERI, G., MAZZA, F. A., MAGGI, S., ARAMINI, D., LA RICCIA, L., MAZZONI, G., AND GIOVAGNONI, A. Open source software in a practical approach for post processing of radiologic images. *La radiologia medica* 120, 3 (Mar 2015), 309–323.
- [116] VAN DER JAGT, P. K., DIK, P., FROELING, M., KWEE, T. C., NIEVELSTEIN, R. A., TEN HAKEN, B., AND LEEMANS, A. Architectural configuration and microstructural properties of the sacral plexus: a diffusion tensor mri and fiber tractography study. *Neuroimage* 62, 3 (2012), 1792–1799.
- [117] VAPNIK, V. *The nature of statistical learning theory*. Springer science & business media, 2013.
- [118] VASILACHE, S., AND NAJARIAN, K. Automated bone segmentation from pelvic CT images. *Proc. IEEE Wkshp. on Bioinformatics and Biomedicine (BIBMW)* (2008), 41–47.

- [119] VASILEVSKIY, A., AND SIDDIQI, K. Flux maximizing geometric flows. *IEEE Transactions on Pattern Analysis & Machine Intelligence*, 12 (2002), 1565–1578.
- [120] VIRZÌ, A., GORI, P., MULLER, C., MILLE, E., PEYROT, Q., BERTELOOT, L., BODDAERT, N., SARNACKI, S., AND BLOCH, I. Segmentation of pelvic vessels in pediatric MRI using a patch based learning approach. In *Journées Francophones de Radiologique Diagnostique et Interventionnelle (JFR)* (Paris, France, 2018).
- [121] VIRZÌ, A., GORI, P., MULLER, C. O., MILLE, E., PEYROT, Q., BERTELOOT, L., BODDAERT, N., SARNACKI, S., AND BLOCH, I. Segmentation of pelvic vessels in pediatric MRI using a patch-based deep learning approach. In *Data Driven Treatment Response Assessment and Preterm, Perinatal, and Paediatric Image Analysis* (2018), Springer International Publishing, pp. 97–106.
- [122] VIRZÌ, A., MARRET, J. B., MULLER, C. O., BERTELOOT, L., BODDAERT, N., SARNACKI, S., AND BLOCH, I. A new method based on template registration and deformable models for pelvic bones semi-automatic segmentation in pediatric MRI. In *IEEE 14th International Symposium on Biomedical Imaging (ISBI)* (2017), pp. 323–326.
- [123] WAKANA, S., CAPRIHAN, A., PANZENBOECK, M. M., FALLON, J. H., PERRY, M., GOLLUB, R. L., HUA, K., ZHANG, J., JIANG, H., DUBEY, P., ET AL. Reproducibility of quantitative tractography methods applied to cerebral white matter. *Neuroimage* 36, 3 (2007), 630–644.
- [124] WANG, X., GRIMSON, W. E. L., AND WESTIN, C.-F. Tractography segmentation using a hierarchical dirichlet processes mixture model. *NeuroImage* 54, 1 (2011), 290–302.
- [125] WASSERMANN, D., BLOY, L., KANTERAKIS, E., VERMA, R., AND DERICHE, R. Unsupervised white matter fiber clustering and tract probability map generation: Applications of a gaussian process framework for white matter fibers. *NeuroImage* 51, 1 (2010), 228–241.
- [126] WASSERMANN, D., MAKRIS, N., RATHI, Y., SHENTON, M., KIKINIS, R., KUBICKI, M., AND WESTIN, C.-F. The white matter query language: a novel approach for describing human white matter anatomy. *Brain Structure and Function* 221, 9 (2016), 4705–4721.
- [127] WESTIN, C.-F., WARFIELD, S., BHALERAO, A., MUI, L., RICHOLT, J., AND KIKINIS, R. Tensor controlled local structure enhancement of CT

- images for bone segmentation. In *International Conference on Medical Image Computing and Computer-Assisted Intervention (MICCAI)* (1998), Springer, pp. 1205–1212.
- [128] XIA, Y., FRIPP, J., CHANDRA, S. S., SCHWARZ, R., ENGSTROM, C., AND CROZIER, S. Automated bone segmentation from large field of view 3D MR images of the hip joint. *Physics in Medicine & Biology* 58, 20 (2013), 7375.
- [129] XU, C., AND PRINCE, J. L. Generalized gradient vector flow external forces for active contours. *Signal Processing* 71, 2 (1998), 131–139.
- [130] XU, C., YEZZI, A., AND PRINCE, J. L. A summary of geometric level-set analogues for a general class of parametric active contour and surface models. In *IEEE Workshop on Variational and Level Set Methods in Computer Vision* (2001), pp. 104–111.
- [131] XU, Y., GÉRAUD, T., AND BLOCH, I. From neonatal to adult brain MR image segmentation in a few seconds using 3D-like fully convolutional network and transfer learning. In *23rd IEEE International Conference on Image Processing (ICIP), Beijing, China* (2017), pp. 4417–4421.
- [132] XU, Y., MOREL, B., DAHDOUH, S., ÉLODIE PUYBAREAU, VIRZÌ, A., URIEN, H., GÉRAUD, T., ADAMSBAUM, C., AND BLOCH, I. The challenge of cerebral magnetic resonance imaging in neonates: A new method using mathematical morphology for the segmentation of structures including diffuse excessive high signal intensities. *Medical Image Analysis* 48 (2018), 75 – 94.
- [133] YAO, J., AND TAYLOR, R. Non-rigid registration and correspondence finding in medical image analysis using multiple-layer flexible mesh template matching. *International Journal of Pattern Recognition and Artificial Intelligence* 17, 07 (2003), 1145–1165.
- [134] YI, J., AND RA, J. B. A locally adaptive region growing algorithm for vascular segmentation. *International Journal of Imaging Systems and Technology* 13, 4 (2003), 208–214.
- [135] YIM, P. J., CEBRAL, J. J., MULLICK, R., MARCOS, H. B., AND CHOYKE, P. L. Vessel surface reconstruction with a tubular deformable model. *IEEE Transactions on Medical Imaging* 20, 12 (2001), 1411–1421.
- [136] YOKOTA, F., OKADA, T., TAKAO, M., SUGANO, N., TADA, Y., AND SATO, Y. Automated segmentation of the femur and pelvis from 3D CT data of diseased hip using hierarchical statistical shape model of joint structure.

In *International Conference on Medical Image Computing and Computer-Assisted Intervention (MICCAI)* (2009), vol. LNCS 5762, pp. 811–818.

- [137] YUSHKEVICH, P., PIVEN, J., CODY, H., HO, S., GEE, J. C., AND GERIG, G. User-guided level set segmentation of anatomical structures with ITK-snap. In *NA-MIC/MICCAI Workshop on Open-Source Software* (2005).
- [138] YUSHKEVICH, P. A., PIVEN, J., HAZLETT, H. C., SMITH, R. G., HO, S., GEE, J. C., AND GERIG, G. User-guided 3D active contour segmentation of anatomical structures: Significantly improved efficiency and reliability. *NeuroImage* 31, 3 (2006), 1116–1128.
- [139] ZENG, G., YANG, X., LI, J., YU, L., HENG, P.-A., AND ZHENG, G. 3D U-net with multi-level deep supervision: Fully automatic segmentation of proximal femur in 3D MR images. In *Machine Learning in Medical Imaging* (Cham, 2017), Q. Wang, Y. Shi, H.-I. Suk, and K. Suzuki, Eds., Springer International Publishing, pp. 274–282.
- [140] ZHANG, Y., ZHANG, J., OISHI, K., FARIA, A. V., JIANG, H., LI, X., AKHTER, K., ROSA-NETO, P., PIKE, G. B., EVANS, A., ET AL. Atlas-guided tract reconstruction for automated and comprehensive examination of the white matter anatomy. *Neuroimage* 52, 4 (2010), 1289–1301.
- [141] ZHU, S. C., AND YUILLE, A. Region competition: Unifying snakes, region growing, and Bayes/MDL for multiband image segmentation. *IEEE Transactions on Pattern Analysis and Machine Intelligence* 18, 9 (1996), 884–900.
- [142] ZOU, K. H., WARFIELD, S. K., BHARATHA, A., TEMPANY, C. M., KAUS, M. R., HAKER, S. J., WELLS III, W. M., JOLESZ, F. A., AND KIKINIS, R. Statistical validation of image segmentation quality based on a spatial overlap index1: scientific reports. *Academic Radiology* 11, 2 (2004), 178–189.

Titre : Segmentation 3D de structures pelviennes en IRM pédiatrique pour de applications de planification chirurgicale

Mots clés : IRM pédiatrique, chirurgie pelvienne, segmentation 3D, modélisation 3D

Résumé : La planification chirurgicale repose sur l'anatomie du patient, et repose souvent sur l'analyse d'images médicales acquises avant la chirurgie. En particulier, c'est le cas pour les interventions de chirurgie pelvienne en pédiatrie, pour de nombreuses pathologies telles que des tumeurs et des malformations. Dans cette zone anatomique, en raison de sa forte vascularisation et innervation, une bonne planification chirurgicale est extrêmement importante pour éviter des lésions fonctionnelles des organes du patient, qui pourraient nuire à sa qualité de vie. En pratique clinique, la procédure standard repose sur l'analyse visuelle, coupe par coupe, des images de la région pelvienne. Cette tâche, même si elle est facilement accomplie par des radiologues experts, est très complexe et fastidieuse pour les chirurgiens, en raison de la complexité et de la variabilité des structures anatomiques et, par conséquent, de leurs images. De plus, en raison des variations anatomiques selon l'âge du patient, toutes ces difficultés sont accentuées en pédiatrie et une compréhension anatomique claire est encore plus importante que pour les adultes. Pour ces raisons, il est important et utile d'être capable de fournir aux chirurgiens des modèles anatomiques 3D spécifiques aux patients, obtenus par traitement et analyse des images IRM.

Dans cette thèse, nous proposons un ensemble de méthodes de segmentation d'images IRM de patients pédiatriques. Nous nous concentrons sur trois structures pelviennes importantes : les os du bassin, les vaisseaux sanguins et la vessie. Pour les os, nous proposons une méthode semi-automatique comportant une première étape de recalage de modèles osseux puis une étape de segmen-

tation fine par modèles déformables. La principale contribution de la méthode proposée est l'introduction d'un ensemble de modèles osseux pour différentes tranches d'âge, ce qui permet de prendre en compte la variabilité des os pendant la croissance. Pour les vaisseaux, nous proposons une méthode par *patches*, apprentissage profond et transfert d'apprentissage, donc ne nécessitant que peu de données d'apprentissage. La principale contribution de ce travail est la conception d'une procédure semi-automatique pour l'extraction des *patches*, qui permet à l'utilisateur de se focaliser uniquement sur les vaisseaux d'intérêt pour la planification chirurgicale. Pour la segmentation de la vessie, nous proposons d'utiliser une approche par modèles déformables, particulièrement robuste aux hétérogénéités de l'image et aux effets de volume partiel, souvent présents dans les images IRM pédiatriques.

Toutes les méthodes proposées sont intégrées dans une plateforme logicielle libre pour le traitement d'images médicales, donnant aux chirurgiens des outils performants avec des interfaces utilisateur faciles à utiliser. De plus, nous mettons en place une stratégie de traitement et de portabilité pour la visualisation des modèles 3D du patient, permettant aux chirurgiens de générer, visualiser et partager ces modèles au sein de l'hôpital.

En conclusion, les résultats obtenus avec les méthodes proposées sont quantitativement et qualitativement évalués de manière très positive par des chirurgiens pédiatriques, démontrant leurs potentialités pour l'utilisation en pratique clinique dans des procédures de planification chirurgicale.

Title : 3D segmentation of pelvic structures in pediatric MRI for surgical planning applications

Keywords : pediatric MRI, pelvic surgery, segmentation 3D, 3D modeling

Abstract : Surgical planning relies on the patient's anatomy, and it is often based on medical images acquired before the surgery. This is in particular the case for pelvic surgery on children, for various indications such as malformations or tumors. In this particular anatomical region, due to its high vascularization and innervation, a good surgical planning is extremely important to avoid potential functional damages to the patient's organs that could strongly affect their quality of life. In clinical practice the standard procedure is still to visually analyze, slice by slice, the images of the pelvic region. This task, even if quite easily performed by the expert radiologists, is difficult and tedious for the surgeons due to the complexity and variability of the anatomical structures and hence their images. Moreover, due to specific anatomy depending on the age of the patient, all the difficulties of the surgical planning are emphasized in the case of children, and a clear anatomical understanding is even more important than for the adults. For these reasons, it is very important and challenging to provide the surgeons with patient-specific 3D reconstructions, obtained from the segmentation of MRI images.

In this work we propose a set of segmentation tools for pelvic MRI images of pediatric patients. In particular, we focus on three important pelvic structures: the pelvic bones, the pelvic vessels and the

urinary bladder. For pelvic bones, we propose a semi-automatic approach based on template registration and deformable models. The main contribution of the proposed method is the introduction of a set of bones templates for different age ranges, which allows us to take into account the bones variability during growth. For vessels segmentation, we propose a patch-based deep learning approach using transfer learning, thus requiring few training data. The main contribution of this work is the design of a semi-automatic strategy for patches extraction, which allows the user to focus only on the vessels of interest for surgical planning. For bladder segmentation, we propose to use a deformable model approach that is particularly robust to image inhomogeneities and partial volume effects, which are often present in pediatric MRI images.

All the developed segmentation methods are integrated in an open-source platform for medical imaging, delivering powerful tools and user-friendly GUIs to the surgeons. Furthermore, we set up a processing and portability workflow for visualization of the 3D patient specific models, allowing surgeons to generate, visualize and share within the hospital the patient specific 3D models. Finally, the results obtained with the proposed methods are quantitatively and qualitatively evaluated by pediatric surgeons, which demonstrates their potentials for clinical use in surgical planning procedures.

